Understanding and Predicting Photoemission Properties of Semiconducting Photocathodes from Many-Body *Ab Initio* Theory

Von der Fakultät für Mathematik und Naturwissenschaften der Carl von Ossietzky Universität Oldenburg zur Erlangung des Grades und Titels eines

Doktors der Naturwissenschaften (Dr. rer. nat.)

angenommene Dissertation

von Herrn Richard Schier

geboren am 28.09.1997 in Berlin

Erstgutachter: Prof. Dr. Christopher Gies
Zweitgutachterin & Betreuerin: Prof. Dr. Caterina Cocchi

Tag der Disputation: 13.08.2026

Eigenständigkeitserklärung

Hiermit versichere ich, dass ich die vorliegende Arbeit selbstständig verfasst habe und keine anderen als die angegebenen Quellen verwendet, sowie keine unzulässige fremde Hilfe in Anspruch genommen habe. Zudem wurde die Arbeit nicht unter unkenntlichem Einsatz generativer KI erbracht. Außerdem versichere ich, dass ich die allgemeinen Prinzipien wissenschaftlichen Arbeitens und Veröffentlichens, wie sie in den Leitlinien guter wissenschaftlicher Praxis der Carl von Ossietzky Universität Oldenburg festgelegt sind, befolgt habe. Weiterhin erkläre ich, dass die Arbeit in gleicher oder ähnlicher Form noch keiner Prüfungsbehörde vorgelegt wurde.

Abstract

In the field of particle accelerator physics, one of the main topics of research is the development of high-performance electron sources. A significant class of materials for this purpose are (multi-)alkali antimonides, which are very promising due to their beneficial electronic and optical properties, especially their low bandgap and electron negativity, which allow emission in the visible and near-infrared region.

While there have already been extensive experimental studies in this field, the development of the next generation of photocathode materials is hindered by the still limited understanding of their fundamental properties on a microscopic level. The aim of this work is to help fill this void with a series of studies based on first principle methods. Based on density functional theory, we use a high-throughput approach to calculate the enrgetic stability as well as the basic electronic properties of a multitude of alkali antimonide crystals. Employing the GW approximation and the Bethe-Salpeter equation, we then proceed to calculate the optical properties of experimentally relevant stable crystals.

One major challenge is to link the microscopic electronic properties calculated with theoretical methods to the macroscopic observables measured in the experiment. To this end, we present a theoretical framework to calculate the quantum efficiency of semiconducting photocathodes through an implementation of the three-step model of photoemission based on the results from many-body perturbation theory. Contrary to previous implementation of the three-step model, this approach allows us to overcome the limitations of density functional theory by directly including quasiparticle and excitonic effects that are intrinsic to the photoexcitation process. In our approach, the quantum efficiency is derived by combining the optical absorption from the Bethe-Salpeter equation with an emission probability defined through the properties of the contributing excitons.

To validate this model, we compare its results against experimental measurements for various representative alkali antimonides crystals and demonstrate a very good agreement between experiment and our theoretical representation. Minor disagreements are found close to the photoemission threshold and can be attributed to neglecting surface roughness and impurities in real samples. Post-processing these results in the framework of classical Fresnel optics allows us to simulate thin films of finite thickness. With this we can quantitatively predict the quantum efficiency of samples and find an impressive agreement to experimental values.

Overall, this work offers deep and novel insights into the fundamental properties of alkali

antimonides. Through the implementation of a parameter-free *ab initio* tool based on Spicer's three-step-model for photoemission, we can link the calculated microscopic properties to macroscopic observables. The results allow us to better understand the physics behind the measured spectral response for photocathode materials and provide a pathway for the rational design of the next-generation of electron sources.

Abstract Deutsch

Von zentraler Bedeutung im Gebiet der Beschleunigerphysik ist die Entwicklung von leistungsfähigen Elektronenquellen. Für diesen Zweck sind (Multi-)Alkali-Antimonide eine vielversprechende Gruppe von Materialien, da sie günstige elektronische und optische Eigenschaften aufweisen, insbesondere eine niedrige Bandlücke und Elektronegativität, welche Elektronenemission für Licht im sichtbaren und Nahinfrarot-Bereich ermöglichen.

Trotz des Vorhandenseins umfangreicher experimentieller Studien wird die weitere Entwicklung von Materialien für Photokathoden durch ein eingeschränktes Verständnis ihrer Eigenschaften auf dem mikroskopischen Level gehemmt. Ziel dieser Arbeit ist es, diese Lücke durch eine Reihe von Studien basierend auf *ab initio* Methoden zu füllen. Mit einem High-Throughput-Screening basierend auf der Dichtefunktionaltheorie berechnen wir die Stabilität sowie die grundlegenden elektronischen Eigenschaften einer Vielzahl von Alkali-Antimoniden. Danach nutzen wir die GW-Näherung sowie die Bethe-Salpeter-Gleichung, um die optischen Eigenschaften praktisch relevanter und energetisch stabiler Kristalle zu berechnen.

Eine wesentliche Herausforderung ist es, die mikroskopischen elektronischen Eigenschaften, welche wir mit unseren theoretischen Methoden berechnen, mit den makroskopischen Größen, die im Experiment gemessen werden, zu verknüpfen. Um dies zu erreichen, stellen wir ein theoretisches Modell vor, mit dem wir die Quanteneffizienz von halbleitenden Photokathoden bestimmen können. Es kombiniert Spicers Drei-Stufen-Modell der Photoemission mit Ergebnissen basierend auf der Vielteilchen-Störungstheorie (Many-Body Perturbation Theory). Damit geht es insbesondere über frühere Implementierungen, die auf die Dichtefunktionaltheorie beschränkt waren, hinaus und beschreibt auch Vielteilcheneffekte, die ein essenzieller Bestandteil der Photoemission sind. Unser Ansatz beruht darauf, die Quanteneffizienz als Kombination der durch die Bethe-Salpeter-Gleichung bestimmten optischen Absorption und einer mit den Eigenschaften der angeregten Elektronen berechneten Emissionswahrscheinlichkeit zu bestimmen.

Zur Validierung vergleichen wir die mit unserem Modell erzielten Ergebnisse mit experimentiellen Datensätzen und zeigen eine sehr gute Übereinstimmung zwischen Theorie und Experiment für mehrere repräsentative Alkali-Antimonide. Abweichungen existieren nahe der Photoemissionsschwelle und lassen sich auf Oberflächeneffekte und Verunreinigungen, die im Modell nicht berücksichtigt werden, zurückführen. Ein weiteres Post-Processing der Ergebnisse basierend auf klassischer Fresneloptik erlaubt es uns, Filme einer endlichen, dünnen Dicke zu simulieren. Damit ist es möglich, die Quanteneffizienz realer Photokath-

oden quantitativ vorherzusagen. Eine exzellente Übereinstimmung mit experimentiellen Werten wird festgestellt.

Insgesamt bietet diese Arbeit tiefgehende und neuartige Einblicke in die grundlegenden Eigenschaften von Alkali-Antimoniden. Mit der Formulierung und Umsetzung eines parameterfreien *ab initio* Modells basierend auf Spicers Drei-Stufen-Modell für Photoemission können wir mikroskopische Eigenschaften mit den makroskopischen experimentiellen Observablen verknüpfen. Unsere Ergebnisse bieten ein besseres Verständnis der physikalischen Gründe für die gemessene Quanteneffizienz von Photokathoden bei verschiedenen Wellenlängen und öffnen damit den Weg für eine sinnvoll gerichtete Weiterentwicklung von Photokathoden als Elektronenquellen.

Contents

Constants and Abbreviations

$\boldsymbol{e}$ elementary charge
$\boldsymbol{m_e}$ electron mass
$\boldsymbol{h}$ Planck constant
$\boldsymbol{\hbar}$ reduced Planck constant
$\boldsymbol{\epsilon_0}$ vacuum permittivity
$\boldsymbol{\mu_0}$ vacuum magnetic permeability
$\boldsymbol{c}$ speed of light

Equations in Chap. 2 (Theoretical Background) are formulated in atomic units with $\hbar$, e, m_e, $4\pi\epsilon_0$ set to one.

BSE Bethe-Salpeter equation
BZ Brillouin zone
CBm conduction band minimum
DFT density functional theory
GGA generalized gradient approximation
IQPA independent quasi-particle approximation
KS Kohn-Sham
LCAO linear combination of atomic orbitals
MBPT many-body perturbation theory
MTE mean transverse energy
PDOS projected density of states
SCF self-consistent field
VBM valence band maximum
QE quantum efficiency
QP quasi-particle

Publications

Large parts of this work, including the figures, have been published:

[1] **R. Schier**, C. Wang, J. Dube, J. Kühn, A. Galdi, T. Kamps, and C. Cocchi: Quantitative photoemission predictions of semiconducting photocathodes from many-body ab initio theory (submitted)

[2] **R. Schier** and C. Cocchi: Electronic and optical excitations of K-Sb and Na-Sb crystals, Phys. Rev. Mat. 9, 053804 (2025)

[3] **R. Schier**, D. Guo, H.-D. Saßnick, and C. Cocchi: Stability and electronic properties of K-Sb and Na-Sb binary crystals from high-throughput ab initio calculations, Adv. Theory Simul. 7, 2400680 (2024)

Additionally, the contents of my preceding master's thesis were expanded and summarized in a publication. This study on the properties of surface facets constitutes the foundation of the present work:

[4] **R. Schier**, H.-D. Saßnick, and C. Cocchi: Stability and electronic properties of CsK_2Sb surface facets, Phys. Rev. Materials 6, 125001 (2022)

Furthermore, during the course of this work I wrote a proposal for an internship via RISE Germany, a program by the DAAD, which was approved and conducted. During this internship, which I supervised, the properties of additional crystals related to the topic of this thesis were calculated, leading to two further publications:

[5] C. Xu, **R. Schier**, and C. Cocchi: Electronic and optical properties of computationally predicted Na–K–Sb crystals, Electron. Struct. 7, 015001 (2025)

[6] C. Xu, **R. Schier**, and C. Cocchi: Ab initio X-ray near-edge spectroscopy of sodium-based multi-alkali antimonides, Phys. Chem. Chem. Phys. 27, 19071 (2025)

Results from [5] were utilized as part of the dataset for the model in this work.

Presentations

The results presented in this theses were disseminated at the following international conferences and workshops:

Materials for Bright Beams Workshop 2025 (Cornell University)
Invited Talk: Modeling photoemission in alkali antimonides from ab initio many-body theory

DPG-Frühjahrstagung der Sektion Kondensierte Materie 2025 (Regensburg)
Talk: Electronic and optical properties of K-Sb and Na-Sb binary crystals from ab initio many-body theory

European Workshop on Photocathodes for Particle Accelerator Applications 2024 (Helmholtz-Zentrum Dresden-Rossendorf)
Poster: Energetic and electronic properties of K-Sb and Na-Sb binary crystals from high-throughput ab initio calculations

DPG-Frühjahrstagung der Sektion Kondensierte Materie 2024 (Berlin)
Talk: Energetic and electronic properties of K-Sb and Na-Sb binary crystals from high-throughput ab initio calculations

1 Introduction

One of the most powerful tools in the experimental research and characterization of materials in the modern ages is the use of controlled electron beams. From the very first scanning electron microscopes developed in the middle of the 20th century [7] to modern techniques and devices like x-ray free electron lasers [8] and ultrafast electron microscopes [9, 10] operating on the femtosecond scale, we have seen a massive leap in experimental capabilities [11]. Crucial to these state-of-the-art methods is the availability of high brightness electron beams from particle accelerators [12]. The design of particle accelerators is clearly a very complex topic and an ongoing field of research. In this work we focus on the arguably most important part of it, the initial electron source [13].

The initial electron beam is generated through a photocathode, a material that absorbs light and emits free electrons. The mechanism behind this is the photoelectric effect, which was already observed in the late 19th century [14]. When a material is irradiated, electrons are dislodged and emitted from it, provided they receive an energy sufficient to overcome their binding energy. Notably, the energy transferred to the electrons depends on the frequency of the incoming light, not its intensity. For light of low frequency, no emission will take place, no matter how high the intensity of the light source is. In particular, this experimentally shown fact goes against the classical picture of a electromagnetic wave that continuously transfers energy to electrons and shows the quantization of light, as suggested by A. Einstein [15].

In state-of-the-art particle accelerators, a photocathode will be placed in an electron 'gun', where it is irradiated through a laser with a certain wavelength and band width. This produces a stream of free electrons via photoemission, which are then accelerated and focused through an initial electric field in order to be released into the subsequent part of the accelerator. The resulting electron beam can be further accelerated and focused until it reaches the desired specifications. In general, the final beam should be focused in space with a low transverse momentum, show a low energy range, and have a high brightness. The way to accomplish this is part of the development of particle accelerators and highly related to the design of suitable superconducting radio frequency (SRF) cavities containing the electromagnetic fields in the accelerator. However, the possible enhancement of the initial beam in the accelerator is not easy and limited by practical constraints like the length of linear accelerators. Therefore, it is crucial that already the initial beam provided by the photcathode in the electron gun is of high quality. Driven by this need, the development of photocathodes that can provide such beams has been an ongoing topic of research for many decades. Besides the experimental growth of actual samples, there

is a general need for understanding of the exact physics of the photocathode materials.

There are multiple distinct qualities that are desirable for photocathodes, depending on the exact setup the cathode is to be employed in [13, 16]. One main quantity is the quantum efficiency (QE). It is defined as the ratio of outgoing electrons to incoming photons [17]. A high quantum efficiency is very positive, as it means that a lower laser intensity is required to produce the desired amount of electrons. In addition to saving power, this makes it easier to control the experimental setup as possible heating or material degradation due to the laser is reduced. The quantum efficiency depends on the wavelength of the used laser. A material's quantum efficiency as function of the photon wavelength is called its spectral response and the focus of this work.

To illustrate this concept, the measured spectral response of four photocathode materials from the literature is shown in Fig. 1.

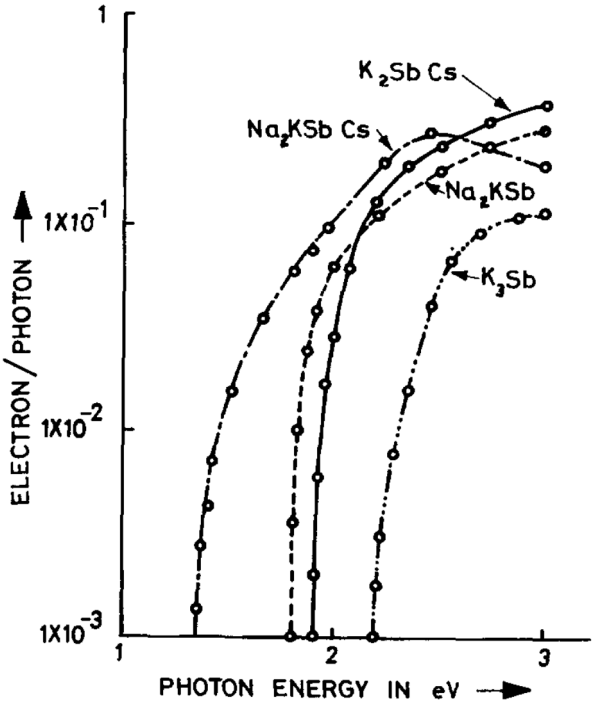

Figure 1: Measured spectral response of four alkali antimonides. Figure taken from [18].

Relevant quantities related to the spectral response are the energy of the photoemission onset as well as the maximum yield that is reached. As seen in Fig. 1, they can vary greatly depending on the photocathode material. Furthermore, the slope of the spectral response is not necessarily monotonic and local maxima can appear, as visible in Fig. 1 for Na_2KSbCs.

Another key parameter is the mean transverse energy (MTE), which, as the name suggests, describes how far the electron beam is spread out transverse to its direction in terms of momentum. It is directly related to the emittance ϵ:

$$\epsilon = \sigma_{x,y}\sqrt{\frac{\mathrm{MTE}}{m_e c^2}}. \tag{1}$$

In Eq. 1, $\sigma_{x,y}$ describes the spot size of the laser on the photocathode surface, while m_e and c are natural constants. A lower MTE is preferable in order to have a focused beam. It is also possible to reduce the spread of the beam later in the accelerator, but this is not trivial to implement. In this work, we are going to assume that the initial beam is sufficiently focused to neglect its transverse spread when calculating the photoemissive yield, and not cover the MTE explicitly.

Considering now the possible materials for photocathodes, we can distinguish between two classes, semiconductors and metals. For a long time, research has focused on metals, which are generally quite robust and offer long operational lifetimes [19] even without an ultra-high vacuum. However, metallic photocathodes have some serious downsides. They significantly heat up during absorption, which is generally not desirable, absorb in the ultraviolet region, which often needs a power conversion, and tend to have a rather high transverse emittance [13]. Furthermore, the quantum efficiency of metallic photocathodes tends to be rather low [20, 21] due to their high reflectivity and a low escape depth of the excited electrons [22].

Semiconducting photocathodes have, in a way, the opposite properties. They are much more fragile than metals and tend to degrade quickly. In addition to a limited operational lifetime [23], the photocathodes need to be kept in a vacuum to avoid contamination [13]. Furthermore, they usually need to be grown on a substrate. On the other hand, they heat up much less than metals due to their semiconducting character [24, 25] and usually have higher quantum efficiencies, reaching 5 - 10 % and beyond [23, 26, 27]. In particular, semiconductors tend to show a high quantum efficiency for light in the visible region, close to the wavelength of typical lasers [23]. With the advance of experimental techniques, semiconducting photocathodes have grown more popular, as the lack of robustness can be remediated by carefully controlling their working conditions.

Among the semiconducting materials, (multi-)alkali antimonides have come into the limelight [28, 29, 30]. They tend to have small band gaps and low electron affinities, allowing for photoemission in the visible and close to infrared region. While alkali antimonides

have been studied experimentally since the middle of the 20th century [18, 31], their development has seen a significant boost recently with the increased usage of semiconductors instead of metals as photocathodes, as mentioned above.

When considering the experimental side of photocathode research, one key field is the experimental procedure to grow samples. Photocathodes are grown on a substrate, which provides the structural base for the cathode itself. Common materials for this are molybdenum (Mo), used for example at Helmholtz-Zentrum Berlin (HZB) [32], and niobium (Nb) [33, 34]. Also more complex compounds containing more than one atomic species can be employed, for example $SrTiO_3$ [35]. Important is mainly that the substrate can withstand the required experimental conditions during operation, in particular the heat and flow of electrons. A substrate with a lattice that matches that of the planned photocathode can be beneficial for growing a clean crystal. On the substrate, the photocathode is then grown by depositing its planned constituents, usually by evaporating the atomic materials and then depositing them via dispensers. The constituents can be deposited all at the same time (co-deposition) [36, 37] or sequentially [23, 38]. This process tends to create polycrystalline phases. Through heating, a recrystallization can be induced in order to generate more pure crystals and reduce defects. Finding a good recipe for the combination of flux from the dispenser and heating is an ongoing area of research. In order to understand what is taking place during the growth process, it makes sense to continuously measure the quantum efficiency, which will reveal changes in the composition of the sample. As mentioned above, an ultra-high vacuum has to be maintained constantly in order to avoid the immediate degradation of the photocathode. Another state-of-the art method is epitaxial growth, which is challenging but can generate ultrathin (quasi-)epitaxial films that are close to ideal crystals [35].

After the growth of the sample, the spectral response can be measured. For this, a light source that can switch through different wavelengths is required. The photocurrent produced by the cathode is measured with a picoammeter, which can (for example) be connected to a positively biased copper wire in order to collect all electrons [39]. Knowing the photocurrent I_e as well as the optical power P_γ and wavelength λ of the light source, the QE at this wavelength can then be calculated with Eq. 2 [17].

$$\mathrm{QE} = \frac{I_e hc}{P_\gamma \lambda e}. \tag{2}$$

With the advancement of experimental materials research, increasingly in-depth studies of samples are possible, investigating complex topics like the effects of different growth proce-

dures or the interaction between photocathode material and substrate in heterostructures. In recent years, a vast amount of experimental data has been collected by many groups around the world by growing photocathode samples and measuring their properties, in particular the quantum efficiency. In order to systematically improve the growth recipes, a good understanding of the fundamental physics taking place in even the most complex compounds is necessary. On the one hand, experimental measurements need to be understood by connecting features in the spectral response to the fundamental electronic properties of the photoacthode materials. On the other hand, a general understanding of beneficial features in photocathode compounds is needed in order to systematically target structures that are expected to show a high quantum efficiency.

However, there are practical issues when collecting data from real-life samples. First of all, reproducibility is often an issue [23], as the exact control over growth parameters like the flux of the dispensers, the temperature, and the vacuum level can be limited. Furthermore, samples are often polycrystalline [29] and show surface roughness and impurities [40]. These effects make it difficult to fully understand which physical effects lead to the final measured spectral response.

In order to untangle the role of the different fundamental properties of photocathode materials, first principles methods have grown increasingly important [41, 42]. They offer direct insight into the electronic and optical properties of single crystals on a microscopic level, circumventing the limitations of polycrystalline experimental samples. Additionally, the increase of computational power allows us to run theoretical calculations on a level that was not yet available in the previous century. On the one hand, basic methods such as density functional theory are now very inexpensive compared to the available resources, allowing us to run a large number of calculations for different materials. On the other hand, more advanced and expensive methods such as the G_0W_0 approach and the Bethe Salpeter equation become more accessible and can be used to go beyond the properties provided by density functional theory. This advance offers us unprecedented possibilities to calculate and predict the properties of materials with *ab initio* methods.

In general, *ab initio* calculations for crystals yield results on the level of the unit cell that is being simulated. When calculating, for instance, the electronic and optical properties of a photocathode material, these would usually be calculated for a single unit cell in the bulk of the material. However, for the photoemission process the bulk properties are not the only part that is significant. Another crucial part is the final emission through the surface, for which the surface properties of the crystal become relevant. They can be accessed by simulating larger cells that contain entire surface facets [4]. Ultimately, we

wish to make a direct comparison between theoretical predictions and the macroscopic quantities measured in the experiment, namely the spectral response. For this, we need a complete model of the photoemission process, which connects the microscopic properties calculated for the bulk as well as the surface properties and allows us to predict the final photoemissive yield.

Our general understanding of the photoemission process is based on the three-step-model originally developed by Berglund and Spicer [43]. It divides the photoemission process into three main subsequent steps, which are visualized in Fig. 2.

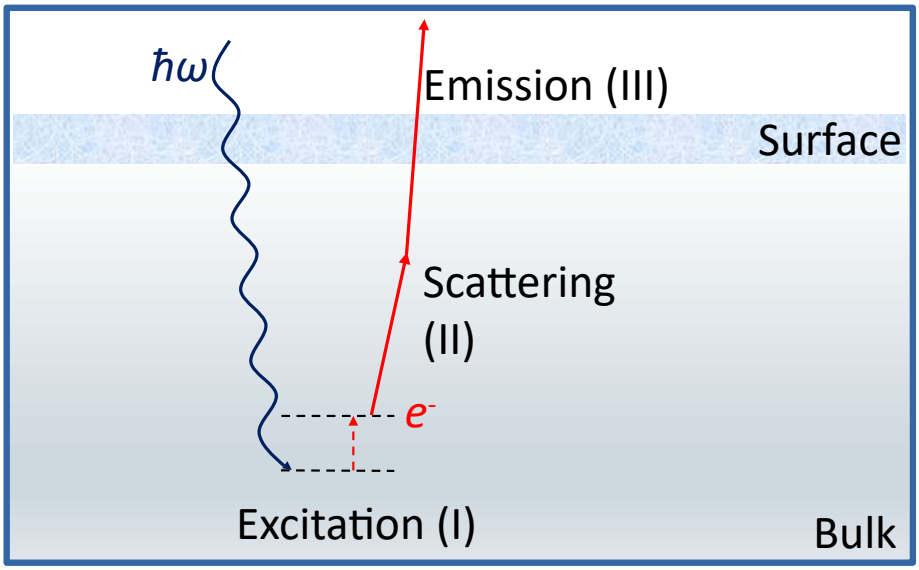

Figure 2: Sketch of the three sequential processes in the three-step model.

First, a photon enters the material and excites an electron in the bulk from a valence band (VB) to a conduction band (CB) (I). The excited electron is then transported to the surface, possibly undergoing scattering events (II). Finally, it has to overcome the surface in order to be emitted into the vacuum (III). While these three steps are straightforward, the detailed description of the physics on each level is unsurprisingly quite complex. Various implementations of the three-step-model are already available in the literature, mostly on a semi-empirical level. However, previous works [44, 45, 46] have been based only on density functional theory, treating electrons as single particles and their interactions through a mean-field approach.

In this work, we are going to present an implementation of the three-step-model based on many-body perturbation theory as well as the work that led up to it. With this we go beyond previous schemes as we directly include electron-electron and electron-hole

correlations in a many-body picture. We start by giving a overview over the theoretical background of the computational methods we employ, covering density functional theory as well as many-body perturbation theory (Chap. 2). In this chapter we also cover a brief overview of other photoemission models and implementations. Afterwards, we present in two chapters the computational data that has been collected in preparation for the creation of our model. In Chap. 3 we present data calculated through a high-throughput workflow based on density functional theory. Chapter 4 covers the calculation of electronic and optical properties from many-body perturbation theory for selected important crystals. In both parts we focus on alkali antimonides, as this is the class of materials that is most relevant in current research. Finally, in Chap. 5 we present our full scheme for the implementation of the three-step-model and use it to calculate the quantum efficiency / spectral response for various crystals based on the results previously collected from many-body perturbation theory.

2 Theoretical Background

This section aims to give an overview over our toolset based on density functional theory and many-body perturbation-theory, which we can use to calculate the electronic and optical properties of molecules and crystals. In this section, all equations are going to be formulated in atomic units with $\hbar$, e, m_e, $4\pi\epsilon_0$ set to one for improved readability.

2.1 The Many-body Problem

In the framework of quantum mechanics, the quantum state of a system is described by its wavefunction. All properties of the system are determined from the wavefunction, which can include any number n of particles. The wavefunction follows the time-dependent Schrödinger equation [47, 48]:

$$i\hbar\frac{d}{dt}\left|\mathbf{\Psi}(\vec{r_1},..,\vec{r_n},t)\right\rangle = \hat{H}\left|\mathbf{\Psi}(\vec{r_1},..,\vec{r_n},t)\right\rangle, \tag{3}$$

with the Hamiltonian $\hat{H}$ of the (non-relativistic) many-body system and the wavefunction $|\mathbf{\Psi}(\vec{r_1},..,\vec{r_n},t)\rangle$. The Hamiltonian consists of the kinetic energy operator $\hat{T}$ and the potential $\hat{V}$:

$$\hat{H} = \sum_i^n \hat{T}_i + \hat{V}(\vec{r_1},..,\vec{r_n},t) = \sum_i^n(-\frac{1}{2m_i})\nabla_i^2 + \hat{V}(\vec{r_1},..,\vec{r_n},t). \tag{4}$$

The Laplace operator ∇_i^2 is applied to the spatial coordinates $\vec{r_i}$ of the particle with index i and mass m_i, with $m_i = 1$ for electrons in atomic units. If the potential and therefore also the Hamiltonian is time-independent, Eq. 3 can be separated into a time-dependent and a time-independent part with the ansatz $|\mathbf{\Psi}(\vec{r_1},..,\vec{r_n},t)\rangle = |\Psi(\vec{r_1},..,\vec{r_n})\rangle\, T(t)$, leading to the solution $T(t) = a \cdot e^{-iEt}$ with a constant a and the time-independent Schrödinger equation

$$\hat{H}\left|\Psi(\vec{r_1},..,\vec{r_n})\right\rangle = E\left|\Psi(\vec{r_1},..,\vec{r_n})\right\rangle. \tag{5}$$

Relevant for real physical quantities is the probability density $|\mathbf{\Psi}(\vec{r_1},..,\vec{r_n},t)|^2$. It depends only on $|\Psi(\vec{r_1},..,\vec{r_n})\rangle$, while $T(t)$ is a phase factor without further relevance for stationary states. Therefore, it is sufficient to solve the time-independent version of the Schrödinger equation in Eq. 5 by determining the eigenvalues and eigenvectors of $\hat{H}$. This holds for any amount n of particles.

An exact analytical solution of the Schrödinger equation is possible for a single particle ($n = 1$) in simple potentials such as a potential well or a harmonic potential, and for more than one particle in special cases [49]. In particular, an analytical solution is available for

the hydrogen atom and was already discussed in the original work by Schrödinger [47]. This is possible by reducing the two-body problem of electron and proton to a one-body problem for an electron with a reduced mass moving around a fixed proton. However, analytical solutions are no longer possible for more complicated systems consisting of multiple interacting particle. This is made evident by the fact that already for the Helium atom no exact solution is available anymore.

For systems consisting of multiple atoms, we can use the Born-Oppenheimer approximation [50]. In this approximation, we assume the nuclei to have fixed position, because their mass is much larger than that of the electrons. We then seek a solution of Eq. 5 for a system of n electrons. As an exact analytical solution is not possible, other methods are needed in order to access $|\Psi(\vec{r_1}, .., \vec{r_n})\rangle$ and the properties of the many-body system. The goal is to do this *ab initio*, fully from fundamental principles and without the need for empirical parameters.

At the heart of *ab initio* methods is the variational principle. It is known that the energy of a physical system is always minimized for the real wavefunction $|\Psi\rangle$. If we create a trial wavefunction $|\Psi'\rangle$, then its energy can never be lower than that of the real wavefunction, $\langle\Psi|\,\hat{H}\,|\Psi\rangle = E \leq E' = \langle\Psi'|\,\hat{H}\,|\Psi'\rangle$. While we do not know the real energy E, we know that E' is an upper limit for it. We can now make numerous small variations to $|\Psi'\rangle$ in order to minimize its energy and to find the best possible approximation to $|\Psi\rangle$.

Multiple approaches that use the variational method to determine a good approximation for the wavefunction and its energy are available in the literature. An early *ab initio* method was presented by D. R. Hartree already in 1928 [51] and was later developed into the Hartree-Fock method [52, 53]. In this work, we use a different approach, namely density functional theory (DFT).

2.2 Density Functional Theory

Density functional theory offers a theoretical framework to transform the problem of solving the Schrödinger equation for a system of n interacting electrons to solving n Schrödinger-like equations for non-interacting particles. It is based on the two Hohenberg-Kohn Theorems [54], which show that (i) the potential $V(\vec{r})$ is a unique (except for a constant) functional of the electron probability density $\rho(\vec{r}) = |\Psi(\vec{r})|^2$ in the ground-state. Since the potential determines the Hamiltonian, the full many-particle ground-state is a unique functional of the density. Second, (ii) the variational principle applies also to the density and the ground-state energy is minimized for the exact density, just as it is

minimized for the exact wavefunction. In particular, it follows from the first Hohenberg-Kohn Theorem that it is not necessary to determine the exact wavefunction $|\Psi(\vec{r})\rangle$, the ground-state density $\rho(\vec{r})$ is sufficient.

The fact that only the density $\rho(\vec{r})$ is required motivates the Kohn-Sham (KS) approach [55], where we consider a fictitious system of n non-interacting single-electron wavefunctions $\phi_j(\vec{r})$ (Kohn-Sham wavefunctions) with the same total density as the real wavefunction $\Psi(\vec{r})$ containing n electrons:

$$|\Psi(\vec{r})|^2 = \rho(\vec{r}) = \sum_{j=1}^{n} |\phi_j(\vec{r})|^2. \tag{6}$$

The Kohn-Sham wavefunctions follow the Schrödinger-like Kohn-Sham equations

$$\hat{h}\,|\phi_j\rangle = \epsilon_j\,|\phi_j\rangle\,. \tag{7}$$

The single electrons described by the Kohn-Sham wavefunctions do not explicitly interact with each other. Instead, the interaction is included in an effective potential in the Kohn-Sham Hamiltonian $\hat{h} = \hat{t} + \hat{v}_{\text{eff}}$. From Eq. 6 and the first Hohenberg-Kohn Theorem, it follows that all physical properties of the many-electron system can be determined by solving the Kohn-Sham equations and finding the eigenvectors ϕ_j. Up to this point, DFT is an exact theory. However, an exact expression for the effective potential in the KS-Hamiltonian is not known and approximations need to be made.

We can split the KS-Hamiltonian as following:

$$\hat{h} = \hat{t} + \hat{v}_{\text{eff}} = \hat{t} + \hat{v}_{\text{ext}} + \hat{v}_{\text{H}} + \hat{v}_{\text{xc}}. \tag{8}$$

This includes the kinetic energy operator $\hat{t} = -\frac{1}{2}\vec{\nabla}^2$, the effects of an external potential $\hat{v}_{\text{ext}}$, the classical interaction between electrons via the Hartree potential $\hat{v}_{\text{H}}$ as well as all interactions between the electrons that go beyond the classical picture with the exchange-correlation potential $\hat{v}_{\text{xc}}$. The first two terms of the potential are known: In the absence of an additional external electric field, $\hat{v}_{\text{ext}}$ can be described by only the Coulomb potential of the nuclei, $\hat{v}_{\text{ext}}(\vec{r}) = \sum_i \frac{Q_i}{|\vec{r}-\vec{x_i}|}$, with the electric charges Q_i and the nuclear positions $\vec{x}_i$. This assumes that we are using the Born-Oppenheimer approximation with completely localized nuclei. Similarly, the Hartree potential $\hat{v}_{\text{H}}$ corresponds to the Coulomb interaction between the electrons distributed according to the density $\rho(\vec{r})$: $\hat{v}_{\text{H}}(\vec{r}) = \int_V \frac{\rho(\vec{r}')}{|\vec{r}-\vec{r}'|} d\vec{r}'$.

Finally, $\hat{v}_{\text{xc}}$ includes the exchange and correlation interactions between electrons, go-

ing beyond the classical picture. The exchange interaction follows from the required symmetry of the many-electron wavefunction. The electrons are identical particles with half-integer spin (fermions) and must have a fully antisymmetric wavefunction. As stated by the Pauli-principle, two identical fermions in the same position can never be in the same quantum state in order to maintain the required antisymmetry of the wavefunction. This implies that additional energy is required if two particles show a significant spatial overlap, as one of the particles is pushed into a higher energetic state (Pauli repulsion). This repulsive character is to be described through the exchange interaction in $\hat{v}_{\mathrm{xc}}$. The second part, the electronic correlation, is a correction to the Hartree potential describing the Coulomb interaction between the electrons. As the Hartree potential is calculated through a mean-field approach with the charge density and not the actual position of the electron, it overestimates the electronic repulsion. If the position of one electron was to be determined through a measurement, this would lead to an instantaneous deformation of the wavefunction of all other electrons to a new, energetically more beneficial state. This correlation leads to a lower overall energy of the system and also needs to be covered through $\hat{v}_{xc}$.

As stated before there, is no exact mathematical expression for the exchange-correlation potential $\hat{v}_{xc}$. In particular, the exchange and correlation effects on one electron depend on the electronic densities in the entire rest of the system system and are therefore intrinsically non-local. Thus, it is necessary to find a useful and physically justified approximation for $\hat{v}_{xc}$ that can be used in practical calculations.

Different approaches are available in the literature, with their performance depending on the system they are applied to. In general, we can rank the available approximations based on their increasing computational cost, commonly referred to as Jacob's Ladder [56] after the staircase to heaven from the bible. The most basic level is a functional based only on the local density in the local density approximation (LDA). In this case, the exchange-correlation energy associated with the Kohn-Sham wavefunction with index j can be calculated as

$$\epsilon_{\mathrm{xc},\,j}^{\mathrm{LDA}} = \langle \phi_j |\, v_{\mathrm{xc}}^{\mathrm{LDA}} \,| \phi_j \rangle = \int |\phi_j(\vec{r})|^2 E_{\mathrm{xc}}(\rho(\vec{r}))d\vec{r}. \tag{9}$$

The concrete dependence $E_{\mathrm{xc}}(\rho(\vec{r}))$ can be approximated by treating the elctron density pointwise as a homogeneous electron gas. Under this assumption, the exchange energy density can be determined analytically [57], it is proportional to $\rho(\vec{r})^{1/3}$. For the correlation energy, exact expressions can be found in the low and high density limit [58, 59]. Beyond these limits, a parametrized expression can be formulated [58], fitting the param-

eters to numerical stochastic data [60].

The approximation as a homogenous electron gas is reasonable for slowly varying densities, but ignores effects from the non-uniformity of the density. The next step is therefore to include further terms that account for the possible inhomogeneity of the system [61, 62]. This leads to the generalized gradient approximation (GGA), where the functional depends on the local electron density as well as its derivative as a measure of the density's non-uniformity [63, 64]. Analogous to above, the exchange-correlation energy can then be formulated as

$$\epsilon_{\mathrm{xc},\,j}^{\mathrm{GGA}} = \int |\phi_j(\vec{r})|^2 E_{\mathrm{xc}}(\rho(\vec{r}), \nabla\rho(\vec{r}))d\vec{r}. \tag{10}$$

One of the most popular GGA functionals is the Perdew-Burke-Ernzerhof (PBE) functional [65], which yields good results for a wide range of systems without using empirical parameters. Another possible approach is the creation of a semi-empirical functional with parameters that are fitted to known energies. Further derivatives can be included, leading to the class of Meta-GGA functionals. While the inclusion of more terms leads to an increase in computational cost going from LDA to Meta-GGA, it also increases the computational accuracy.

In order to obtain a more complete picture, also non-local effects can be covered through an exchange energy calculated with the Hartree-Fock method [66]. The Hartree-Fock exact exchange can then be combined with the exchange and correlation energies calculated with lower level approximations to formulate so called hybrid functionals:

$$\epsilon_{xc}^{\mathrm{hybrid}} = a\epsilon_x^{\mathrm{HF}} + (1-a)\epsilon_x + \epsilon_c, \tag{11}$$

with the Hartree-Fock exchange ϵ_x^{HF} as well as the exchange ϵ_x and correlation ϵ_c from an existing functional and a constant a. Examples of hybrid functionals are PBE0 [67] based on PBE with $a = \frac{1}{4}$, B3LYP [68, 69], and its further development CAM-B3LYP [70]. PBE0 is non-empirical, while B3LYP uses an empirical parametrization. A major downside of all hybrid functionals is a large jump in computational cost due to the non-locality of the calculation of the exact exchange.

With one of the available approximations for the exchange-correlation potential, it is then possible to solve the KS-equations numerically. For this purpose, we employ an iterative self-consistent-field (SCF) method, as the Hamiltonian $\hat{h}$ depends on the density, which itself is to be calculated through the KS-equations. This approach is illustrated in Fig. 3.

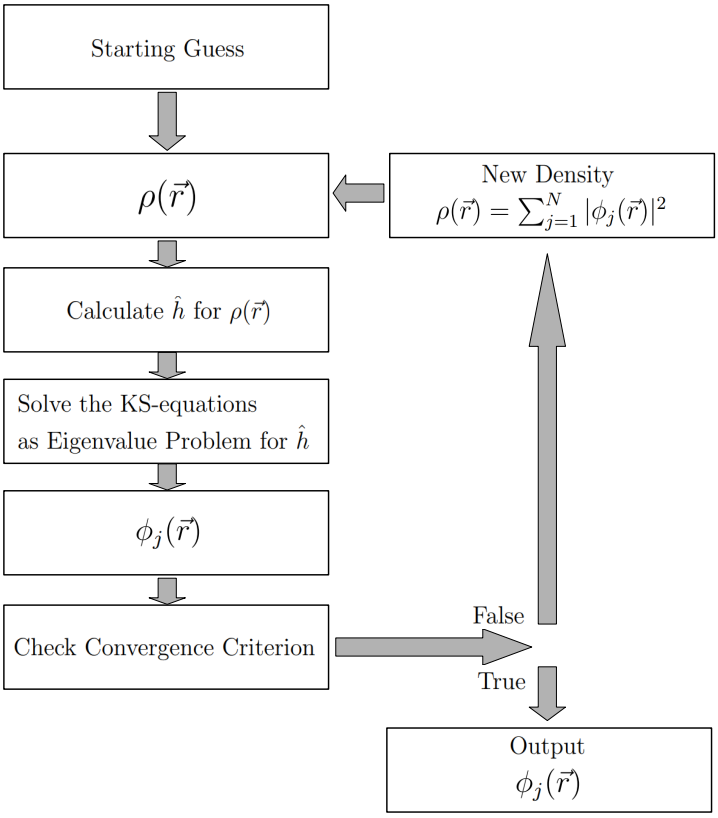

Figure 3: SCF-loop to calculate the Kohn-Sham wavefunctions $\phi_j(\vec{r})$ through an iterative approach.

For the numerical calculation of the wavefunctions $\phi_j(\vec{r})$, they are devolved into a set of M basis functions $\chi_\alpha(\vec{r})$:

$$\phi_j(\vec{r}) = \sum_{\alpha=1}^{M} c_{j\alpha}\chi_\alpha(\vec{r}). \tag{12}$$

Computationally, $\phi_j(\vec{r})$ can then be determined by calculating the coefficients $c_{j\alpha}$ for the basis functions. The mapping between ϕ_j and the linear combination of basis functions is exact for a complete basis set, which requires an infinite set of basis functions. If the basis set is finite, Eq. 12 is to be understood as an approximation.

The creation of suitable basis sets has been an ongoing area of computational research since the emergence of the first DFT codes. On the one hand, a basis set needs to allow an accurate description of the wavefunction $\phi_j(\vec{r})$. On the other hand, computational calculations need to remain cost effective, therefore a small amount of basis functions and a quick convergence of calculations are beneficial.

One common approach to the creation of basis sets is the use of atomic orbitals centered at the nuclei. The wavefunction is then described as a linear combination of atomic

orbitals (LCAO). Nowadays, the functions that are usually employed for this purpose are Gaussian type orbitals (GTOs) [71]. They have the form

$$\chi^{l_x,l_y,l_z,\zeta}(x,y,z) = N x^{l_x} y^{l_y} z^{l_z} e^{-\zeta(x^2+y^2+z^2)}, \tag{13}$$

with integers l_x, l_y, l_z, a positive width ζ, and a normalization factor N. Another possible type of functions are Slater type orbitals (STOs) [72]. For computational purposes, the basis functions can be build by contracting multiple 'primitive' Gaussian type orbitals into one function. This improves computational efficiency and allows the construction of functions that are particularly suited for a certain class of system by choosing appropriate coefficients for the combination.

By design, the LCAO approach works best for systems where the electron density is localized around the nuclei and indeed resembles atomic orbitals. This is not always the case. For larger systems and especially solids an accurate description is required also in regions further away from the atomic cores. For this, we can use basis functions based on plane waves, $\chi(\vec{r}) \propto e^{i\vec{k}\vec{r}}$. The plane waves are used up to a certain wavevector or energy cutoff that is to be converged.

It is also possible to mix atomic orbitals and plane waves by discriminating between spheres close to atoms, where orbital-based basis sets are used, and the room in-between, where plane-waves are sufficient. This leads to the class of linearized augmented-plane-wave (LAPW) basis sets.

Finally, it is not always necessary to explicitly treat all electrons in the system through the Kohn-Sham equations. For larger systems, we observe that there is usually a set of core electrons around atoms, which show no significant changes compared to the orbitals of the single atoms. We can therefore decide to not explicitly include these core electrons in our calculations. Instead, they are treated through a pseudopotential approximation, which mimics their effect on the rest of the system. In order to do this, a parametrization of the short-range and long-range effects of the core electrons is created in the form of a potential. The most popular and successful formulation that is available today is the one by Goedecker, Teter, and Hutter (GTH) [73, 74]. The parameters, which are individual to the used exchange-correlation functional, are then fitted to the results from an all-electron calculation [75].

2.3 Calculating Properties of Crystals

In this work, we are interested in the properties of larger crystals. While it is not possible to simulate an entire macroscopic crystal with DFT due to the large number of atoms, this is not necessary either. A defining feature of crystals is their periodicity. There is a crystal lattice defined by its lattice vectors as well as the atoms located on it, which in turn create a periodic potential. As finite crystals are much larger than the atomic scale on which we are operating, we can assume an infinite periodicity in all directions.

The physics behind electrons in such a crystal lattice have been analyzed by F. Bloch already in 1929 [76]. In particular, Bloch's theorem states that if there is a periodic potential $V(\vec{r}) = V(\vec{r} + \vec{R})$ with the periodicity $\vec{R}$, then the solutions of the Schrödinger equation take the form

$$\Psi_{\vec{k}}(\vec{r}) = e^{i\vec{k}\vec{r}} u_{\vec{k}}(\vec{r}), \tag{14}$$

with the condition that $u_{\vec{k}}(\vec{r}) = u_{\vec{k}}(\vec{r} + \vec{R})$. This means that the wavefunction can be disassembled into two parts. First, a plane wave $e^{i\vec{k}\vec{r}}$ with the wavevector $\vec{k}$, which serves as a phase factor in $\Psi_{\vec{k}}(\vec{r})$. This phase modulation can be understood as that of a free particle with an identical wavevector $\vec{k}$. Analogous to the momentum of the free particle, we can understand $\hbar\vec{k}$ as the crystal momentum of the state. The second part is a function $u_{\vec{k}}(\vec{r})$ with the same periodicity as the potential. This function depends on the wavevector $\vec{k}$ and is not unique, as multiple functions can fulfill the periodicity condition. In fact, there is an infinite number of stationary solutions $\Psi_{\vec{k}}(\vec{r})$ (Bloch functions) for the Schrödinger equation in such a periodic crystal.

From the periodicity condition for $u_{\vec{k}}(\vec{r})$ it is obvious that also the density of the solutions is periodic, $|\Psi_{\vec{k}}(\vec{r})|^2 = |\Psi_{\vec{k}}(\vec{r} + \vec{R})|^2$. Therefore, it is sufficient to analyze the properties of crystals in their periodic building block, the unit cell. For computational purposes it is generally most efficient to use the smallest possible unit cell, the primitive cell. Larger cells can be reduced to the primitive cell by using the symmetries inherent to the respective system. Mathematically, the available symmetry operations can be described through point groups. A point group combined with the lattice type defines a space group, which fully describes the symmetry of a given crystal.

Stationary states in a crystal depend on both the location $\vec{r}$ in real space as well as the wavevector $\vec{k}$. Therefore, we analyze their properties not only in real space but also in $\vec{k}$-space. The $\vec{k}$-space is commonly referred to as reciprocal space and can be accessed through a Fourier transformation. We can also Fourier transform the crystal's lattice vectors in order to generate a reciprocal lattice. Importantly, the periodicity of the potential

in real space also leads to a periodicity in $\vec{k}$-space in the sense that $\Psi_{\vec{k}}(\vec{r}) = \Psi_{\vec{k}+\vec{G}}(\vec{r})$ for any $\vec{G}$ that is a combination or multiple of the reciprocal lattice vectors. Because of the periodicity, it is sufficient to consider wavevectors $\vec{k}$ in the range $-|\vec{b_j}|/2 \leq k_j \leq +|\vec{b_j}|/2$, with $j = \{1, 2, 3\}$, the reciprocal lattice vectors $\vec{b_j}$ and the components k_j of $\vec{k}$. This defines the primitive Wigner–Seitz cell or first Brillouin zone. For crystals with higher symmetries, the first Brillouin zone can be reduced further without loss of generality into the smallest unique part, the irreducible Brillouin zone.

When calculating the properties of a crystal with density functional theory (or any other method), it is important to consider that the quantities that are calculate depend on the wavevector $\vec{k}$. In a periodic crystal, the KS-states ϕ_j are now the $\vec{k}$-dependent $\phi_{j\vec{k}}$ with KS-energies $\epsilon_{j\vec{k}}$. When we are interested in the overall properties of a crystal, e.g. the total energy, we would in principle need to integrate over the full range of possible $\vec{k}$-vectors. As this is practically not feasible, we instead sample over a number of discrete $\vec{k}$-points. Various sampling schemes are available [77, 78], with the Monkhorst-Pack scheme [79] being commonly used today. It generates a grid of $N_1 \times N_2 \times N_3$ points that are spread out equally along the reciprocal lattice vectors $\vec{b_j}$:

$$\vec{k}_{n_1,n_2,n_3} = \sum_{j=1}^{3} \left(\frac{n_j - \frac{1}{2}}{N_j} - \frac{1}{2} \right) \vec{b_j}, \tag{15}$$

with $n_j = \{1, .., N_j\}$. The exact dimensions $N_1 \times N_2 \times N_3$ that are required have to be determined for every material individually through convergence tests. Commonly used grids range from $4 \times 4 \times 4$ to $10 \times 10 \times 10$ k-points. Generally, a larger cell vector in real space corresponds to a smaller vector in reciprocal space and fewer points that are required in that direction.

In addition to calculating overall properties such as the total energy, we define the density of states (DOS) at an energy E as the number of possible states per volume in the infinitesimal energy range $E + \delta E$. It can be further untangles by projecting the density of states on the orbitals of the different atoms in order to quantify their individual contribution, leading to the projected density of states (PDOS).

Finally, it is possible to calculate the electronic band structure as an overview of the electronic structure of a material. For a fixed j, all energies $\epsilon_{j\vec{k}}$ together form the band with band number j. We define a one-dimensional $\vec{k}$-path, which includes the high-symmetry points, through the multi-dimensional Brillouin zone and calculate the eigenvalues on a finite number of points on that path. The band structure is divided in the occupied va-

lence region as well as the unoccupied conduction region. For semiconductors, valence region and conduction region are clearly separated through a direct or indirect band gap, while the bands overlap for metals.

2.4 The Self-Energy Correction - Hedin's Equations and G_0W_0 Method

A fundamental constraint of DFT is the fact that it is a ground-state theory. All properties are based on the density of the KS-wavefunctions in the ground-state of the system. If the state of a system is modified, for example through the excitation of an electron, this changes the overall density of the many-electron system and therefore affects also the other electrons. This effect implies a certain self-energy possessed by every electron based on its influence on the overall system. However, this interaction inherent to every excitation is not covered by DFT at all. Therefore, a self-energy correction to the energies calculated from DFT is necessary in order to quantitatively predict accurate energies for the unoccupied orbitals and the band gap.

In order to calculate the self-energy, we turn to Hedin's equations [80], which are a set of five equations connected to each other in a self-consistent pentagon.

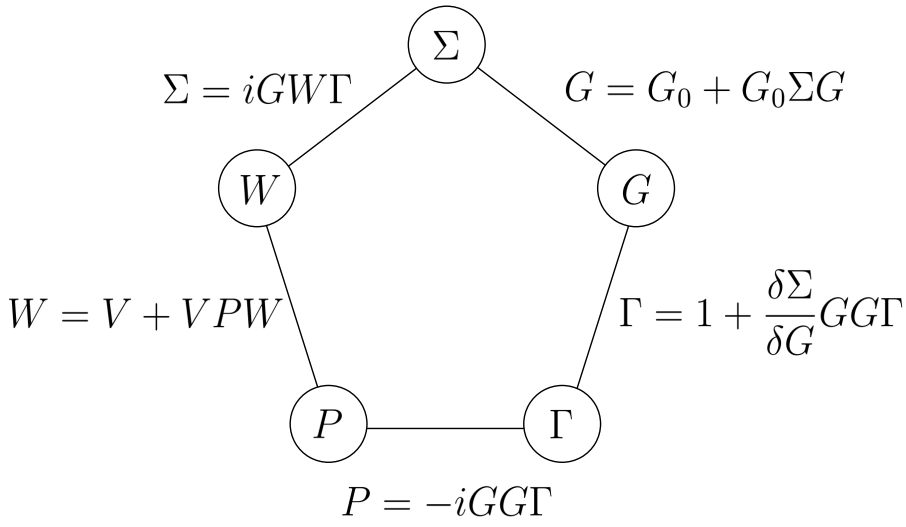

Figure 4: Hedin's pentagon connects the self-energy Σ, the single-particle Green's function G, the screened Coulomb potential W, the vertex function Γ, and the polarization operator P with each other. G_0 refers to the non-interacting single-particle Green's function and V to the Coulomb potential.

Relevant for us is the expression for the self-energy,

$$\Sigma = iGW\Gamma. \tag{16}$$

The vertex Γ depends on the derivative of the self-energy with respect to the Green's function

$$\Gamma = 1 + \frac{\delta\Sigma}{\delta G} GG\Gamma. \tag{17}$$

To move forward, we write Σ as a series and assume that it is sufficient to consider the lowest order term,

$$\Sigma = iGW - GWGWG + ... \approx iGW. \tag{18}$$

This is referred to as the GW-approximation.

In principle, Hedin's equations allow the calculation of G and W in a self-consistent manner. However, in this work we are instead going to use the computationally less expensive single-shot G_0W_0 approach to calculate Σ based on the results from DFT. This is entirely justified, as benchmarks have shown that the increase in computational cost for self-consistent GW calculations does not lead to a corresponding increase in accuracy [81, 82].

Using DFT results as starting point, it is possible to obtain the non-interacting single-particle Green's function G_0 from the KS states. The screened Coulomb potential is calculated as $W_0 = \epsilon^{-1}v_c$ with the frequency-dependent dielectric function of the material ϵ^{-1} and the bare Coulomb potential v_c. The full equation for the electronic self-energy then takes the form

$$\Sigma(r, r', \omega) = \frac{i}{2\pi} \int G_0(r, r', \omega + \omega')W_0(r, r', \omega')e^{i\omega'\eta}d\omega'. \tag{19}$$

With the calculated self-energies from Eq. (19) it is possible to 'correct' the KS-energies from Eq. (7). To this end, we calculate the quasi-particle (QP) energies with the linearized QP equation [83] as

$$\epsilon_j^{\mathrm{QP}} = \epsilon_j + Z_j[\Re\Sigma_j(\epsilon_j) - v_j^{\mathrm{xc}}], \tag{20}$$

with a renormalization factor Z_j to account for the energy-dependence of the self-energy.

2.5 Calculating Optical Properties - The Bethe-Salpeter Equation

Based on the electronic structure of a material calculated either from DFT or with the G_0W_0-method on top of DFT results, it is already possible to estimate the possible optical transitions and their respective energies. However, the electronic structure contains no information on electron-hole interactions, which means that we are limited to an independent particle approximation (IPA) or independent quasi-particle approximation (IQPA) with the G_0W_0-correction. In order to accurately compute optical properties, it is necessary to go beyond this picture and include electron-hole interactions, as they not only shift the energies of the optical transition but may also give rise to completely new excitation that are not available in a single-particle picture.

The electron-hole interactions can be described through the Bethe-Salpeter equation (BSE) [84], which is a formalism to compute bound two-particle states [85]. In this case, we use it to describe bound electron-hole pairs (excitons). The BSE can be expressed as an effective eigenvalue problem for a two-particle Hamiltonian,

$$\hat{H}^{\mathrm{BSE}} \left|A^{\lambda}\right\rangle = E^{\lambda} \left|A^{\lambda}\right\rangle, \tag{21}$$

delivering eigenvalues E^{λ} and eigenvectors $|A^{\lambda}\rangle$ upon diagonalization. The results of the Bethe-Salpeter equation allow us to access optical properties through the eigenvalues and eigenvectors.

The Hamiltonian in Eq. (21) can be split into three terms:

$$\hat{H}^{\mathrm{BSE}} = \hat{H}^{\mathrm{diag}} + 2\hat{H}^{\mathrm{x}} + \hat{H}^{\mathrm{c}}. \tag{22}$$

The diagonal term $\hat{H}^{\mathrm{diag}}$ describes vertical electronic transitions and corresponds to the single-particle picture in the IQPA, while the other terms cover effects beyond the IQPA. The exchange term $\hat{H}^{\mathrm{x}}$, multiplied by 2 due to spin-degeneracy, accounts for the repulsive exchange interaction between the fermionic electron-hole pairs, and the direct term $\hat{H}^{\mathrm{c}}$ describes the attractive electron-hole Coulomb interaction.

The BSE can be solved efficiently by adopting a suitable two-particle basis split between excitation (resonant part) and deexcitation (anti-resonant part) [86]. The coupling between resonant and anti-resonant part is usually neglected (Tamm-Dancoff approximation) because it does not have a large impact on the results [86].

The solution of the BSE provides information on the energies of the possible optical excitations through the eigenvalues E^λ as well as on the properties of the created excitons through the eigenvectors $|A^\lambda\rangle$. In particular, it is possible to formulate the imaginary part of the macroscopic dielectric function, which corresponds to the optical absorption spectrum, as a sum of Lorentzian functions centered around the eigenvalues,

$$\Im\epsilon_M \propto \sum_\lambda |\mathbf{t}_\lambda|^2 \left(\frac{\Gamma^2}{(\omega - E_\lambda)^2 + \Gamma^2} \right). \tag{23}$$

Eq. 23 includes the energies E_λ of the single excitations as well as their transition coefficients $\mathbf{t}_\lambda$, which are calculated from the results of the BSE as a sum of dipole-transition matrix elements weighted by the associated eigenvectors. The value of the broadening Γ is arbitrary. The full function $\Im\epsilon_M$ includes positive Lorentzian functions to describe excitations as well as negative functions that describe deexcitations:

$$\Im\epsilon_M = \frac{4\pi^2}{\pi\Gamma\Omega} \sum_\lambda |\mathbf{t}_\lambda|^2 \left(\frac{\Gamma^2}{(\omega - E_\lambda)^2 + \Gamma^2} - \frac{\Gamma^2}{(\omega + E_\lambda)^2 + \Gamma^2} \right), \tag{24}$$

with the volume Ω of the unit cell [87].

2.6 Computational Tools and Parameters

In order to execute the calculations outlined above, we used already established codes.

The pure DFT calculations in Chap. 3 were performed with the code `CP2K` [88]. In the framework of this code, atomic cores are represented through pseudpotentials instead of being treated explicitly. We used the Godecker–Teter–Hutter (GTH) pseudopotentials [89] in combination with the MOLOPT basis sets [90] `DZVP-MOLOPT-SR-GTH` (low level calculations) and `TZV2P-MOLOPT-SR-GTH` (high level calculations) based on Gaussian functions. As functional we used `r2SCAN` [91], which has already been shown to offer a good combination of accuracy and manageable computational cost for alkali based crystals [92]. Detailed computational parameters were converged through the workflow presented in that chapter.

For the DFT + MBPT calculations in Chap. 4 and 5, we used the code `exciting` [87, 93]. Contrary to `CP2K`, it employs an all-electron full-potential formalism. The basis is a mix of linearized augmented plane waves and local orbitals, with the boundary defined by the Muffin-tin radii of 2.0 bohr for alkali atoms and 2.2 bohr for antimony atoms. As the DFT

results in this part form merely the starting point for further calculations, it is sufficient to use the PBE-sol functional [94]. In the G_0W_0 part, the dielectric screening is calculated in the random-phase approximation (RPA). The BSE calculations are performed in the Tamm-Dancoff approximation and the static screening is also calculated in the RPA. The number of empty states included in the various steps as well as the local-field cutoff and k-meshes were carefully converged manually. In all cases we use 200 empty states to calculate the G_0W_0-screening, 100 empty states to calculate the BSE-screening, and a local field cutoff of 1.5 Ha in the BSE. Detailed k-meshes of the single steps are reported in the appendix, part A.

2.7 Existing Photoemission Models from the Literature

Over decades of photocathode research there has always been the drive to understand the experimental data through theoretical models and simulations. The first fundamental phenomenological frameworks were developed in the 50s and 60s [31, 43, 95] and laid the foundation on which many more models were developed. The initial works featured a semi-empirical approach, where analytical expressions for the photoemissive yield were derived with free parameters to be fitted to the experimental data. Generally, a simplified electronic structure of the photocathode materials was assumed, as more complicated cases could not be covered. The advance of computational methods like DFT has allowed for the implementation of more advanced schemes with impressive predictive power [35, 44, 45].

As anticipated in the introduction, we base our conceptualization of the photoemission process on the three-step model or Berglund-Spicer model of photoemission. It was originally established by W. E. Spicer's pioneering work on photoemission in alkali antimonides in 1958 [31] and theoretically developed in a work of Berglund and Spicer published in 1964 [43]. In this model, we think of photoemission as a process consisting of three relevant sequential steps. First, photoexcitation in the crystal generates exited electrons (I). Second, the motion of these electrons through the crystal and all events that take place during it (II), and finally the escape of the electrons through the surface into the vacuum (III).

In the original work by Spicer, key parameters were fitted to the collected experimental data. This approach has, generally speaking, been quite successful, in particular for polycrystalline photocathodes. However, with the advance of experimental growth tech-

niques improvement is required also for the theoretical methods in order to properly cover the physics of more complicated systems like thin-film heterostructures. Nowadays, many models are integrated into *ab initio* workflows, using results from first principles to predict the photoemissive yield. This allows a screening of different materials and in particular also the analysis of the effects of specific structural or chemical modifications.

Among the more recent works is a workflow published by Antoniuk et al. in 2020 [45], which is based on the electronic structure of materials calculated with DFT. It uses Fermi's golden rule and the possible Bloch states from the electronic structure to determine the probabilities of photoexcitation in the crystal and photoemission into the vacuum. This ultimately leads to the intrinsic emittance of the compound, with scattering during transport being neglected.

Another DFT-based scheme was proposed by Saha et al. in 2023 [46] based on the density of states of the materials. The occupation probability in the density of states is treated through a Fermi-Dirac distribution, leading to an excitation probability that is assumed to be the product of occupied states at an initial energy and unoccupied states at the target energy. Again, transport is not treated explicitly and the emission probability is assumed to be directly proportional to the kinetic excess energy after overcoming the surface.

Common to these methods relying on DFT is that they have to simplify how they treat interactions between particles. As DFT is a ground-state theory, electron-electron and electron-hole correlations are not included. Instead, the electrons are approximated as independent particles whose interactions are covered only by a mean-field approach. A common issue with this is that band gaps have to be artificially corrected to match the experimental values, as seen for example in the mentioned paper by Antoniuk et al. [45]. More importantly, photoexcitation is evidently a process that goes beyond the ground-state. To fully describe it, a many-body picture is required.

Before moving on to our own work, we give a short breakdown of other models from the recent literature. These are mainly aiming at metal photocathodes, while our own model will be designed for semiconducting materials.

Jensen et al. presented a time-dependent model in 2006 [96], which takes into account thermal propagation due to laser heating. It cover various material and laser parameters. This model was originally designed for metals only, but expanded in a follow-up in 2008 [97] to cover semiconductors, being successfully applied to Cs_3Sb and CsK_2Sb.

The Dowell-Schmerge Model [98, 99] is another framework specifically for metal photocathode. A Fermi-Dirac distribution is used for the electrons and expressions are derived for quantum efficiency and emittance.

Finally, there is the 1-step model [100], which treats photoemission in metals as a single process. Optical transitions are again treated through Fermi's golden rule. With this, the quantum efficiency is calculated, allowing different polarizations and angles of the incoming beam. In this model, scattering is incorporated by using an effective scattering length.

While the preceding works have not been unsuccessful, we wish to go beyond the picture of DFT and instead use the methods from many-body theory presented in the previous subchapters, namely G_0W_0 and BSE. With this, we are able to accurately cover the electronic and optical properties of even the most complex materials. In particular, our model should be able to produce good predictions for the photoemissive yield without the need for empirical parameters or adjustments.

3 High-Throughput Studies for Alkali Antimonide Binary Crystals

After reviewing the available background and literature, we are now going to present our own work on photocathode materials. Before developing the desired implementation of the three-step-model, we start by collecting more data on alkali antimonides through preliminary *ab initio* studies. In this section, we analyze binary alkali antimonide crystals via a high-throughput screening based on DFT, focusing on Na and K as cations. A corresponding study with Cs is already available in the literature [101]. These binary crystals are relevant for the purpose of understanding intermediate, meta-stable, and possible polycrystalline phases that can appear during the crystal growth process. By performing automated DFT calculations for hundreds of compounds, we want to understand which stoichiometries and crystal arrangements are energetically favored. For stable crystals we proceed with a further analysis of their electronic properties, in particular their band structures and projected density of states. At this point, we are going to perform calculations with ground-state DFT in order to assess the basic properties of a large number of binary alkali antimonides without excessive computational cost. This part lays the groundwork for our further studies. For the execution of the high-throughput calculations we use the in-house library `aim²dat` [102] based on AiiDA [103, 104].

3.1 Initial Structure Pool and aim²dat Library

The first preliminary step is the creation of an initial structure pool containing the crystals that are going to be analyzed. This can be accomplished by mining data from established computational databases. In this work we drew crystal structures from both Materials Project (MP) [105, 106] and the Open Quantum Materials Database (OQMD) [107, 108]. As we want to analyze the properties of K-Sb and Na-Sb binary crystals, we create two pools, one with all crystals containing K and Sb and one with all crystals containing Na and Sb. As we are drawing structures from two separate databases, this approach leads to many duplicates in the structure pool. To be computationally efficient, these need to be filtered out before running any calculations.

While the exact technical definition of what constitutes a duplicate is not as straightforwards as it may seem, this problem has been encountered and solved before. In the F-fingerprint method [109, 110], an abstract crystal fingerprint space is created. Every crystal structure is connected with a vector in this multidimensional space, the 'fingerprint'. The elements of this vector are defined through the pairwise partial radial distribution function of atomic pairs in the crystal structure. Each structure can be described

uniquely by a fingerprint vector, which is unaffected by changes to the coordinate system, rotations, and reflections. The distance between the vectors in this multidimensional space can be quantified through their cosine distance (or alternatively the Minkowski distance). By design, a short distance in the fingerprint space corresponds to a similarity in structure. Thus, we can transform all crystal structures in the pool into the fingerprint space and easily filter out duplicates, as their structural similarities are evident there.

The next issue which arises is, that the number of distinct crystal structures is rather small after filtering. Each structure pool consists of only around 50 binary crystals. In order to address this, we download additional crystals with similar elements and then substitute them with K / Na and Sb. We can consider Na and Li for substitution with K, K and Li for substitution with Na, and As and Bi for substitution with Sb. From this extended structure pool duplicates are again removed. In this case, a harsher filter based on composition and space group is applied. After this procedure, the final initial structure pool consists of 166 crystals for K-Sb, among them 91 binary phases and 147 crystals for Na-Sb, among them 79 binary phases. The properties of the crystals in the structure pool are then calculated through a workflow that is visualized in Fig. 5.

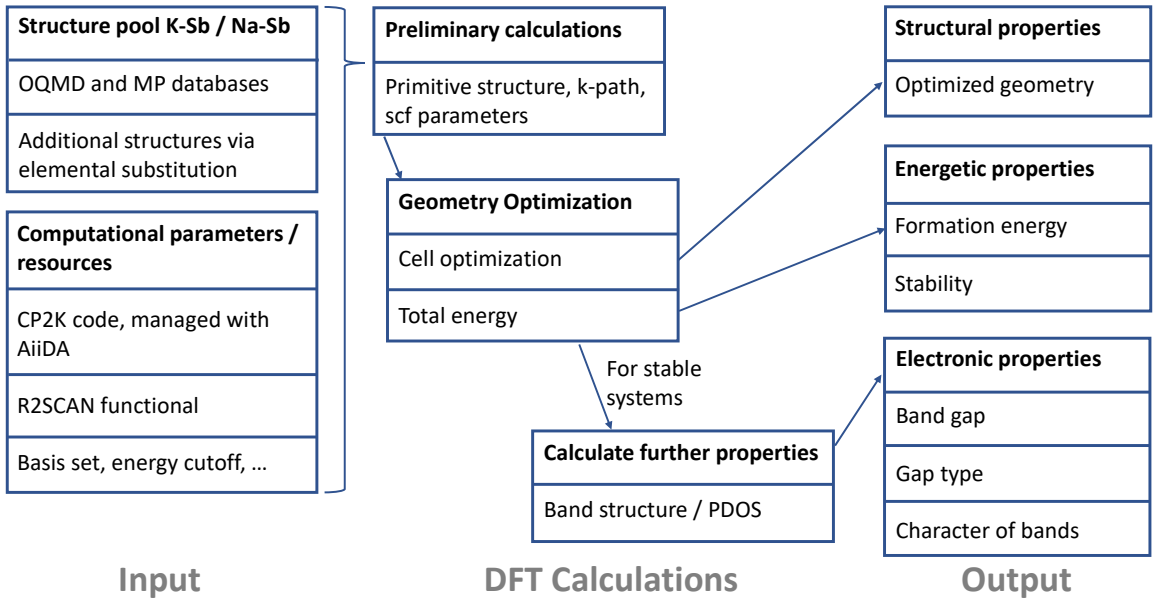

Figure 5: The computational workflow used in this section. From a group of initial structures and input parameters, a series of DFT calculations is run to determine structural, energetic, and electronic properties.

In addition to the initial structures, various computational parameters and resources have to be chosen before starting to run calculations. All results in this chapter were calculated with the code `CP2K` [88] and the functional `r2SCAN` [91]. With this 'input' we then embark on a series of DFT calculations. For these calculations, the crystal structures are reduced to their primitive unit cell. This can be done with the tool `seekpath` [111], which in turn is based on the `spglib` [112] library. In addition to providing the primitive cell, `seekpath` identifies the space group of the crystal and determines a suitable k-path through the Brillouin zone for later band structure calculations.

As first step, a set of preliminary DFT calculations is run in order to determine suitable parameters for the 'real' calculations, as tight as necessary for convergence. Then the initial crystal geometries are optimized with the chosen set of parameters. While the imported structures were already pre-optimized, repeating the optimization ensures that all crystals are optimized with the same set of computational parameters, which are also usually on a higher level than what was available before. To save computational resources, the cell optimization is split into two subsequent steps, a first one with course parameters and another one with tighter parameters to reach the final converged structure. These cell optimizations were done for all crystals in the two initial structure pools. In addition to the optimized geometry, this yields the total energy of the crystal unit cell. The total energy determines the energetic properties of the compounds and allows us to filter out all crystals that are not stable. This will be discussed in more detail in the next subchapter. The workflow then continues with only the stable crystals and includes the calculation of further electronic properties for the stable compounds, namely band structures and the projected density of states. All of the output can then be analyzed to better understand the properties of this class of materials.

As mentioned before, the outlined calculations were managed with the library `aim`^{2}`dat`, which in the original form that was used in this work was designed and implemented by H.-D. Saßnick. It allows us to manage and execute the hundreds of DFT calculation needed for the crystals in the structure pool, which would hardly be feasible by hand. In addition to automatically generating the input files for the calculations with `CP2K`, the AiiDA toolkit provides an interface to automatically interact with computer clusters and to submit jobs there. In particular, it allows the implementation of workflows of sequential calculations, where the next job is launched once the previous one is completed. This aligns with the requirements of the planned high-throughput study and allows schemes like the cell optimization in two steps with coarse and tight parameters, which would be very tedious to setup and execute manually. Furthermore, AiiDA provides a data storage

system, in which all generated data and metadata is saved in data nodes. These nodes are connected through a web of data provenance, which allows it to extract all the (meta-)data connected with a certain process or calculation without problems. With this system, it is straightforward to share complete datasets with all their computational parameters also with people that are completely unaffiliated with the original calculations.

3.2 Energetic Stability

The first important result from the high-throughput workflow is the formation energy of the considered crystals, which will provide us with information on the stability of the compounds. For a crystal X_xSb_y with X = (K, Na) it is defined as

$$E_{form}(X_xSb_y) = \frac{1}{x+y}(E(X_xSb_y) - xE(X) - yE(Sb)). \tag{25}$$

$E(X_xSb_y)$ is the total energy of the K_xSb_y or Na_xSb_y system, while $E(K)$, $E(Na)$, and $E(Sb)$ are the energies per atom of the most stable elemental phase for each atomic species. In all cases, x and y refer to the number of atoms of the respective atomic species in the unit cell. The pre-factor $\frac{1}{x+y}$ is necessary to normalize the formation energy to an energy per atom for comparison between unit cells with a different total number of atoms.

The formation energy of a crystal is required to be negative in order for it to form, otherwise it would be more energetically favorable for separate elemental phases to coexist. However, a negative formation energy does not necessarily imply that a compound is stable, as there might be other possible crystals at the same stoichiometry that are energetically more favorable, or it might be favorable for a crystal to split between more than one crystalline phase. The subset of crystals that are stable is given by the convex hull in a phase diagram and the crystals that are directly on it. With it, we can define the stability of a crystal as the distance between the formation energy of this crystal and the convex hull. For fully stable crystal, it is 0 (eV / atom).

The formation energies that were calculated for the K-Sb and Na-Sb binary crystals are shown together with the convex hull in phase diagrams in Fig. 6 (a) and (b), respectively. They show the stability of the possible compounds at varying relative content of the alkali species. Different crystal symmetries are indicated with different symbols.

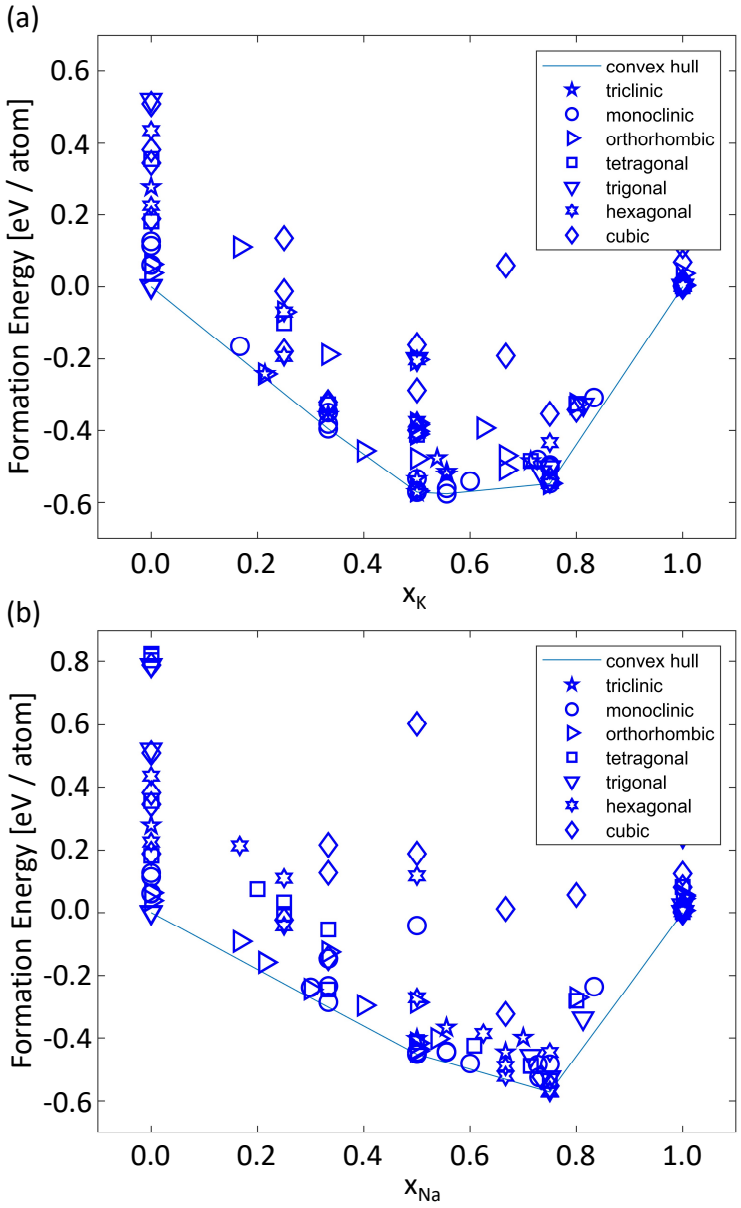

Figure 6: Phase diagrams for (a) K-Sb and (b) Na-Sb crystals. The formation energy per atom is given as a function of the ratio x_K (x_{Na}) of K (Na) atoms in the crystal. By definition, the formation energy of the most stable elemental phases is set to zero. The convex hull is indicated with a solid line.

In both cases, there is a large number of crystals on or in close vicinity of the convex hull. Especially at x = 0.5 and x = 0.75, corresponding to alkali:antimonide ratios of 1:1 and 3:1, there are many different possible systems with varying symmetry and formation energy in both the K-Sb and Na-Sb phase diagrams. However, it is important to remember that the number of analyzed compounds at a certain stoichiometry is directly dependent on how many crystal are available in the used databases. We can assume that there is a strong bias towards the 1:1 and 3:1 ratios as they are usually targeted experimentally and have been analyzed in previous works. A more complete study over all ratios would be

possible by generating and analyzing a large number of random crystal structures, going beyond the data that is currently available online. An efficient implementation of such an approach is possible by identifying promising structures through machine learning [113]. However, this goes beyond the scope of the presented work.

Looking at Fig. 6 in more detail, we find remarkable differences between the phase diagrams of the K-Sb and Na-Sb crystals. As visible in panel (a) for K-Sb, for a low ratio of potassium there are a few monoclinic and orthorhombic crystals very close or on the convex hull between $x_K = 0.17$ and $x_K = 0.4$. After this a plateau appears between 0.5 and 0.75 with a large number of crystals, many of them close to the convex hull. Above $x_K = 0.75$, a few more structures have been calculated, but they are not predicted to be stable. The Na-Sb crystals in panel (b) show a similar picture, with many data points mirroring the structures of K-Sb. Also here there are multiple monoclinic and orthorhombic crystals close to the convex hull between $x_{Na} = 0.17$ and $x_{Na} = 0.4$. Above that we find again a multitude of polymorphs very close to the convex hull, mainly with monoclinic, triclinic and hexagonal lattices up to $x_{Na} = 0.75$, followed by a few unstable compounds at higher sodium ratios.

Significant differences are notable when considering the overall shape of the convex hull. In the phase diagram for K-Sb in part (a), the global minimum is at the ratio $x_K = 0.56$ for the monoclinic crystal K_5Sb_4. Around it, the convex hull forms the mentioned plateau between $x_K = 0.5$ and $x_K = 0.75$. For Na-Sb in part (b) on the other hand, the global minimum is at $x_{Na} = 0.75$ with a hexagonal Na_3Sb crystal. Instead of a plateau, the formation energies around the minimum decrease and then increase more rapidly. Apart from the shape of the convex hull, it is also visible that for the K-Sb binaries there are many compounds almost directly on the convex hull for ratios apart from 1:1 and 3:1, while for Na-Sb many crystals are a bit above the convex hull and therefore predicted to be not completely stable.

Overall, the large number of crystals on the convex hull shows that it is indeed likely for polycrystalline phases to form, as there is a large number of possible stable compounds. This is especially true for the K-Sb crystals with their plateau in energy between alkali:antimonide ratios of 1:1 and 3:1. According to our results, it is also possible for separate exceptionally Sb-rich phases to form, as stable compounds exist in this region. On the other hand, special Sb-poor phases beyond the 3:1 ratio are not possible. Ultimately, the large number of crystals identified as stable shows in turn the importance of this study to understand their properties.

After identifying the energetic properties of the alkali antimonide crystals, we now want to understand which electronic properties can appear at the different alkali:antimony ratios. For this, we are going to limit our study on the stable compounds that can appear in experimental photocathodes. We consider crystals to be stable when they are within 50 meV from the convex hull, which accounts mainly for the thermal energy at room temperature. With this threshold, there is a multitude of different K-Sb crystals included, while for Na-Sb many compounds are slightly above the 50 meV barrier. For the following study, we focus on the electronic properties of six K-Sb and six Na-Sb crystals that can be seen as representative of different alkali-antimony ratios. The chosen structures are visualized in Fig. 7. We start with one example of an antimony-rich system in each case, which is monoclinic K_2Sb_4 for K-Sb and orthorhombic $Na_{12}Sb_{44}$ for Na-Sb. Afterwards, we consider the equistoichiometric case with two different crystals, one with a small and one with a large unit cell: monoclinic K_2Sb_2 and K_8Sb_8 as well as triclinic Na_2Sb_2 and monoclinic Na_8Sb_8. Additionally, there is the monoclinic K_5Sb_4 crystal close to the 1:1 ration, which we analyze exclusively for K-Sb because it corresponds to the global minimum there. Finally, we take a look at the experimentally very relevant 3:1 ratio, where we consider largely identical cubic and hexagonal crystals for K_3Sb and Na_3Sb as well as another different cubic phase for Na-Sb with distinct properties.

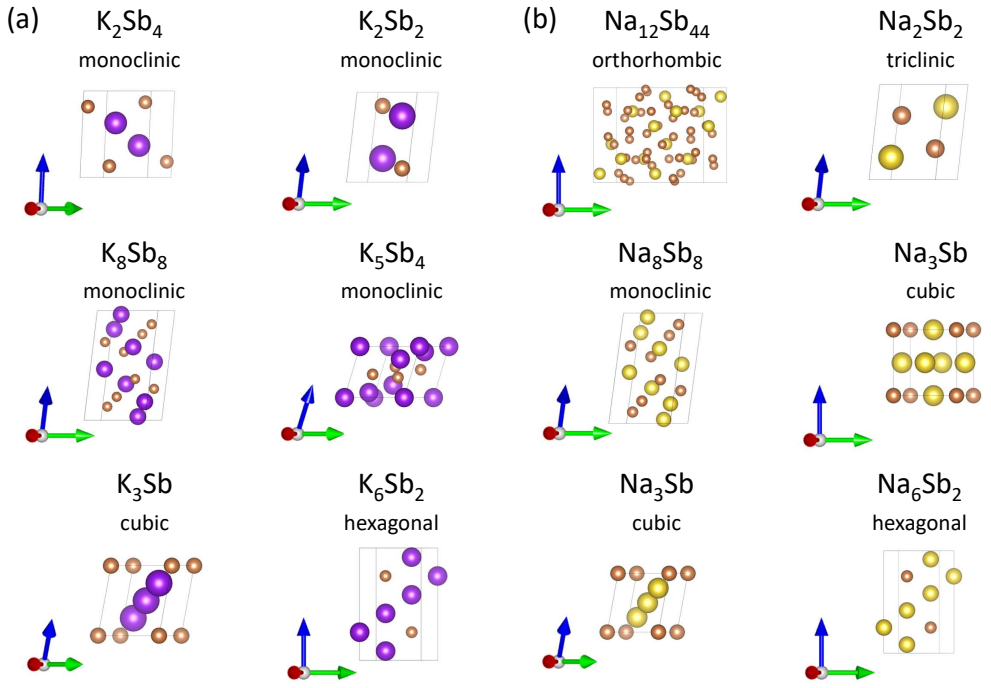

Figure 7: Chosen stable structures with (a) K-Sb and (b) Na-Sb composition. Na atoms are depicted in purple, K in yellow, and Sb in bronze. The coordinate system is indicated by the colored arrows.

3.3 Electronic Properties from DFT

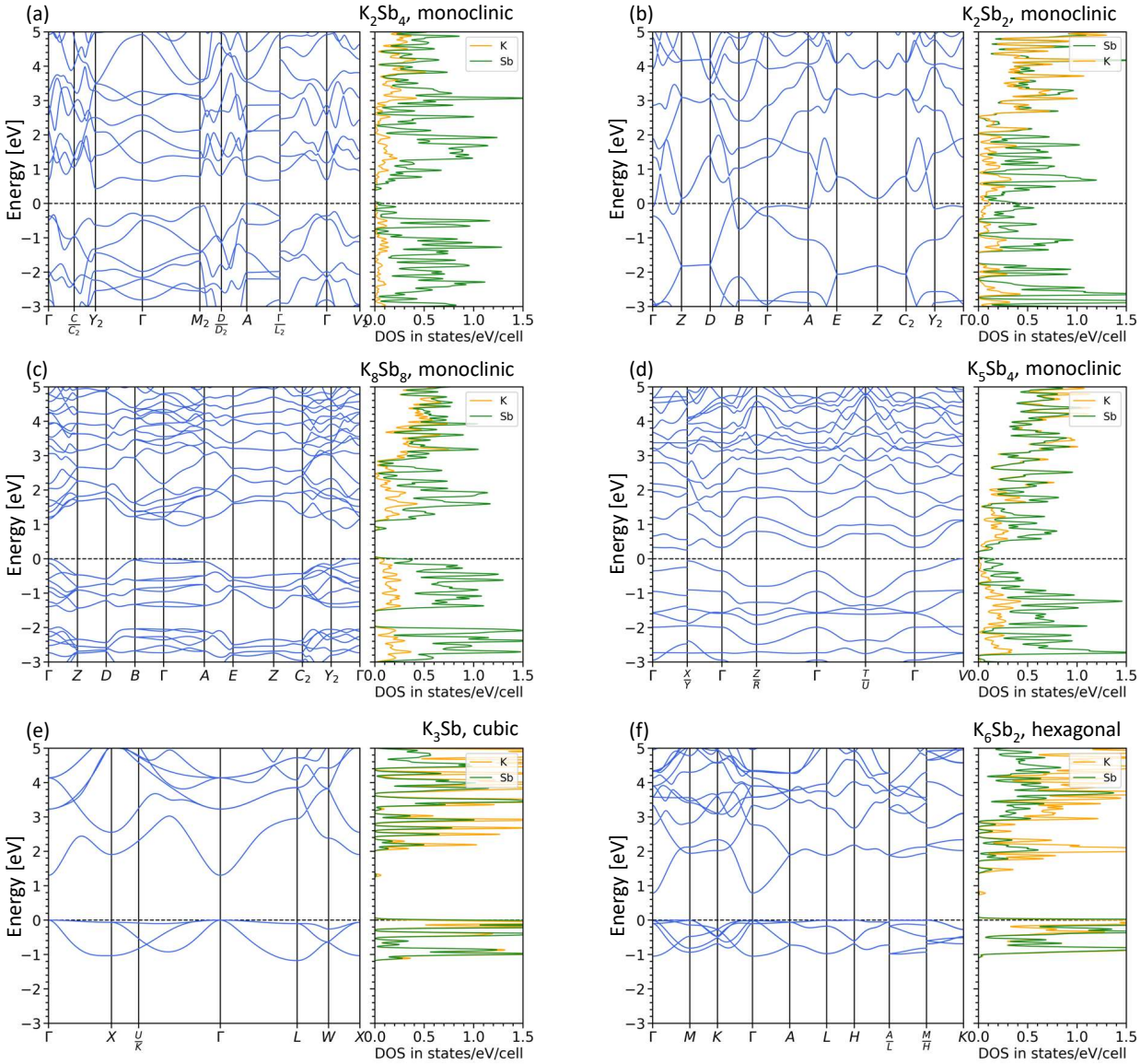

Figure 8: Band structures and PDOS of selected stable K-Sb binaries. The energy scale is aligned to be zero at the valence band maximum for semiconductors and the Fermi energy for metals.

For the selected exemplary crystals shown in Fig. 7, we calculate and plot the band structures as well as the PDOS in order to gain valuable insights into their electronic properties. The first example is the Sb-rich monoclinic K_2Sb_4 shown in Fig. 8(a). It has a band structure with the VBM at the high-symmetry point A and the CBm at the high-symmetry point Y. The indirect band gap between these points is 0.43 eV, while the

smallest direct gap is 0.73 eV and not located at a high-symmetry point. From the PDOS it is visible that both the occupied and the unoccupied bands are dominated by contributions from Sb states, which is expected for an Sb-rich crystal. In particular, the top of the valence region and the bottom the conduction region consist solely of Sb states, showing that the low fundamental gap stems from a transition between Sb orbitals. Interestingly, the level of dispersion of the bands varies a lot between the different regions in the Brillouin Zone, as visible in the plot. For example we see almost a plateau for the highest occupied and lowest unoccupied band on the path from Y_2 to Γ to M_2, highlighting their non-dispersive character in this region. Meanwhile, the VBM-1 is strongly dispersive in the same region. On the path from Γ to C, on the other hand, all bands both occupied and unoccupied show a highly dispersive character.

Next, we take a look at the electronic structure of the crystals with equal potassium and antimony content. In Fig. 8(b), there is the band structure and PDOS of a metallic crystal, monoclinic K_2Sb_2. The band structure is characterized by highly dispersive bands crossing the Fermi energy. Notably, the PDOS shows that the occupied bands as well as the unoccupied bands at low energy (up to about 2 eV) are characterized by contributions from Sb states, while K states become dominant at higher energies. The other crystal that we analyze at this ratio is monoclinic K_8Sb_8 with a larger unit cell of 16 atoms in Fig. 8(c). It has a large number of bands due to the larger number of atoms in the unit cell. Many of the bands become pairwise degenerate in certain regions of the Brillouin Zone, while being distinct in others. In the occupied region, most bands show a very low dispersion, which is characteristic of Sb p-orbitals and corresponds to the large influence of Sb states visible in the PDOS for the valence region. In the lower conduction region, Sb states are also dominant, but there is an additional significant contribution from K states. This correspond to the higher band dispersion in this energy region and the hinted parabolic shape of the CBm, which usually is a sign of the s-orbitals of potassium. Overall, we can also assume that the large number of atoms and core electrons reduces the dispersion of the bands compared to the K_2Sb_2 crystal with a much smaller unit cell. Quantitatively, the K_8Sb_8 crystal is a semiconductor with an indirect gap of 0.88 eV between Y_2 and Γ, while the direct gap is only about 10 meV smaller than the indirect band gap due to the low dispersion of the VBM. The comparison between these two materials shows how two crystals, even though they have the same composition and symmetry group, can yield significantly different electronic properties.

Moving on to panel (d) of Fig. 8, we see the results for the interesting and energetically very favorable monoclinic crystal K_5Sb_4. It is a semiconductor with a very small indirect band gap of 0.25 eV. The VBM is located at the point V, while the CBm is at X.

The band structure is a mix of bands with low dispersion, for example the VBM-6, which is almost entirely flat, with a few bands that are more dispersive. A striking feature are pseudo-parabolic states in the lower conduction bands, which show local minima at Γ. These can again be connected with K s-orbitals, as supported by the fact that K and Sb states contribute almost equally to the DOS at the bottom of the conduction region. The top of the valence region, on the other hand, is again dominated by Sb states.

Finally, there is the important and experimentally observed 3:1 ratio. For this ratio, we show the electronic structure of the calculated cubic phase in panel (e) and of the hexagonal phase in panel (f) of Fig. 8. The band structures are unsurprisingly very similar and show the typical features of these alkali antimonides. The highest occupied band shows almost no dispersion over the entire Brillouin Zone and has the VBM at Γ. It consists of Sb p-states partially hybridized with states from K. The lowest unoccupied band on the other hand is highly dispersive with a parabolic shape and the CBm also at Γ. Its character stems from s-states of potassium. This overall character is largely identical for both crystals. The main difference is that the hexagonal phase contains double the atoms in its unit cell due to the lower symmetry, which leads to a larger number of distinct bands in the electronic structure. Also the absolute value of the band gap changes, it is 1.3 eV for the cubic phase and 0.8 eV for the hexagonal phase, which is a significant reduction.

Overall, we find numerous similarities between the electronic structures of the considered K-Sb crystals. With the exceptions of the very Sb-rich phase K_2Sb_4 and the metallic crystal, the transition through the band gap is characterized by a top of the valence region that is strongly influenced by Sb states, hybridized with a varying degree of K states. The bottom of the conduction region shows a stronger influence of K states, which manifests itself mainly through the parabolic and pseudo-parabolic bands in the electronic structure. These highly dispersive bands are also responsible for the fact that all the analyzed K-Sb crystals show very low band gaps, which remain below 1 eV with the exception of cubic K_3Sb.

Next, we are going to consider the electronic structure of the Na-Sb crystals shown in Fig. 9 in order to assess how the different alkali species changes the electronic properties.

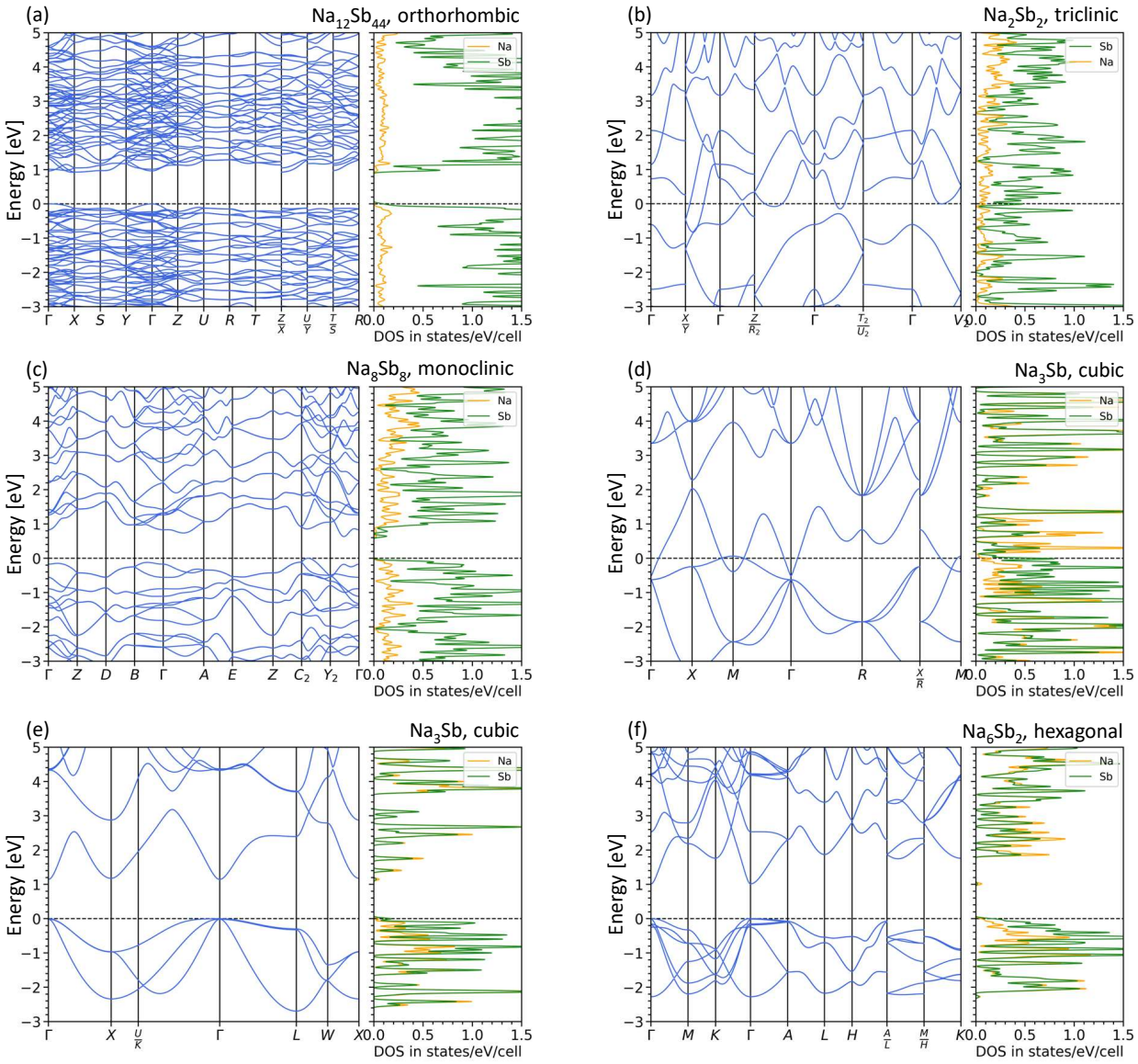

Figure 9: Band structures and PDOS of selected stable Na-Sb binaries. The energy scale is aligned to be zero at the valence band maximum for semiconductors and the Fermi energy for metals.

Starting again with an Sb-rich compound, the band structure of orthorhombic $Na_{12}Sb_{44}$ is shown in Fig. 9(a). This also serves as an example for a crystal with a very large number of atoms in its unit cell, 56 in total. The large number of atoms leads to a very dense band structure with many distinct bands, even though some become pairwise degenerate in certain parts of the Brillouin Zone also here. As seen previously for K_8Sb_8, the large unit cell gives rise to a low band dispersion throughout the entire Brillouin zone. Nevertheless, the material has a clearly defined band gap with a direct gap of 0.96 eV at Γ. A pseudo-parabolic shape of the band structure is visible for both the VBM and CBm. From the PDOS, it is evident that the bands are completely dominated by contributions from antimony states, as expected for a crystal with a much larger ratio of Sb than Na.

Next, we consider again the case of equal alkali and antimony concentration with two different examples. Similar to the metallic monoclinic K_2Sb_2, the electronic structure of triclinic Na_2Sb_2 in Fig. 9(b) is characterized by strongly dispersive bands over the entire Brillouin Zone. Contrary to K_2Sb_2, where K states became prevalent at higher energies, the PDOS of Na_2Sb_2 is dominated by Sb states over the entire shown energy range. For practical purposes more relevant is the electronic structure of monoclinic Na_8Sb_8 in panel (c). This crystal is directly related to the K_8Sb_8 crystal discussed above and their band structure is similar. Again, there is a large number of bands, which are distinct in certain regions of the Brillouin Zone and degenerate in other. An example for this are the lowest two unoccupied bands, which 'merge' on the path from A via E and Z to C_2. This compound is an indirect band gap semiconductor with a fundamental gap of 0.63 eV and a direct gap of 0.81 eV. The VBM appears between C_2 and Y_2, while the CBm is located between Y_2 and Γ. The smallest direct gap is also at a point between Y_2 and Γ. Notably, the dispersion of the bands is slightly larger than for the related K_8Sb_8 crystal and there are fewer flat parts of the band structure. This can be related to the fact that sodium is a lighter atom than potassium and possesses fewer core electrons to 'stabilize' the energy of the bands.

In this case, we are going to omit the 5:4 ratio and instead start our discussion of the 3:1 alkali:antimony ratio with another metal. This material, with its electronic structure shown in Fig. 9(d), is a metallic crystal with cubic symmetry. It is characterized by highly dispersive bands crossing the Fermi energy. In this case, most of the bands have a clear parabolic shape, much more so than for Na_2Sb_2 discussed above. This is related to the stronger influence of Na states visible in the PDOS. The shown electronic structures of the other analyzed phases of Na_3Sb in Fig. 9(e) and (f), on the other hand, closely resemble that of the K_3Sb crystals with the same symmetries. The cubic Na_3Sb crystal has a direct band gap at Γ of 1.14 eV and again shows the parabolic band structure at the

CBm associated with an alkali s-orbital. Contrary to the analyzed K_3Sb, we see another local minimum at almost the same energy at the high-symmetry point X, only 32 meV above the CBm. The VBM at Γ remains rather flat, but does show a larger dispersion than for the related K-Sb crystal. A similar behavior is visible for the electronic structure of the hexagonal crystal in (f), where all the bands show a higher dispersion than for the hexagonal K_6Sb_2 crystal. This crystal also has a direct band gap at Γ, which in this case is 1.0 eV large.

Altogether, the electronic structures of the Na-Sb crystals show significant similarities to that of the respective K-Sb crystals. Again, we find the characteristic parabolic states associated with alkali metals in the lower conduction region. The upper valence region remains generally rather flat, but shows a clearly higher dispersion than for the related K-Sb compounds. This can be rationalized through the fact that sodium is a significantly lighter atom than potassium. Also for the Na-Sb crystals band gaps are rather small and remain at around 1 eV.

After taking a detailed look at the electronic structure of specific representative structures, we will now move back to the larger picture by analyzing the overall trends of the electronic structure of these materials. While the details of the band structures are difficult to compare automatically in a high-throughput framework, we can make a direct comparison between the calculated band gaps. We will compare both the quantitative value of the gap as well its qualitative nature by discriminating between direct and indirect band gaps as well as metals. The results of this analysis are shown in Fig. 10 as a function of the relative alkali content for the stable crystals that were calculated in the workflow.

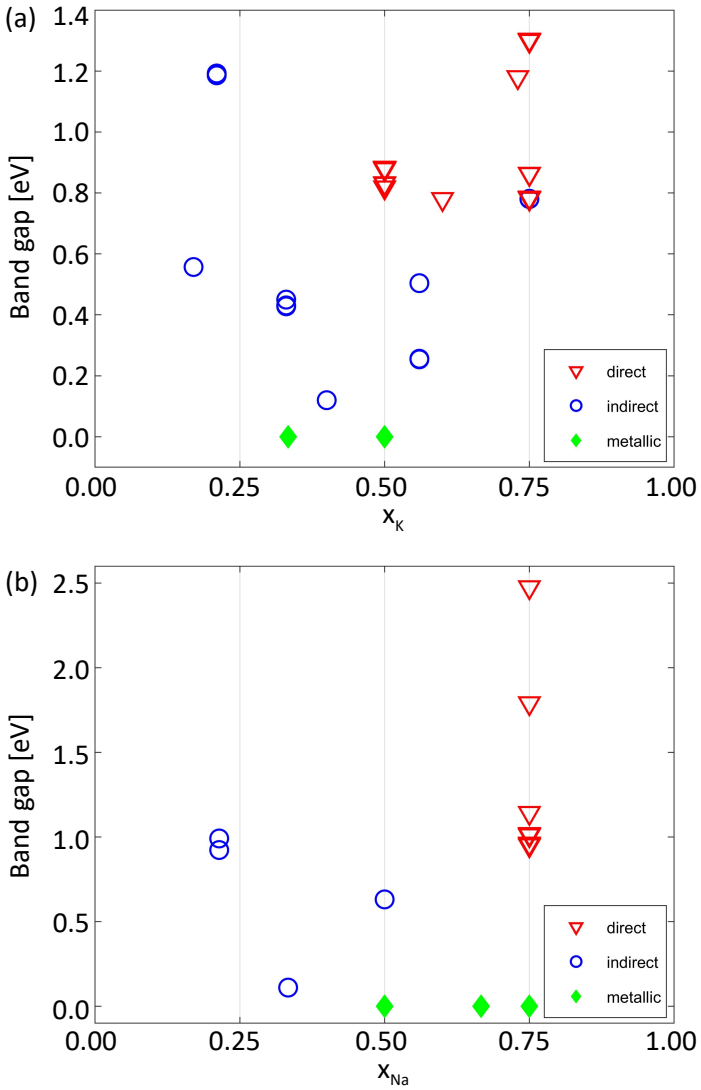

Figure 10: Calculated band gaps of stable (a) K-Sb and (b) Na-Sb binary crystals as a function of the alkali ratio x_K (x_{Na}). We distinguish between direct and indirect band gaps through red triangles and blue circles. Metals are plotted as green diamonds.

Starting again with the K based crystals in panel (a), clear trends can be identified. The crystals with a low ratio of potassium show indirect band gaps ranging from 0.4 to 1.2 eV. For the crystals with a high ratio of K on the other hand, we find direct band gaps which also tend to be larger, ranging 0.8 to 1.3 eV. For crystals with similar K and Sb content the situation is not as clear. There are three crystals at $x_K = 0.5$ with similar direct band gaps of around 0.8 to 0.9 eV. However, we also find multiple crystals with very low indirect gaps of 0.3 eV and 0.5 eV at close to equiatomic ratio, as well as multiple metallic structures.

Similarly, there are clear trends for the stable Na-Sb crystals shown in Fig. 10(b), even though the number of analyzed stable crystals is not as large for these compounds. In the Na-poor region of the plot, crystals with small indirect band gaps ranging from 0.1 to 1.0 eV appear. For Na-rich crystals, there are multiple structures at $x_{Na} = 0.75$ with direct gaps ranging from 0.9 eV to 2.4 eV. Between these parts there are various metallic compounds as well as an equiatomic structure with an indirect band gap of 0.6 eV.

In summary, we have used a high-throughput workflow based on DFT to analyze the energetic stability as well as the electronic properties of binary crystals composed of K / Na and Sb. We generated an initial structure pool based on the materials available on computational databases, for which we then calculated the formation energies after a structural relaxation. With this, we could plot the convex hull and rank the stability of the various structures based on their distance to the convex hull. This analysis revealed that there is indeed a large number of possible stable crystals, especially close to the experimentally important alkali:antimony ratios 1:1 and 3:1, motivating a further analysis of the electronic properties of the stable crystals. A direct comparison between K-Sb and Na-Sb crystals showed many similarities, as largely identical structures are energetically favorable in both cases and show similar band structures with their (pseudo-)parabolic bands associated with alkali metals. Differences appear for the dispersion of the bands as well as the quantitative value of the band gaps, which are both higher for the Na-Sb compounds. With this we have gained valuable insights into the fundamental properties of many different crystals, including possible metastable and polycrystalline phases that can form during the experimental growth process. Our high-throughput approach therefore allows us to characterize complex materials and is a first step towards understanding their properties, without going beyond DFT at this point.

4 Optical Properties of Alkali Antimonides

After the general overview of the properties of alkali antimonide crystals at various stoichiometries in the previous chapter, we are now going to take a more in-depth look at the electronic and optical properties of eight binary crystals from the previous high-throughput study. Here, we focus on stable crystals at the important 3:1 and 1:1 alkali:antimony ratios and go beyond DFT by adding calculations with many-body perturbation theory. The selected representative crystals are all semiconducting and are shown in Fig. 11.

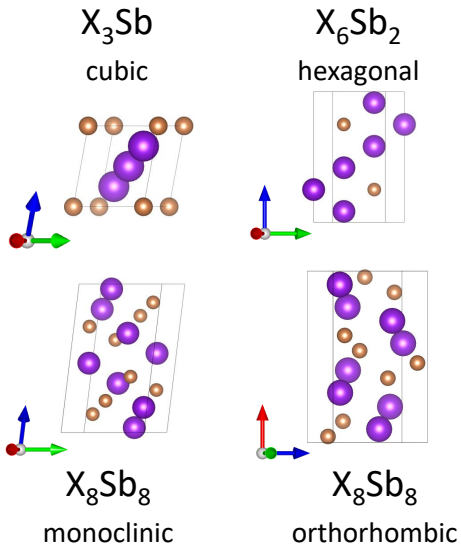

Figure 11: Unit cells of the crystals analyzed in this chapter. The alkali species X = {Na, K} are depicted in purple and Sb in bronze.

The structures at 3:1 stoichiometry correspond to the semiconducting cubic and hexagonal phases analyzed already in the previous chapter. For the 1:1 ratio, the monoclinic phase is supplemented with an orthorhombic crystal structure. In all cases, we analyze the same structures for both K-Sb and Na-Sb in order to make a direct comparison. A comparison of the properties associated with different lattice symmetries is necessary because the different symmetries of the structures in Fig. 11 have indeed been shown to appear experimentally for the class of alkali antimonides and are particularly relevant when going to heavier alkali metals, especially cesium. In the early experimental studies of Spicer, hexagonal phases appeared for K_3Sb and Na_3Sb, while Cs_3Sb samples were cubic [31]. For the 1:1 phases, KSb and NaSb favor a monoclinic symmetry, as seen also in the high-throughput study in the previous chapter, while an orthorhombic symmetry is typical for CsSb. However, this separation is not strict and it has been shown that monoclinic and orthorhombic phases can in fact coexist for CsSb [114].

4.1 Electronic Properties from MBPT

As the first step of the analysis with MBPT, we are going to take another look at the electronic structure of the considered compounds. In order to obtain quantitatively more accurate results, we are going to perform another round of band structure calculations, this time with the G_0W_0 method. To build on the analysis in the previous chapter and to show the concrete impact of the G_0W_0 correction, we are going to underlay the quasi-particle band structure with the original results from DFT, as seen in Fig. 12 for the 3:1 ratio.

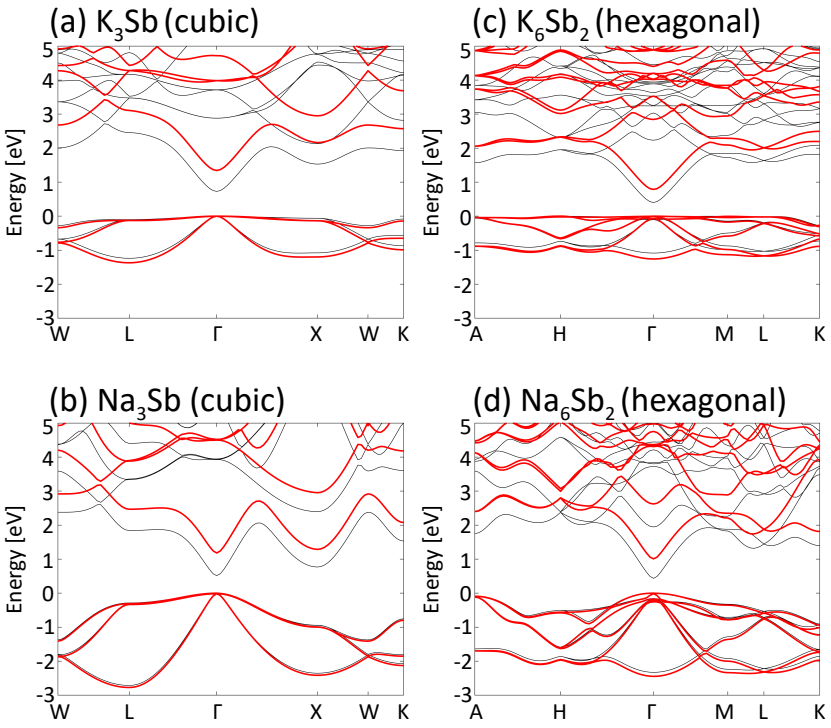

Figure 12: Band structures with the direct overlay of results from DFT (gray) and G_0W_0 (red) for crystals with 3:1 alkali:antimony ratio. All results are aligned with the valence band maximum set to 0 eV.

As visible in Fig. 12, the G_0W_0 correction leads to an opening of the band gap without significantly altering the overall slope or character of the bands. Due to the almost identical structures, the results are again very similar for the K-Sb and Na-Sb crystals. In our analysis, we want to focus on the differences that originate from the different alkali species and see how a light (Na) or heavy (K) alkali metal influences the QP band structure. This behavior can then be extrapolated on also other alkali antimonides such as cesium antimonide.

Taking now a more detailed look at the individual results, we start with the electronic structure of the cubic crystals in Fig. 12 (a) and (b). The quasiparticle correction increases the gap by about 0.6 eV for both K_3Sb and Na_3Sb, reaching 1.34 eV and 1.18 eV, respectively. The overall dispersion of the bands remains unaffected by the self-energy correction. However, there are minor differences in the detailed electronic structure at various high-symmetry points. In the valence band region, we see especially for K_3Sb how the QP band structure shows a slightly higher dispersion than that from DFT, broadening this band region by a few tens of meV. This effect is less visible for Na_3Sb with its already higher band dispersion from DFT. Also in the unoccupied region we can see that the shift from the self-energy correction is not completely rigid for the bands higher up in energy, we see that the difference between DFT and QP bands tends to increase with increasing distance from Γ. This picture is largely identical for the hexagonal crystals with the same stoichiometry, see Fig. 12 (c) and (d). Also here the self-energy correction opens the gap by around 0.6 eV. With the smaller DFT gap, this amounts to 0.79 eV for K_6Sb_2 and 1.01 eV for Na_6Sb_2. The overall band dispersion remains the same, but bands that are not directly at the VBM or CBm are slightly shifted with respect to each other.

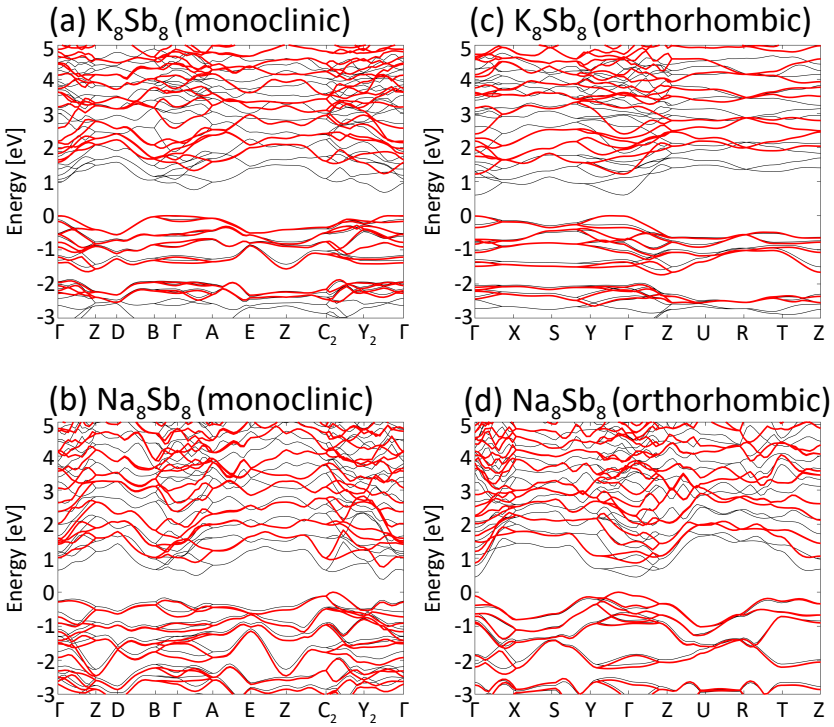

Figure 13: Band structures with the direct overlay of results from DFT (gray) and G_0W_0 (red) for crystals with 1:1 alkali:antimony ratio. All results are aligned with the valence band maximum set to 0 eV.

Moving on the the 1:1 stoichiometry, the monoclinic crystals from the previous chapter appear again in Fig. 13 (a) and (b) with their large number of bands, stemming from a total of 16 atoms in the unit cell of these crystals. The band structures calculated with the G_0W_0-method show gaps of 1.29 eV (K_8Sb_8) and 1.05 eV (Na_8Sb_8), which corresponds to an increase of around 0.6 - 0.7 eV compared to the DFT results. Due to the low value of the DFT gaps, this change is quite significant. Similar to the 3:1 crystals, the dispersion of the bands is slightly increased in the QP band structure. Finally, the electronic structure of the 'new' orthorhombic phases is presented in Fig. 13, panel (c) and (d). Both crystals show a direct band gap at Γ of 1.23 eV (K_8Sb_8) and 0.90 eV (Na_8Sb_8), which is around 0.1 eV lower than for the respective monoclinic phases. This minor, but notable, decrease is related to the higher band dispersion of the orthorhombic crystals, which is most evident for the highest occupied bands. As before, there is no qualitative difference between the DFT and G_0W_0 band structures.

In order to provide a better overview over the quantitative changes from the G_0W_0 correction, the numerical band gaps from both DFT and G_0W_0 are compiled in Table 1.

Table 1: Comparison of DFT (PBE-sol functional) and QP gap. All values in eV.

Stoichiometry	Symmetry	E_{gap}^{DFT}	E_{gap}^{QP}
K_3Sb	cubic	0.73	1.34
K_6Sb_2	hexagonal	0.40	0.79
K_8Sb_8	monoclinic	0.67	1.29
K_8Sb_8	orthorhombic	0.61	1.23
Na_3Sb	cubic	0.52	1.18
Na_6Sb_2	hexagonal	0.44	1.01
Na_8Sb_8	monoclinic	0.38	1.05
Na_8Sb_8	orthorhombic	0.45	0.90

While the self-energy correction leads to a significant opening of the gap on the magnitude of 0.4 to 0.7 eV, the QP gaps remain rather low, below the range of visible light. Among the chosen structures, the K-Sb crystals tend to have larger band gaps than the respective Na-Sb crystals, although the difference is not large and may also be coincidental. From the band structures we have seen that the gaps are direct for all compounds, with the exception of monoclinic Na_8Sb_8, where the smallest direct gap is about 220 meV higher than the smallest indirect gap. This is generally beneficial for optical transitions and therefore a high quantum efficiency.

4.2 Optical Properties from MBPT

In the next step, we are interested in the optical absorption of the considered crystals at different wavelengths, which we access by calculating the optical absorption spectra with the BSE. First, we will take a detailed look at the results for the 3:1 stoichiometry. The main parameters that we wish to understand are the influence of the alkali species as well as the difference between cubic and hexagonal crystal symmetry. To this end, we are going to make a direct comparison between the optical spectra for the four crystals in our study plotted in Fig. 14.

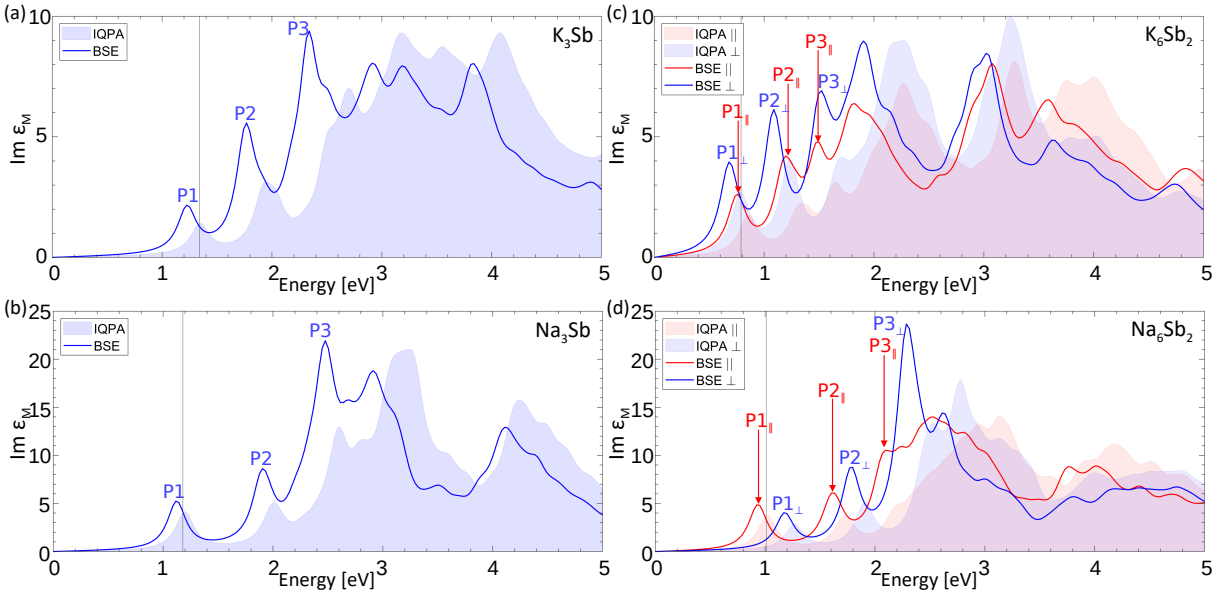

Figure 14: Optical spectra of the cubic crystals (a) K_3Sb and (b) Na_3Sb, as well as of the hexagonal crystals (c) K_6Sb_2 and (d) Na_6Sb_2. Plotted are results calculated from the full BSE (solid line) as well as in the IQPA (shaded area). In-plane ($\parallel$) and out-of-plane ($\perp$) components are plotted separately for the hexagonal crystals. In all cases, a Lorentzian broadening of 100 meV is applied. A vertical bar marks the QP gap and the first three peaks are indicates as P1 - P3.

For all crystals, we plot both the result from the full BSE as well as from the independent quasiparticle approximation (IQPA) in order to assess the difference between them, which corresponds to the influence of excitonic effects. For the hexagonal crystals, the independent in-plane ($\parallel$) and out-of-plane ($\perp$) components can be plotted separately. Additionally, the first three peaks are marked as P1, P2 and P3, respectively, and will be analyzed further.

Starting with the cubic crystals in Fig. 14(a) and (b), we can see an absorption onset

in the near-infrared region, as expected from the low quasiparticle gap in their band structures. The first excitation (P1) is located at 1.23 eV for K_3Sb and 1.11 eV for Na_3Sb. The second peak (P2) appears around 0.5 eV higher in energy for both materials. It is significantly larger, especially for K_3Sb, where it has about three times the oscillator strength of P1. Then at around 2.3 eV we find the third and most intense peak P3. After P3, the spectrum enters a continuum. For K_3Sb, this continuum of excitations remains nearly as intense as P3, while for Na_3Sb we see a significant drop in oscillator strength between 3.2 and 4.0 eV.

By comparing the spectrum calculated with the full BSE with that from the IQPA, we can assess the effect of electron-hole correlations. Most obvious is that the inclusion of the electron-hole correlation shifts the entire spectrum to lower energies due to the electron-hole Coulomb attraction, which is significantly larger than the repulsion from the exchange interaction. This shift in energy between BSE and IQPA can be interpreted as the excitonic binding energy. It varies between the different parts of the spectrum, as the influence of excitonic effects is individual to each excitation. From the plotted spectra it is evident that there is overall a larger shift in energy due to excitonic effects for K_3Sb than for Na_3Sb. Quantitatively, the exciton binding energy of the first three peaks for K_3Sb is 0.12 eV for P1, 0.19 eV for P2 and 0.19 eV for P3. For Na_3Sb the values are 0.07 eV for P1, 0.11 eV for P2 and 0.13 eV for P3. At higher energies, also the qualitative shape of the spectrum changes with the inclusion of many-body effects.

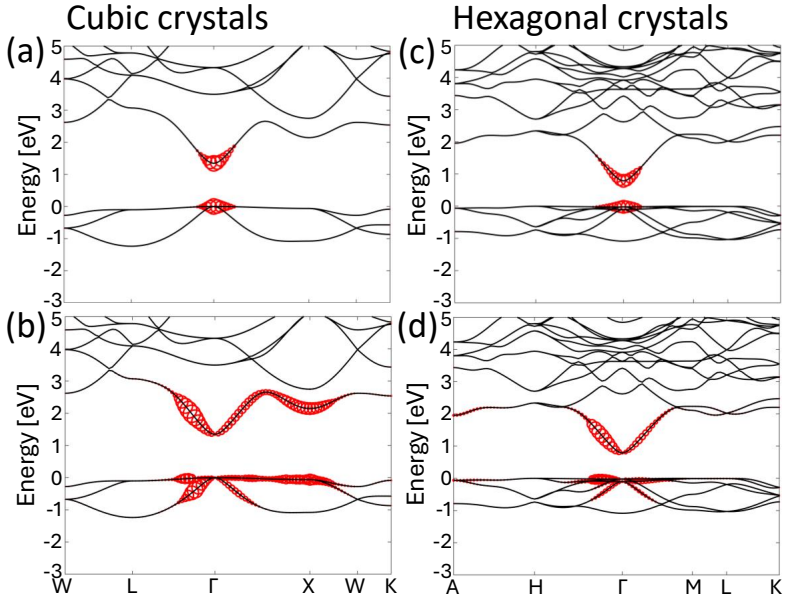

Figure 15: Excitonic weights projected on the band structure of the peaks (a) P1 and (b) P3 of K_3Sb, as well as of (c) P1($\perp$) and (d) P3($\parallel$) of K_6Sb_2.

To further understand the character of the features in the optical spectrum, we take a detailed look at the excitons in the marked peaks. For this purpose, we plot the excitonic weights projected on the band structure in Fig. 15. They show visually where the exciton is located in k-space.

In this case, the character of P1 and P2 is almost identical and plotted in Fig. 15(a). It shows a direct transition at Γ from VBM to CBm, which corresponds to an excitation from an Sb p-orbital to an s-orbital of the respective alkali species. This implies that the excitation leads to a delocalized Wannier exciton in real space, while in k-space the exciton is strongly localized. This characterization is the same for both K_3Sb and Na_3Sb. Due to the strong dispersion of the parabolic CBm, this transition can give rise to multiple peaks at different energies, namely P1 and P2 with approximately 0.5 eV difference in between.

The third peak P3, on the other hand, has a different excitonic character, as shown in Fig. 15(b). It consists of various transitions spread out over a large part of the Brillouin Zone, mainly around the high-symmetry points Γ and X and the path in between. Multiple occupied bands but only the lowest unoccupied band contribute. The large number of different transitions is in line with the large oscillator strength of P3. Contrary to P1 / P2, we expect this exciton to be more localized in real space.

We now compare the findings above with these of the related hexagonal crystals with chemical formula K_6Sb_2 and Na_6Sb_2. As anticipated, the lower symmetry group leads to two distinct optical components, in-plane ($\parallel$) and out-of-plane ($\perp$). They are plotted in red and blue in Fig. 15(c) and (d). Corresponding to the lower quasi-particle gap compared to their cubic counterparts, the hexagonal crystals have a lower optical absorption onset, 0.68 eV for K_6Sb_2 and 0.92 eV for Na_6Sb_2. Notably, the component in which the very first peak appears is different between these two materials, for K_6Sb_2 it is the out-of-plane component ($P1_\perp$) and for Na_6Sb_2 the in-plane component ($P1_\parallel$). Another interesting difference between the two spectra is the energy separation between the peaks from the in-plane and out-of-plane component. It is visibly much larger for Na_6Sb_2 than for K_6Sb_2. For example, the first peak shows a separation of 70 meV between $P1_\perp$ and $P1_\parallel$ for K_6Sb_2, while it is 260 meV for Na_6Sb_2. Also qualitatively, there is a significant difference. In the case of K_6Sb_2, the two distinct spectra have an almost identical slope, with differences only in the magnitude and exact location of the peaks. For Na_6Sb_2, on the other hand, there are fundamental differences between the two plotted spectra at energies above 2 eV.

Again, the difference between the spectra from the full BSE and in the IQPA yields the exciton binding energy. Similar to the cubic structures, the binding energy is slightly higher for the K-based crystal than for the Na-based crystal. For example, for K_6Sb_2 the first peak is shifted by about 110 meV in energy in both $P1_\perp$ and $P1_\parallel$, while the corresponding shift for Na_6Sb_2 is only 90 meV. For the further peaks the difference in energy due to excitonic effects is similar, about 140 meV for $P2_\perp$ and $P2_\parallel$ and 190 meV for $P3_\perp$ and $P3_\parallel$. In the case of Na_6Sb_2, the inclusion of electron-hole effects also significantly changes the oscillator strength, especially in the region between 2 and 3 eV.

As before, we turn to the excitonic weights to better understand the character of the peaks. They are plotted in Fig. 15(c) and (d) for the hexagonal crystals. As visible in the figure, the excitonic weights of the hexagonal crystals are extremely similar to that of the cubic ones. The first two peaks (Fig. 15(c)) correspond to a direct transition between VBM and CBm at Γ. This describes again a transition from an Sb p-orbital to an alkali s-orbital which is highly localized in k-space, delocalized in real space and can occur with different energies due to the high dispersion of the parabolic CBm. This characterization is independent of the polarization of the incoming light. The third peak (Fig. 15(d)), on the other hand, corresponds to excitons that are broadly delocalized in k-space and localized in real space.

After understanding the character of the optical spectra for the relatively simple materials with 3:1 alakli:antimony ratio, we now turn to the crystals with the equal 1:1 ratio. Due to the lower symmetry group of the monoclinic and orthorhombic structures analyzed here, there are three distinct optical components corresponding to the on-diagonal elements of the dielectric tensor. The monoclinic crystals show additional non-zero off-diagonal components. As the independent elements are not targeted individually in practice, we average over the on-diagonal elements in order to simplify the analysis. The averaged optical spectra are then plotted in Fig. 16.

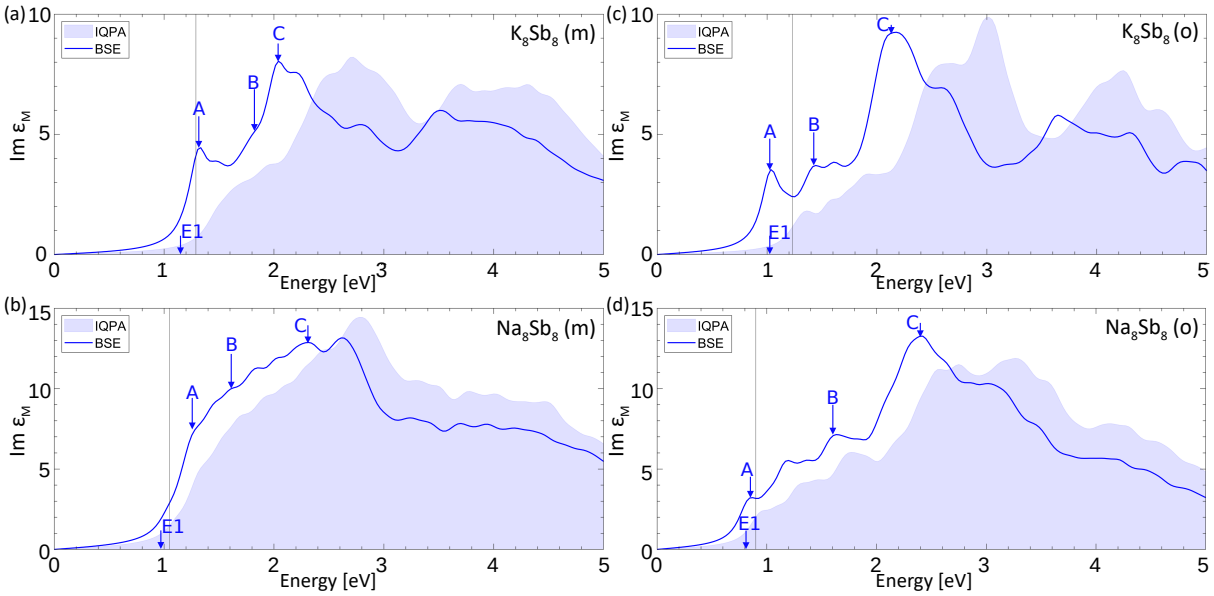

Figure 16: Optical spectra of monoclinic (a) K_8Sb_8 and (b) Na_8Sb_8, as well as of orthorhombic (c) K_8Sb_8 and (d) Na_8Sb_8. Plotted are results calculated from the full BSE (solid line) as well as in the IQPA (shaded area). In all cases, the plotted results are the average of all on-diagonal components of the macroscopic dielectric tensor and a Lorentzian broadening of 100 meV is applied. A vertical bar marks the QP gap. Exemplary peaks are indicated as A, B & C for further analysis and the very first excitation is labeled as E1.

Due to the large number of bands and the high density of states close to the gap, as seen in the electronic structure, the optical spectra in Fig. 16 show a large number of excitations close together in energy. This leads to spectra that are rather broad and have peaks that are less clearly defined compared to the crystals with 3:1 ratio. For this reason, we mark interesting peaks with letters in this plot, as they do not correspond to peak 1 - 3. However, the optical absorption onset is again at around 1 eV for all compounds, corresponding to the similarly low band gap.

We now take a more detailed look at the individual spectra, starting with monoclinic K_8Sb_8 in Fig. 16(a). At lower energies, there are two clearly distinct peaks, A at 1.33 eV and C at 2.0 eV. Between them are many smaller excitations that are not individually visible. One of them is marked as B at 1.82 eV. We also mark the lowest energy excitation as E1, but it does not show any significant oscillator strength associated with it. This is likely due to the fact that VBM and CBm have a similar character, stemming both from Sb p-orbitals. Again, we compare the result from the BSE to that in the IQPA. As it is difficult to clearly define individual peaks in these spectra, we cannot clearly quantify the exciton binding energy as difference between the energy in the BSE and the IQPA

here. However, we can see qualitatively that the major peaks A and C are significantly redshifted by the inclusion of excitonic effects. They also appear sharper and more narrow in the BSE spectrum compared to the results in the independent particle picture.

In this case we do see a major difference between the results for the K-based and Na-based alkali antimonides. The spectrum of monoclinic Na_8Sb_8 plotted in Fig. 16(b) barely shows any individual peaks at all. Furthermore, the inclusion of excitonic effects leads to a smaller shift in energy compared to K_8Sb_8, amounting to only a few tens of meV. The lowest-energy excitation E1 is again very weak and located at 0.98 eV. Features are marked at 1.28 eV (A), 1.63 eV (B), and 2.31 eV (C).

For the orthorhombic crystals we find a picture similar to that of the monoclinic structures. The optical spectrum of orthorhombic K_8Sb_8 shown in Fig. 16(c) is characterized by an initial peak A at 1.03 eV followed by numerous minor excitations and then the global maximum C at 2.15 eV, as also seen for the monoclinic lattice with the same stoichiometry. The intermediate feature B is marked at 1.44 eV. In this case the absorption onset and lowest energy excitation E1 coincides with A. Again, there is a significant redshift of the spectrum from including excitonic effects. Also qualitatively, the oscillator strength gets redistributed by including electron-hole correlations compared to the independent particle spectrum. This is particularly evident at peak C and its neighboring shoulder.

Contrary to monoclinic Na_8Sb_8, the spectrum of orthorhombic Na_8Sb_8 in panel (d) shows numerous distinct peaks, even though it remains overall rather broad. The first peak (A) is located at 0.84 eV, close to the very first (dark) excitation E1 at 0.81 eV. Another peak is centered at 1.63 eV (B) and we find the global maximum of the spectrum at 2.43 eV (C). Similar to monoclinic Na_8Sb_8, the difference between BSE and IQPA spectra is rather small, with only minor qualitative differences and a small shift towards lower energies.

Again, we plot the excitonic weights to better understand the character of the peaks. Due to the large number of excitations in these spectra, we plot only a few exemplary cases in Fig. 17.

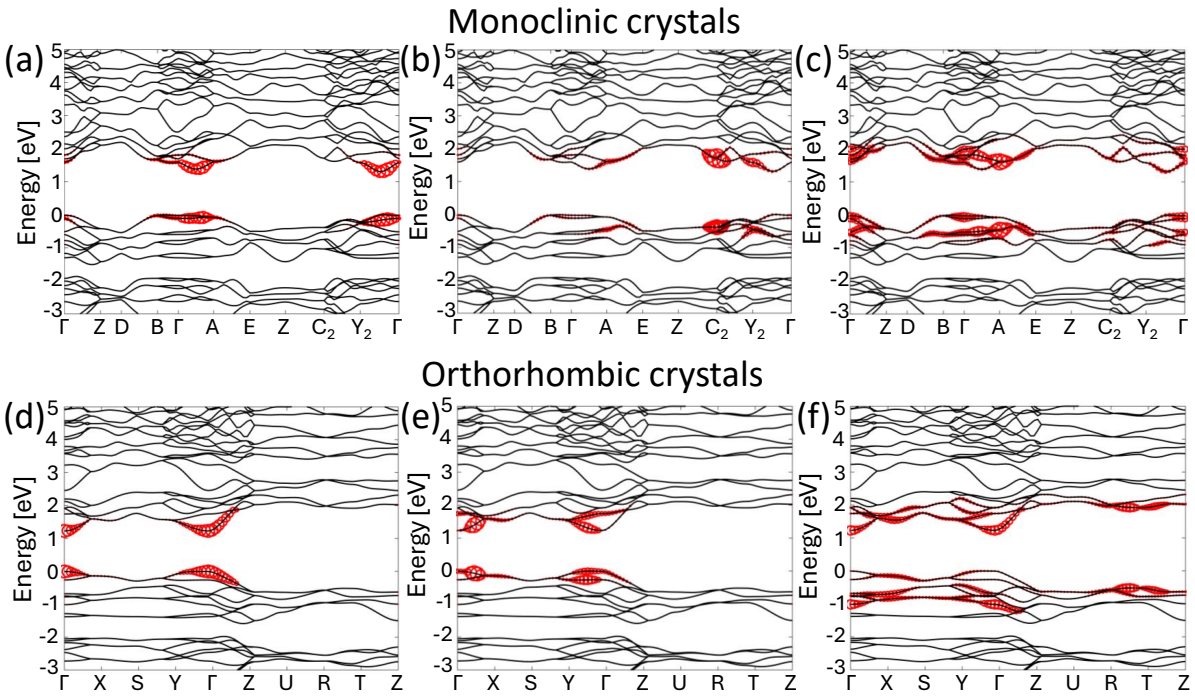

Figure 17: Excitonic weights projected on the band structure for exemplary excitons in the peaks A (a), B (b), and C (c) of monoclinic K_8Sb_8, as well as in A (d), B (e), and C (f) of orthorhombic K_8Sb_8.

In the upper part of Fig. 17, we show exemplary excitonic weights associated with the peaks A, B and C of the monoclinic crystals (panel (a) - (c)), while the plots in the lower half are associated with the peaks A, B and C of the orthorhombic crystals (panel (d) - (f)). The plots in the figure are for the K_8Sb_8 compounds, but the qualitative picture is similar for the Na_8Sb_8 crystals because of their similar electronic structure.

The electronic structure of these materials with its multitude of bands gives rise to a similarly complex distribution of the excitonic weights. The first exciton shown in Fig. 17 (a) (peak A) is located close to the VBM and the CBm and already slightly spread out in the Brillouin Zone. It is about 100 meV higher in energy than the direct VBM to CBm transition, which would correspond to the very first excitation E1. The excitations higher up in energy get progressively more spread out over the Brillouin Zone and include multiple bands. In panel (b) there is an exciton with transitions from multiple occupied bands targeting the lowest unoccupied band, while in panel (c) an exciton with transitions from a total of four occupied bands to the lowest four unoccupied bands is shown.

The excitons plotted for the orthorhombic structures similarly get more complex for higher energies. One major difference is that peak A with the excitonic weights shown in Fig. 17

(d) originates from the direct VBM to CBm transition and is equivalent to the lowest energy excitation E1. Peak B (Fig. 17 (e)) consists of transitions from the two highest occupied bands to the two lowest unoccupied bands and is located close to but not exactly at Γ in the Brillouin Zone. Peak C (Fig. 17 (f)), on the other hand, is spread out through most of the Brillouin Zone and has contributions from multiple occupied and unoccupied bands.

In summary, in this chapter we have investigated the fundamental properties of eight binary K-Sb and Na-Sb crystals with many-body perturbation theory, focusing on the 3:1 and 1:1 alkali:antimony ratio. From the QP band structures, we have understood the electronic properties of these materials and in particular found direct band gaps between 0.8 and 1.3 eV for all crystals save monoclinic Na_8Sb_8. Qualitatively, the electronic QP structure is the same as the DFT band structure, with rather flat bands on the top of the valence region and the characteristic parabolic shape of the bands at the bottom of the conduction region. Band dispersion is slightly increased in the G_0W_0 band structure, which is particularly visible for the K-Sb crystals with their low dispersion in the DFT band structure. Corresponding to the small band gaps, the calculated spectra show optical absorption onsets in the near infrared region, which is beneficial for the use with lasers of corresponding low energy. The optical spectra are qualitatively similar for compounds with the same stoichiometry but different crystal symmetry, which originates from the similarity in the electronic structure. The character of the peaks in the optical spectra is revealed by their excitonic weights which we can project on the band structure. An interesting fact seen from this analysis is how similar transitions in the electronic structure, e. g. the VBM to CBm transition for the cubic and hexagonal crystals, can give rise to multiple distinct peaks at clearly different energies in the optical spectrum. An overall trend we found is that excitonic effects have a significantly larger impact for the K-Sb materials compared to the Na-Sb crystals. The redshift in energy is larger for the former, exceeding a binding energy of 100 meV for the single excitons, and also the qualitative differences between BSE and IQPA spectra are larger. This behavior can be rationalized through the electronic structure. For the Na-Sb compounds with their strongly dispersive bands especially in the upper valence region, the excitons tend to be more localized in k-space compared to the K-Sb crystals. In real space, they are more delocalized, which can also be related again to the lighter Na atoms. Therefore, they are rather loosely bond and show limited excitonic effects and binding energies. For K-Sb on the other hand, the flat valence bands lead to a higher delocalization in k-space while the electron-hole pairs are closer together in real space. This leads to a tighter binding with higher exciton binding energies and excitonic effects.

5 Implementation of the Three-Step-Model from MBPT

In the previous two chapters, we have calculated and analyzed the fundamental properties of various alakli-antimonides, going beyond the intrinsic limitations of standard DFT by including quasiparticle and excitonic effects via the *GW* approximation and the Bethe-Salpeter equation. However, our calculations provide us only with the microscopic properties of these materials. To efficiently advance the development of photocathodes as electron sources, we need to make a connection to the macroscopic observables that can be measured in the experiment for real-life photocathodes. To this end, we develop and present a parameter-free scheme to use the results of many-body perturbation theory in the framework of the three-step model for photoemission to predict the macroscopic quantum efficiency of semiconducting materials.

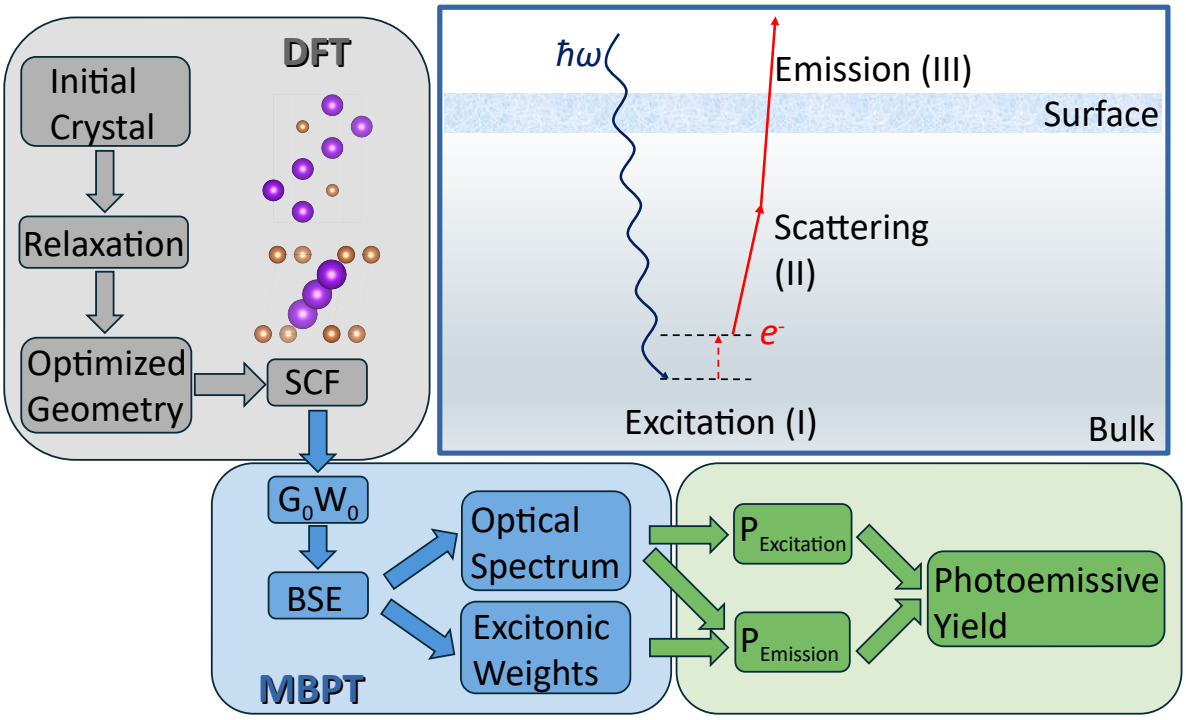

Figure 18: Schematic overview of the computational steps in our implementation of the three-step model. Through colored blocks, we divide the scheme between DFT calculations of the ground-state properties (gray), MBPT runs (G_0W_0+BSE) to access excited state properties (blue), and final post-processing to compute the photoemission yield (green). A sketch of the three steps of photoemission is included as an inset.

5.1 Model Creation

As previously discussed, the three-step model seeks to describe the photoemission process through the three steps of Excitation (I), Scattering (II) and Emission (III). Our implementation of this model is realized through a set of post-processing routines for the results from DFT and many-body perturbation theory. A visualization of the sequence of calculations is shown in Fig. 18.

The first part, placed in the gray box, is a series of DFT calculations to relax the initial crystal structure and then run a final high-level DFT calculation to compute the ground-state properties of the crystal. This corresponds to what was done in our high-throughput study for a large number of crystals in Chap. 3. On top of these results, excited state properties are calculated with G_0W_0 and BSE. Relevant for our model are the optical properties, which are the optical spectrum and the excitonic weights of the single peaks in it. These steps, shown in the blue box, correspond to the calculations presented in Chap. 4 for binary crystals. Finally, the green box is the post-processing part, which will be developed and presented in this chapter. By calculating probabilities of successfully 'passing' every step of the photoemission process, we seek to obtain ultimately the photoemissive yield / quantum efficiency.

We will illustrate this at the example of hexagonal K_3Sb, which was discussed in the previous chapter.

Step 1: Photoexcitation The first necessary quantity is the probability of photoexciation, $P_{\text{Excitation}}(\omega)$. It is defined as the probability that an incoming photon with energy $\hbar\omega$ leads to an optical excitation in the crystal and creates an excited electron in the conduction band. In other words, $P_{\text{Excitation}}(\omega)$ is the ratio between incoming photons and excited electrons created in the crystal, irrespective of whether they are emitted or not.

The imaginary part of the macroscopic dielectric function obtained from the BSE is known (Eq. 24) as

$$\Im\epsilon_M = \frac{4\pi^2}{\pi\Gamma\Omega}\sum_\lambda |\mathbf{t}_\lambda|^2 \left(\frac{\Gamma^2}{(\omega - E_\lambda)^2 + \Gamma^2} - \frac{\Gamma^2}{(\omega + E_\lambda)^2 + \Gamma^2}\right), \tag{26}$$

featuring excitations and deexcitations with the Lorentzian broadening Γ. E_λ and $\mathbf{t}_\lambda$ are energies and transition coefficients of the single excitons, and Ω is the volume of the unit cell. The quantity $\Im\epsilon_M$ describes the probability of excitation and is therefore directly proportional to the required $P_{\text{Excitation}}$. It is possible to obtain a qualitatively accurate result for $P_{\text{Excitation}}$ by directly using $\Im\epsilon_M$ for it and normalizing the global maximum to 1.

How to quantitatively predict $P_{\text{Excitation}}$ without the need for normalization will be discussed later.

As we have seen in the previous chapter, $\Im\epsilon_M$ is a tensor and can have multiple distinct components. Similar to what was previously shown for the monoclinic and orthorhombic crystals, we will average over the different on-diagonal components, as they will usually not be individually targeted in the experiment. Off-diagonal contributions are assumed to be negligible. With this, we mathematically define the excitation probability as

$$P_{\text{Excitation}}(\omega) = \frac{\Im\epsilon_M^{\text{avg}}(\omega)}{\max_\omega[\Im\epsilon_M^{\text{avg}}(\omega)]}. \tag{27}$$

This quantity is shown for hexagonal K_3Sb in Fig. 19.

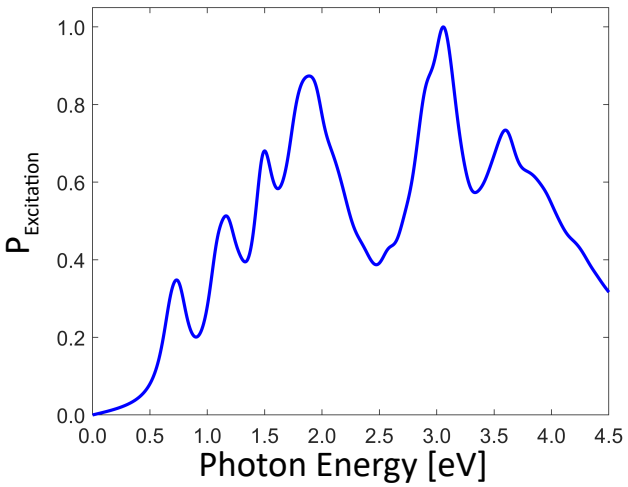

Figure 19: Optical absorption averaged over all on-diagonal components for hexagonal K_3Sb and normalized to 1 at the maximum in the shown energy range.

In the plot in Fig. 19 there are multiple clearly defined peaks, with the first one being at around 0.7 eV. As seen in Chap. 4, the initial two peaks are made up of transition from the VBM to the CBm, while excitations higher up in energy include further bands. However, in this chapter we are interested in the absorption at higher energies, starting from about 2.5 - 3.0 eV, as the excited electrons from excitations at lower energies will not be able to overcome the work function and be emitted. Therefore, the most important features we note here are the peaks at 3.1 and 3.7 eV, as well as the qualitative fact that the optical absorption decreases for photon energies above 4.0 eV.

Step 2: Electron Transport and Scattering The second step of the three-step model is the transport of the excited electrons to the surface, during which scattering events can occur. However, as our model is created for semiconductors, electron-electron scattering is negligible (contrary to metals). The relevant scattering mechanism that remains is electron-phonon scattering, which leads to only small band renormalizations ($\approx$ 100 meV) [115]. In order to focus on the effects that have a larger quantitative impact and to keep computational costs manageable, we do not explicitly include scattering and assume that all scattering events are fully elastic. With this approximation we expect that our model overestimates the final QE, as we ignore possible electron loses during transport. However, this effect is expected to be small, especially if the described photocathodes are thin-films where the distance from the bulk to the surface remains on the order of nanometers.

If a complete quantitative description of the transport process was to be wanted, this could be accomplished via Monte-Carlo simulations [115, 116, 117] at significantly increased cost and effort. Alternatively, available values from the literature for the mean free path or the attenuation length can be used to estimate how significant or insignificant scattering events are.

Step 3: Emission Probability The final step describes the electron overcoming the surface and being emitted into the vacuum. The probability for this is $P_{\text{Emission}}(\omega)$, which is the fraction of excited electrons leaving the photocathode. This quantity still carries a dependence on the energy of the incoming photon $\hbar\omega$, as the needed information is the likelihood that an excited electron created by a photon of this energy gets emitted.

In a simple approximation, ignoring complex effects like surface roughness and surface defects, we can treat overcoming the surface as overcoming a potential barrier. If we

assume a step function as idealized potential, the transmission probability is

$$T(E) = \begin{cases} \frac{4\sqrt{E(E-V_0)}}{(\sqrt{E}+\sqrt{E-V_0})^2} & \text{for } E \geq V_0 \\ \\ 0 & \text{for } E < V_0, \end{cases} \tag{28}$$

with E being the energy of the electron and V_0 the vacuum potential. In this work, we will match V_0 to the experimental value available through the work function from the measured data. This allows a direct comparison with the experimental spectra. For a full *ab initio* appraoch, it is also possible to compute V_0 with a surface slab calculation [4].

To illustrate the character of the transmission function $T(E)$, we plot it for hexagonal K_3Sb in Fig. 20. In this plot, the vacuum potential $V_0 = 2.9$ eV is matched to the experimental onset [31]. We can clearly see the steep onset at V_0 and the asymptotic increase towards a probability of 1 at higher energies.

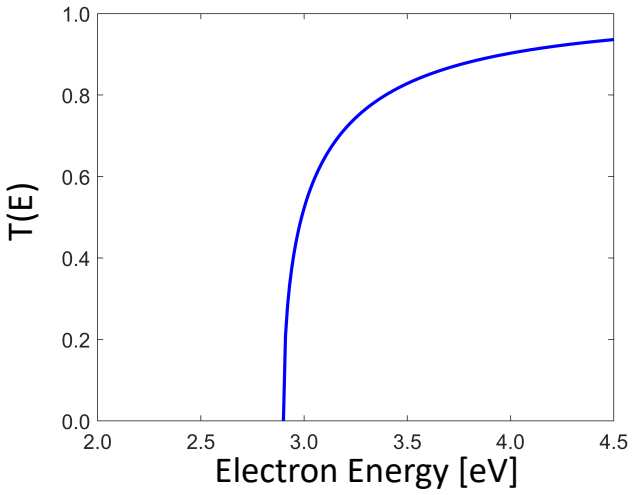

Figure 20: Probability of emission depending on the energy of an excited electron for a potential step of 2.9 eV.

With the function $T(E)$, a description of the emission probability depending on the electron energy E is available. In the next step, it is necessary to connect this probability to the photon energy $\hbar\omega$. To this end, we define the energy distribution function $D_\lambda(E)$ of the excited electron generated from the excitation with index λ. It describes the probability of finding the electron generated by excitation number λ at the energy E. This information is taken from the excitonic weights resulting from the BSE. It can be extracted

by summing over all the $\vec{k}$-resolved electron weights which target unoccupied bands:

$$D_\lambda(E) = \sum_{c=n_{\mathrm{CBm}}}^{n_{\mathrm{CBmax}}} \sum_{\vec{k}} w^\lambda_{c\vec{k}}\, \delta(E - \varepsilon^{QP}_{c\vec{k}}). \tag{29}$$

This sum runs from the lowest conduction band to the highest band included in the BSE. Practically, we use DFT energies shifted with a scissor operator that corresponds to the QP-correction to the fundamental gap in our workflow. The computational implementation of the calculation of the energy distribution is outlined in the appendix, part B.

An exemplary distribution $D_\lambda(E)$ is shown in Fig. 21. It belongs to an excitation at 3.6 eV in hexagonal K_3Sb and shows that the energy of this exciton is spread out mainly between 2.9 and 3.4 eV. We can see the discrete, δ-function character of the distribution.

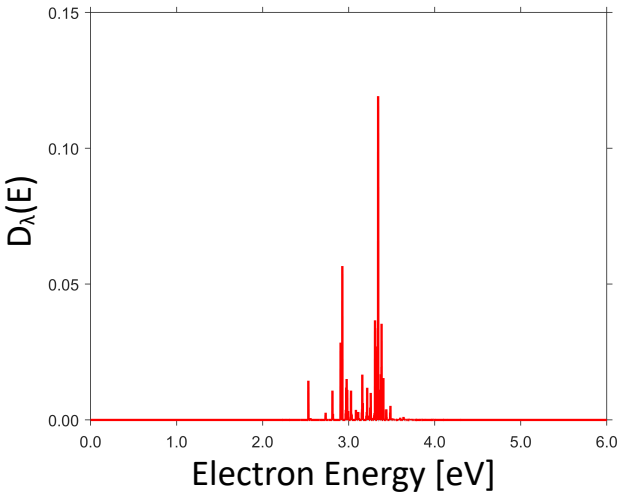

Figure 21: Exemplary energy distribution of an excited electron at 3.6 eV.

As the energy distribution $D_\lambda(E)$ for every possible excited electron with index λ is now available, the transmission probability $T(E)$ can be used to assign an absolute probability of emission $P^\lambda_{\mathrm{Emission}}$ to every single excitation:

$$P^\lambda_{\mathrm{Emission}} = \int_{E_{\mathrm{CBm}}}^{E_{\mathrm{max}}} T(E) D_\lambda(E) dE. \tag{30}$$

The integration boundaries in Eq. 30 correspond to the energy range associated with the unoccupied bands included in the BSE.

To proceed from this quantity to the overall emission probability $P_{\text{Emission}}(\omega)$ depending on ω, it is necessary to determine the contribution of the λ-th exciton to the full optical spectrum.

If the full spectrum is given by $\mathcal{S}(\omega) \equiv \Im\epsilon_M(\omega)$ as defined in Eq. 26, then the contribution of a single excitation is given by

$$\mathcal{S}_\lambda(\omega) = \frac{4\pi^2}{\pi\Gamma\Omega}|\mathbf{t}_\lambda|^2 \left(\frac{\Gamma^2}{(\omega - E_\lambda)^2 + \Gamma^2} - \frac{\Gamma^2}{(\omega + E_\lambda)^2 + \Gamma^2} \right). \tag{31}$$

By definition $\mathcal{S}(\omega) = \sum_\lambda \mathcal{S}_\lambda(\omega)$. We now introduce $p_\lambda(\omega)$ as the probability of targeting the excitation with index λ if an optical excitation takes place at ω. It is given by the fraction of $\mathcal{S}(\omega)$ stemming from $\mathcal{S}_\lambda(\omega)$:

$$p_\lambda(\omega) = \frac{\mathcal{S}_\lambda(\omega)}{\mathcal{S}(\omega)}. \tag{32}$$

Summing over all possible excitations weighted by their contribution to the full optical spectrum then yields the overall emission probability:

$$P_{\text{Emission}}(\omega) = \sum_\lambda p_\lambda(\omega) P^\lambda_{\text{Emission}}. \tag{33}$$

This probability is the fraction of excited electrons that get emitted into the vacuum. In other words, it is the probability that an emitted electron is created if a photon has already been absorbed

Again, this quantity is plotted in Fig. 22 for the example of hexagonal K_3Sb. This plot shows, similar to the basic transmission probability for the potential barrier in Fig. 20, a sharp onset at 2.9 eV and then a nearly monotonic increase which eventually slows down for higher energies above 4.0 eV.

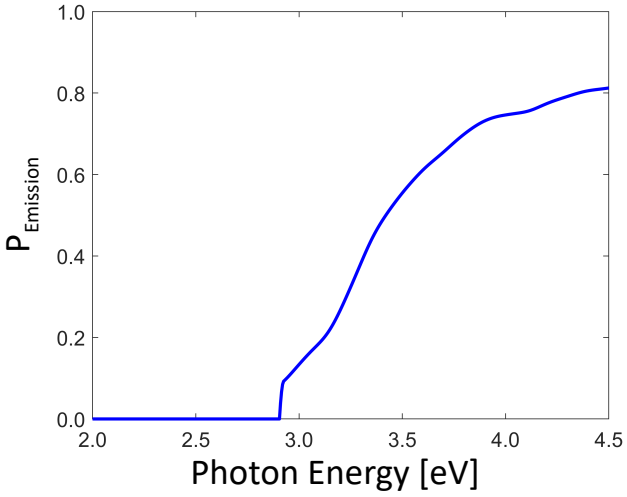

Figure 22: Calculated final emission probability by photon energy for hexagonal K_3Sb.

By putting together the ingredients collected so far, it is possible compute the final photoemissive yield (QE) as the convolution of excitation probability and emission probability:

$$P_{\text{Yield}}(\omega) = P_{\text{Excitation}}(\omega) \cdot P_{\text{Emission}}(\omega). \tag{34}$$

The final qualitative $P_{\text{Yield}}(\omega)$ in Eq. 34 is the optical spectrum from the BSE modulated by the probability that an electron excited by a photon with wavelength ω is in fact emitted through the surface.

At this point we are still at a qualitative description of the spectral response, as we have normalized $P_{\text{Excitation}}$ to 1 at its maximum. A quantitative method will be discussed later. First, we will test whether we can qualitatively match the experimentally measured QE with our model.

5.2 Model Validation - Binary Crystals

We will start by benchmarking the results from our model against experimental photoemission data for the binary alkali antimonides K_3Sb and Na_3Sb, both with a hexagonal lattice. At this point we make only a qualitative comparison and align the maximum of the predicted QE to that of the experiment. Results for these two crystals are shown in Fig. 23 together with experimental data taken from Spicer's original work from 1958 [31].

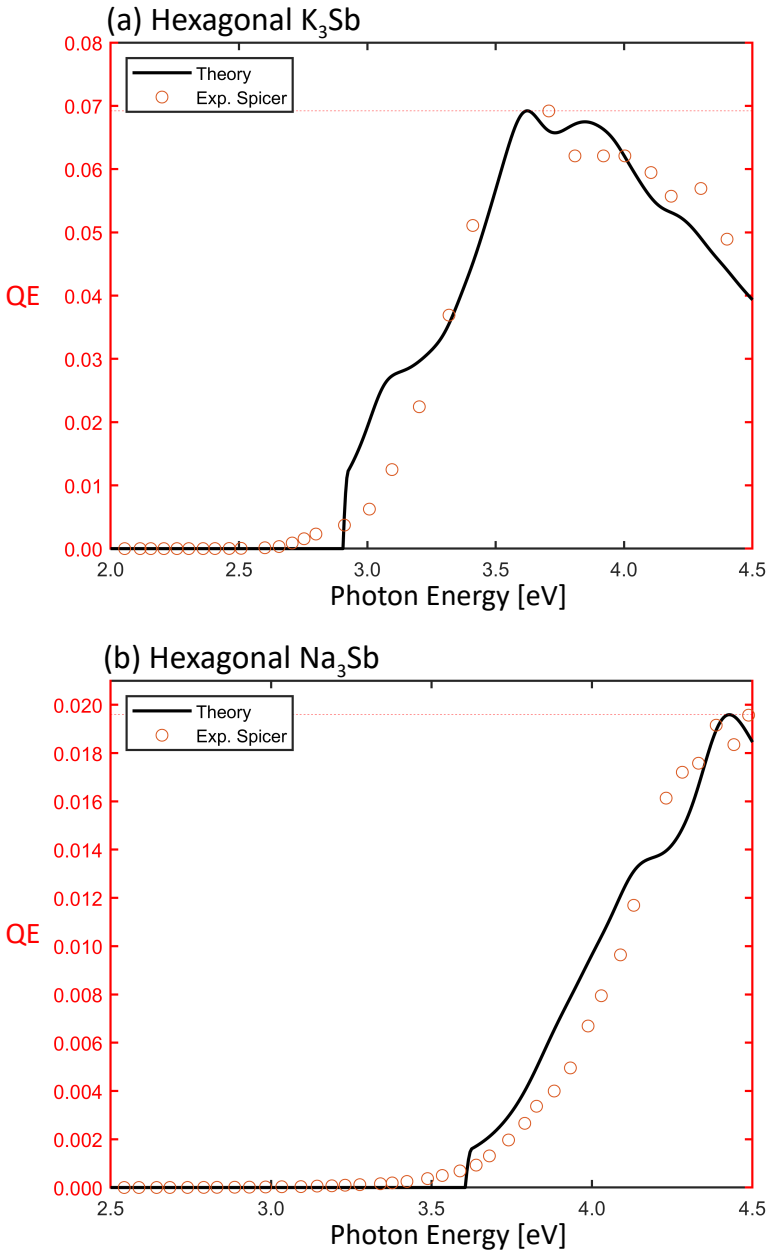

Figure 23: Results for binary crystals with K_3Sb and Na_3Sb composition, matched against experimental data from Spicer [31]. The absolute value of the predicted QE is aligned to the experimental data at the value indicated by the dotted bar. A Lorentzian broadening of 100 meV is applied to the theoretical results.

We start with K_3Sb in Fig. 23(a), which was already used to illustrate the development of the model in the previous section. As seen before, this material has an optical spectrum with multiple distinct peaks, in particular at 3.1 and 3.6 eV. In this plot, we see how the spectrum is modulated by the emission probability to generate the plot of the spectral response. There is a very steep initial increase at the onset of 2.9 eV, followed by a smoother increase up to the maximum QE of 0.07 aligned to the experimental data. Interestingly, the QE decreases again for higher energies above 4.0 eV. This is a result of the fact that the main peaks in the optical absorption spectrum are at lower energies. Comparing our theoretical prediction with the experimental dataset, we see a remarkable agreement. In particular the decrease at higher energies is captured extremely well. On the other hand, there is a notable difference between our theory and the experiment at the onset, where our prediction shows a much sharper increase than the experimental measurement. This can be attributed mainly to the description of the emission barrier as a step function. Another point influencing the onset is the fact that Spicer's samples were significantly influenced by impurities [31, 118], which leads to a strong smearing at and below the photoemission threshold. This effect does not appear in our calculations for an ideal bulk crystal. Still, the overall agreement for this example is quite good. An explicit treatment of possible impurities and surface defects could likely improve the agreement at the onset, but is not trivial to implement.

As second example we consider Na_3Sb with the spectral response plotted in Fig. 23(b). This material has a significantly lower peak QE of only 0.02 compared to K_3Sb. For both the experimental and the predicted data there is a similar monotonic increase from the threshold around 3.6 eV to the global maximum at about 4.4 eV. Similar to the previous example, the experimental QE at and below the onset is influenced by impurities [31, 118]. As no further features appear in the spectral response, the agreement between theory and experiment is good but does not reveal much about the performance of the model in more complicated cases.

5.3 Model Validation - Ternary Crystals

After showing a good agreement between our model and Spicer's measurements for K-Sb and Na-Sb binary crystals, we will now turn to the ternary materials that are used nowadays in state-of-the-art photocathodes [12, 13, 28]. In this case we will use measurements from Helmholtz-Zentrum Berlin (HZB) as benchmark.

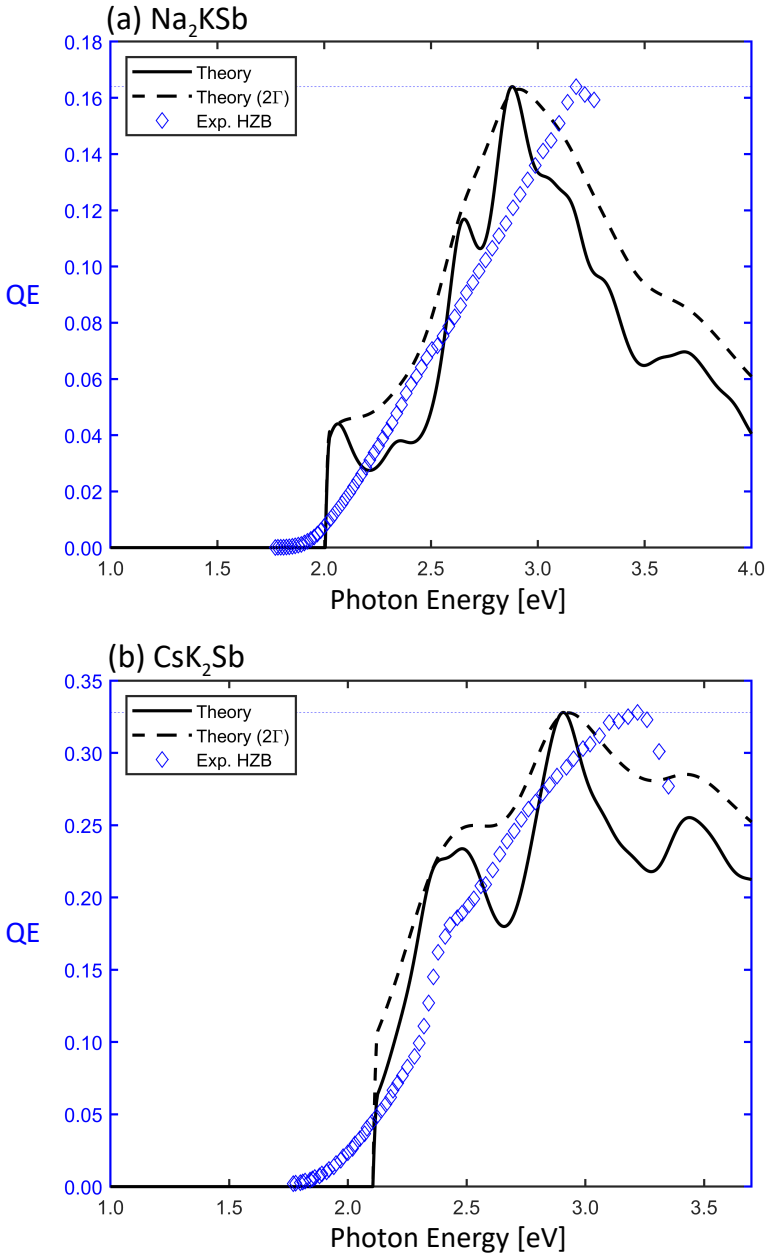

Figure 24: Results for ternary crystals with Na_2KSb and CsK_2Sb composition, matched against experimental data from HZB [1]. The absolute value of the predicted QE is aligned to the experimental data at the value indicated by the dotted bar. The theoretical results are provided with a Lorentzian broadening of 100 meV (solid line) as well as with a double broadening (2Γ) of 200 meV (dashed line).

The theoretical prediction and experimental data for Na_2KSb and CsK_2Sb are shown in Fig. 24. The spectral response of Na_2KSb in panel (a) starts at an onset of 2.0 eV. Above this threshold the experimentally measured QE rises steadily towards a maximum of more than 16% at 3.2 eV. There are very minor changes in the slope of the measured curve around 2.5 eV and 3.0 eV which hint at underlying effects that are not fully resolved in the experimental setup. The QE predicted from our model shows the same general trend but provides multiple smaller peaks and features not seen in the experiment. These peaks stem directly from the optical spectrum, while the calculated emission probability is constantly high for most energies in the visible spectrum due to the low vacuum potential of this material. While the experimental curve is much smoother, this is to be expected due to the resolution of the measurement, which cannot resolve all minor peaks. In order to make a more direct comparison, we provide an additional plot of the theoretical spectral response with twice the 'standard' broadening to better account for experimental effects like the band width of the light source. With this additional broadening, all spectral features are assimilated into a single monotonically increasing peak, matching well the character of the experimental measurement. We do notice, however, that the features are shifted by around 100 meV between measured and predicted spectral response. This shift appears to be systematic over all energies. A possible reason for this is the numeric inaccuracy of the GW / BSE calculations which is also on the order of 100 meV. Other explanations are effects in the experiment itself that are not captured by our calculation such as defects and polycrystallinity, or possibly the temperature of the sample. Apart from the shift in energy, we are in good agreement with the experiment. This example also demonstrates a major benefit of our theoretical work, as we can use the additional information contained in the better resolved theoretical curve as a way to understand the physical picture behind the spectral response.

As final example for the qualitative validation of the model in Fig. 24(b), we plot the spectral response of CsK_2Sb, one of the most popular multi-alkali antimonides used today [12, 13, 23]. This material possesses a very large experimentally measured QE of more than 30% at its maximum. In this case, clear features appear also in the experimental measurement. There is a significant change in slope between 2.4 and 2.5 eV where the increase in QE almost plateaus and we find that the global maximum at 3.2 eV is followed by a sudden strong drop in QE afterwards. The same features appear in the theoretical prediction. There also is a plateau after the initial increase, which is at almost the same energy range, shifted only by a few tens of meV. Afterwards, we find a minimum at 2.6 eV which is not resolved in the experiment and then the global maximum at 2.9 eV. Again, we see a drop in QE when going to photon energies beyond that maximum. Notably, in

this case also the plot with the increased broadening retains clear features like the plateau around 2.5 eV, corresponding to the slope of the experimental spectral response. With this, we can conclude that there is an excellent agreement between model and experiment for this crystal, with the only major difference being an energy shift for the absolute maximum between both datasets. This can again be attributed to the lower accuracy of the BSE at higher energies as there may be an influence of states higher up in the conduction band that are not included in the solution of the BSE. Because of this, the predictive accuracy is better in the energy region closer to the onset. Finally, the origin of the peaks in the spectral response can be traced back to the optical spectrum from the BSE where two peaks appear at 2.4 eV and 2.9 eV [119].

5.4 Quantitative Predictions for Cs_3Sb

In the previous section we have shown that our model can deliver results which are qualitatively in agreement with the experiment. This is an excellent first step as it shows the validity of the model and allows us to better resolve and understand the different features in the spectral response. As the next step, we will expand our approach to cover quantitative predictions of the QE. This is important in order to also make predictions for materials where there is no clear experimental reference.

For this we consider the spectral response of cubic Cs_3Sb, which is, and has been for several decades, one of the most popular alkali antimonides used in photocathodes [12, 13, 120].

The scheme to make a full quantitative prediction is straightforward, as it is merely necessary to replace the non-quantitative $P_{\text{Excitation}}$ that was normalized to 1 with a quantitatively accurate $\tilde{P}_{\text{Excitation}}$. To this end, we consider the electric field $\vec{E}$ and the magnetic field $\vec{H}$ in a film of finite thickness. They are described by Maxwell's equations [121]. In momentum space, the two relevant equations take the form

$$\vec{k} \times (\vec{k} \times \vec{E}) + \frac{\omega^2}{c^2} \epsilon(\omega) \vec{E} = 0 \tag{35}$$

and

$$\vec{H} = \frac{1}{\mu_0 c} \vec{k} \times \vec{E}. \tag{36}$$

The dielectric tensor $\epsilon(\omega)$ is available from the result of the BSE. We now consider an electric field that propagates in z-direction with the wavevector k_z with fixed components k_x and k_y. Eq. 35 represents an eigenvalue problem for the electric field, which has non-trivial solutions if its determinant is zero. The double cross product in Eq. 35 leads to a 4th degree polynominal (in k_z) in the determinant, therefore there are four possible roots k_z that fullfill this condition. We can now formulate the electric field as a sum of four terms:

$$\vec{E} = \sum_{\sigma=1}^{4} A_\sigma \vec{p}_\sigma e^{k_x x + k_y y + k_{z,\sigma} z - \omega t}. \tag{37}$$

The four terms can be understood as two polarization of the electric field for two directions of motion. Each is connected with an amplitude A_σ and a polarization vector $\vec{p}_\sigma$. As $\epsilon(\omega)$ is known, it is possible to calculate the polarizations $\vec{p}_\sigma$ as eigenvectors from Eq. 35. Eq. 36 then yields the magnetic field, which will also have four magnetic polarizations $\vec{q}_\sigma$. Finally, the amplitude of the fields in the material can be connected to the initial amplitude of the incoming field through the boundary conditions for the x and y components of $\vec{E}$ and $\vec{H}$ at the interface between vacuum and material. This approach can be expanded to multiple layers with different dielectric functions if needed. In that case, boundary conditions are applied at every interface between layers.

With the outlined approach, we can obtain a full quantitative description of the electric and magnetic fields in a finite film of any thickness. For a macroscopic description, we now wish to extract the Fresnel coefficients of the system. For this purpose, we can calculate the time-averaged Poynting vector as

$$\langle \vec{S}_\sigma \rangle = \frac{1}{2} |\vec{p_\sigma} \times \vec{q_\sigma}|. \tag{38}$$

After summing over σ, this leads to the transmittance, which is defined as

$$T = \frac{\langle |\vec{S}^{\text{substrate}}| \rangle}{\langle |\vec{S}^{\text{vacuum}}| \rangle}. \tag{39}$$

Furthermore, we can also calculate the reflectance. As mentioned, the different components for $\sigma = \{1, .., 4\}$ correspond to waves with two different directions. If $\sigma = \{1, 3\}$ correspond to fields propagating forwards into the substrate and $\sigma = \{2, 4\}$ correspond to fields propagating backwards, then the reflectance can be calculated as

$$R = |A_2^{\text{vacuum}}|^2 + |A_4^{\text{vacuum}}|^2, \tag{40}$$

assuming amplitudes that are normalized to a total of one.

A computational implementation of this framework was originally created by C. Vorwerk as the `Python` package `LayerOptics` [122]. In addition to the thickness of the film, the package allows us to specify the angle of incidence of the beam as well as the polaization of the light. It also allows us to rotate the dielectric tensor to match a specific surface orientations. In earlier works, the code was used to calculate changes in the absorbance for different crystal planes [123] as well as for different polarizations of the incoming light [124]. In this work, on the other hand, we are more interested in the absolute quantitative values for the absorption. For this purpose, `LayerOptics` was updated to support the newest version of `Python 3` and subsequently used to compute the Fresnel coefficients.

With the now accessible Fresnel coefficients, we define the new quantitative excitation probability as

$$\tilde{P}_{\text{Excitation}}(\omega) = 1 - (R(\omega) + T(\omega)), \tag{41}$$

with the calculated reflectance and transmittance $R(\omega)$ and $T(\omega)$, respectively.

From this we derive the quantitative QE as

$$\tilde{P}_{\text{Yield}}(\omega) = \tilde{P}_{\text{Excitation}}(\omega) \cdot P_{\text{Emission}}(\omega). \tag{42}$$

Going back to the concrete example of Cs_3Sb, we calculate $\tilde{P}_{\text{Yield}}(\omega)$ here for a film of 9 nm thickness, corresponding to a real ultra-thin sample grown at Cornell [30]. We assume a beam with normal incidence for this calculation. The resulting quantitative spectral response is plotted in Fig. 25 together with the qualitative prediction without `LayerOptics` for comparison. Additionally, a total of four experimental datasets are provided as benchmark.

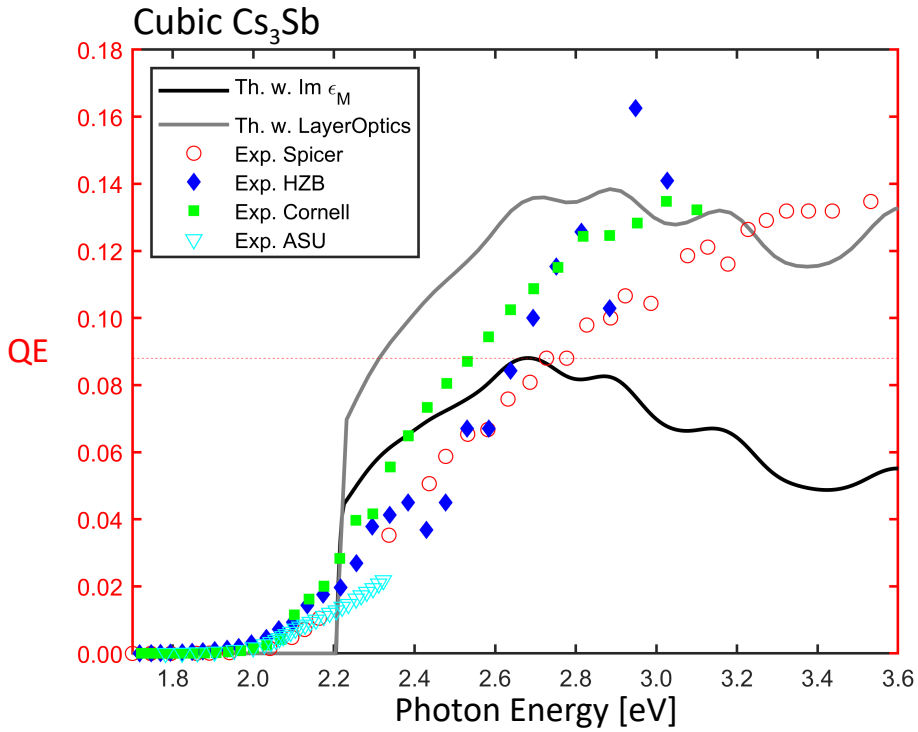

Figure 25: Results for cubic Cs_3Sb, compared against experimental data from Spicer [31] as well as measurements performed at HZB [125], Cornell University [30] and ASU [35]. The absolute value of the QE predicted with the non-quantitative model (Th. w. Im ϵ_M) is aligned to the experimental data at the value indicated by the dotted bar and includes a Lorentzian broadening of 100 meV. A quantitative prediction for a 9 nm-thick thin film calculated with `LayerOptics` is provided without manual alignment of the QE (Th. w. LayerOptics).

For the presented experimental datasets we show data for samples ranging from the original measurements by Spicer [31] to more recent results from Arizona State University (ASU) [35], Cornell University [30] and HZB [125]. All the experimental datasets show an overall similar behavior, but have differences in the details. Common to all samples is a rather smooth onset around 2.0 eV, followed by a monotonic increase in QE. The measurement from ASU terminates at 2.5 eV, while the other datasets show a similar increase up to 2.7 eV. The sample from Cornell is characterized by a slightly steeper increase after 2.3 eV, reaching a maximum QE of 13% at around 3.0 eV. The QE of the samples from HZB and Spicer show a slower increase but reach higher global maxima of 17% at 2.95 eV and 14% at 3.5 eV, respectively. The differences between the experimental samples can be related to different growth methods. The traditional co-deposited films usually feature a 'knee' around 2.1 eV followed by a defect-driven tail [126]. Modern methods allow quasi-epitaxial (ultra-thin) films, which in the given datatsets are grown

on $SrTiO_3$ (ASU) [35] or via deposition-recrystallization (HZB) [125]. The are closer to ideal crystals and are characterized by a more gradual increase of the QE.

Comparing to these measurements the two theoretically predicted curves from our model, we find again a significantly sharper onset than in the experiment. This has been seen also for the previous examples and is mainly a result of neglecting the surface roughness, as surface effects lead to very significant spatial variations in the work function of up to 0.4 eV [120]. A main difference between both theoretical plots is the absolute value of the QE. The qualitative prediction without LayerOptics was aligned to the experimental values between 2.5 and 2.7 eV, because the experimental datasets are close together in that energy region. However, this choice is somewhat arbitrary. We can see that with this alignment it overestimates the QE at lower energies (< 2.4 eV), while significantly underestimating it at higher energies (> 2.7 eV). The disagreement at higher energies can again be assumed to be due to a low number of bands being included in the BSE.

The spectral response calculated with `LayerOptics` for the 9 nm film is overall higher, reaching a maximum of about 14%. Interestingly, there is also a qualitative change compared to the prediction based solely on the macroscopic dielectric function. While the initial part of the curve shows a similar slope, we no longer find a large decrease of the QE at higher energies after the treatment with `LayerOptics`. This significantly improves the agreement with all experimental results. While our model still overestimates the QE in the initial 2.2–2.7 eV energy range, the slope of the predicted QE follows that of the measurement at Cornell closely. At higher energies the predicted profile is very close to that measured by Spicer and also the absolute value of the QE from our model is very close to that measured in the various experiments. This improvement provided by a macroscopic treatment in the framework of the Fresnel equations shows that it is indeed important to include macroscopic effect like interference and polarization-dependent reflectance within the thin film.

With this final step in the development of our model, we have fulfilled our goal of bridging the gap between the results from *ab initio* theory on a microscopic level and the macroscopic results from real samples in the experiment. With this, we can go beyond the qualitative analysis of optical spectra done before and make quantitative predictions for the QE fully from *ab initio* theory.

5.5 Further Quantitative Predictions

After creating our photoemission model and validating it against experimental data, we will now take a look at further quantitative effects that we can calculate.

Sticking to Cs_3Sb for now, two quantities that are readily available are the reflectance and transmittance calculated in the framework of Fresnel optics. They are plotted in Fig. 26 for the same 9 nm film that was analyzed before.

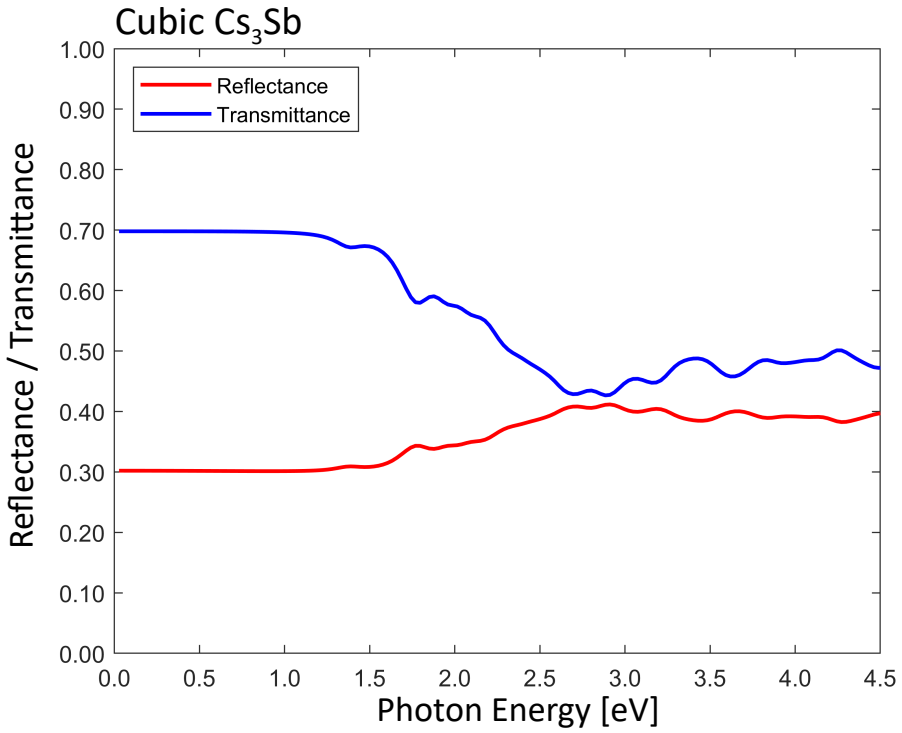

Figure 26: Reflectance and transmittance calculated through `LayerOptics` in the framework of Fresnel optics for a 9 nm film of cubic Cs_3Sb

As seen in Fig. 26, the sum of both coefficients is 1 at low energies where no absorption takes place. In the optically active region, the 'missing' percentage is the absorption coefficient as defined in Eq. 41. The transmittance starts at almost 70 % and decreases to roughly 50 %. This decrease is not monotonous, its slope reflects the peaks in the optical absorption. Similarly, we see an analogous increase of the reflectance from 30 % to around 40 %.

While in the analysis done in the last chapter we focused on the final absorption only, the individual coefficients for reflection and transmission become relevant when describing

heterostructures and interfaces. Light that is transmitted through a photocathode onto a reflective substrate can be reflected back into the cathode and get a second change for absorption. This behavior can be further enhanced through additional layers. For example, it has been shown that the QE of CsK_2Sb, which was already analyzed above, can be significantly increased by depositing it on a single-atomic boron nitride layer, which in turn is on an optically reflective substrate [127]. Untangling the optical absorption into the change in the single Fresnel coefficients is an important piece in the puzzle to understand these complex systems.

Another aspect that is important for the comparison with experimental samples is the effect of changes in the thickness of the film. As calculating the QE for samples of finite thickness is merely a post-processing routine in our model, we can compute the spectral response for films of varying thickness with negligible computational cost. Four examples, ranging from 6 to 15 nm and including the previously shown 9 nm film, are presented in Fig. 27. Experimentally grown Cs_3Sb ultra-thin films are on the same order of thickness, often ranging from 10 to 13 nm [30, 128] after the growth process and lower during it.

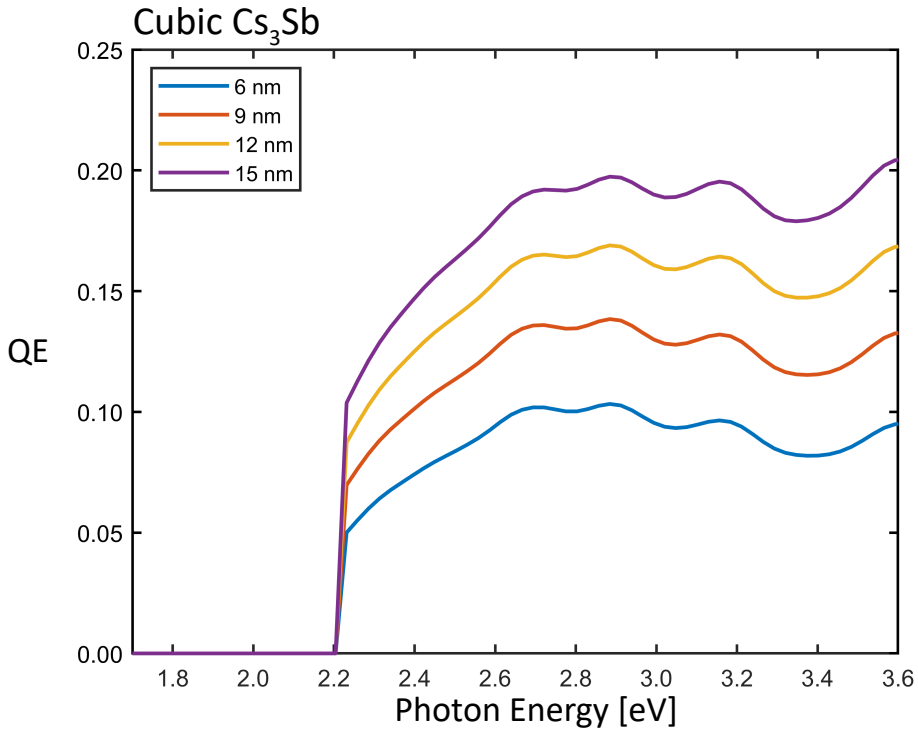

Figure 27: Spectral response calculated for films of varying thickness for cubic Cs_3Sb

As expected, all curves shown in Fig. 27 feature the same slope and differ merely in the absolute values of the quantum efficiency. The peak QE for the 15 nm film is around 20 %, which is twice as large as the maximum QE for the simulated 6 nm film. The examples for 9 and 12 nm are in between, with detailed values for the initial maximum at 2.9 eV reported in Table 2.

Table 2: QE at the initial maximum at 2.9 eV for slabs of different thickness.

Thickness [nm]	QE_{max1} [%]
6	10.33
9	13.84
12	16.89
15	19.74

As seen from Table 2, the increase in QE is not completely linear, as the QE gained per additional nm is slightly reduced for larger thicknesses. Nevertheless, the calculated values are quite large and in particular also larger that the differences observed between ultra-thin samples of different thickness in the experiment, where the QE barely increases during the growth from 4 nm to 10 nm [30]. This discrepancy can be attributed to the fact that we are not explicitly treating losses due to scattering, which would serve as an additional dampening factor that grows larger for films of high thickness. Therefore, the direct comparison between samples of different thickness offers an incomplete picture in the current model and it is important to be aware that the predicted QE serves as an upper limit. For larger films beyond the ultra-thin limit transport can become more relevant, and in that case it may be necessary to return to the qualitative approach used in the initial model validation. In that approach, the effects of scattering are included in the alignment of the maxima between prediction and experiment, as long as the effects of transport can be assumed to be approximately the same for all photon energies.

The large QE predicted without transport motivates a more quantitative estimate on the effects of scattering. While an explicit Monte Carlo treatment goes beyond the current scope of our work, the attenuation length L_a of Cs_3Sb has been determined to be around 26 nm for low energy electrons in the literature [129]. It describes the exponential decay $\propto e^{-z/L_a}$ for an amount of electrons traveling a distance z through the crystal. For a basic estimate independent of the wavelength of the beam we now assume that the excited electrons are spread equally throughout the film with thickness z_0. Under this condition we can determine the percentage of electrons that are successfully transported

to the surface with Eq. 43:

$$P_{\text{Transport}} = \int_0^{z_0} \frac{1}{z_0} e^{-z/L_a} dz = -\frac{L_a}{z_0} e^{-z_0/L_a} + \frac{L_a}{z_0}. \tag{43}$$

The probability calculated with Eq. 43 is a lower boundary as more electrons are excited closer to the surface. However, a more exact description with the optical absorption length would depend on the energy of the incoming photons.

We now calculate the estimated transport probability for the slabs with the different thicknesses from Fig. 27. Analogous to Table 2, the transport adjusted QE of the first maximum is reported in Table 3.

Table 3: Transport probability and adjusted QE at the initial maximum at 2.9 eV for slabs of different thickness.

Thickness [nm]	$P_{\text{Transport}}$ [%]	$\text{QE}_{\text{max1}}^{\text{w. transport}}$ [%]
6	89.3	9.22
9	84.5	11.70
12	80.1	13.53
15	76.0	15.00

As seen from the calculated values, the estimated losses during transport grow quickly with increasing film thickness. For the originally considered 9 nm film, the calculated upper limit of scattering losses is 15.5%, while it already exceeds 20% for films above 12 nm, which in turn leads to a depression of the QE.

We will now make a quantitative comparison with experimentally measured ultra-thin Cs_3Sb photocathodes grown on different substrates. Measured values taken from [128] are listed in Table 4. The measurements were performed at 450 nm ($\sim$ 2.8 eV), slightly below the predicted first theoretical maximum from Table 2 and 3.

Table 4: Measured QE at a wavelength of 450 nm for Cs_3Sb photocathodes with different thickness and substrate. Values taken from [128], Fig.5(b).

Substrate	Thickness [nm]	QE [%]
Si_3N_4	3.8	2.8
Si_3N_4	5.6	5.3
Si_3N_4	11.4	5.7
Gr/4H–SiC	2.4	2.4
Gr/4H–SiC	3.8	2.4
Gr/4H–SiC	4.7	4.5
Gr/4H–SiC	6.6	6.0
Gr/4H–SiC	9.5	11.0
Gr/4H–SiC	10.1	6.8
Gr/4H–SiC	11.9	6.8
3C–SiC	2.0	0.2
3C–SiC	4.6	2.0
3C–SiC	9.8	8.4
3C–SiC	10.2	4.6
3C–SiC	12.7	5.4
3C–SiC	13.6	3.8
3C–SiC	14.0	8.4

The experimental data in Table 4 shows a very high variance, making it difficult to identify clear trends. The sample with the highest yield is the measured 9.5 nm film on Gr/4H–SiC. It shows a QE of 11.0 %, which is in excellent agreement with the predicted 11.7 % for the 9 nm film, see Table 3. However, the other experimental data points are below the theoretical prediction. While a larger thickness tends to lead to a higher QE in the experiment, there are also outliers with significantly lower yield, e.g. the 13.6 nm film on 3C–SiC. This underlines the importance of growing high quality samples and suggests that the high QE predicted from our model can be reached in a best case scenario, but this condition is difficult to archive and reproduce.

Finally, we will consider the quantitative differences between the multiple distinct components that appear for non-cubic crystals, as already anticipated in Chap. 4. In particular, we have already shown the distinct in-plane and out-of-plane optical components for hexagonal K_3Sb and Na_3Sb in Fig. 14. For the initial results shown in Fig. 23, this was addressed by averaging over all on-diagonal components. While this approach is reasonable for the comparison with experimental samples, we can also untangle the individual components on the level of the macroscopic QE.

Experimentally, the targeting of individual optical components corresponds to using polarized light for illuminating the photocathode. Detailed experimental studies on the influence of the polarization on the spectral response remain rare, which is likely due to the fact that clean single-crystalline samples are required and the expectation that other effects have a larger impact on the absolute value of the QE. We hope that the availability of theoretical predictions from our model, as presented below, will also boost the experimental research in this direction and support a more detailed understanding of the spectral response for non-cubic crystals. One practical example for the importance of the polarization is the use of photocathodes as Cherenkov detectors. Cherenkov light is always polarized and extremely faint, which means that the correct calibration of the detectors is very delicate and requires a good understanding of the effects of polarization on the cathode [130, 131].

One study on the effects of different polarizations that is available in the literature was performed by K. Matsuoka [132] for NaKCsSb photocathodes. In it, the spectral response was measured for light with parallel and perpendicular polarization at different angles of incidence. While the absolute QE of the samples in this work remains below 1 %, significant differences between the two directions of polarization were found, see [132] Fig. 6 and 7. This motivates a further study of the physical effects that take place. While in the experimental measurement the largest differences appeared for an angle of incidence close to 45 %, we will remain at an incidence normal to the surface in order to first understand the most basic case and leave a possible expansion to all angles to a follow-up work.

In this chapter we consider only hexagonal crystals. For these compounds the two individual components can be targeted by varying the polarization of the incoming light as illustrated in Fig. 28.

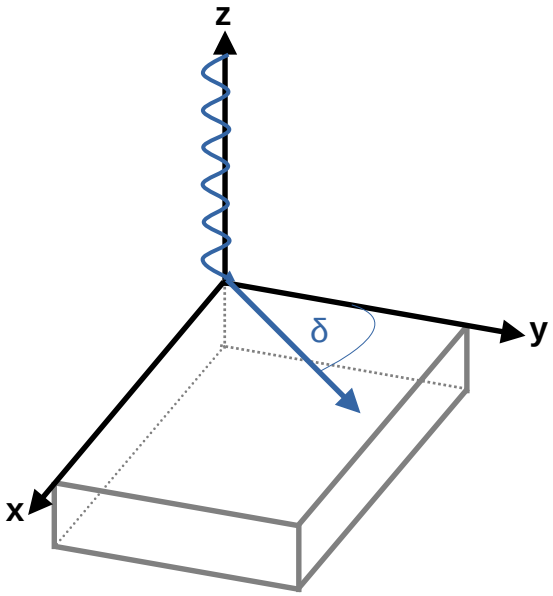

Figure 28: Coordinate system for a sample with a finite thickness in z-direction and a surface in x,y-direction. Light propagates along the z-axis and has a polarization angle δ.

The hexagonal crystal is rotated in such a way that there are distinct components in both x and y-direction. The incoming beam remains normal to the surface and has a polarization δ. At $\delta = 0°$ we target the y-component, at $\delta = 90°$ the x-component, and a mixture of both for everything in between.

The resulting predicted spectral response for light of varying polarization is shown in Fig. 29 for both hexagonal K_3Sb and Na_3Sb. We show results for polarizations of 0°, 90°, and 45° as an intermediate step.

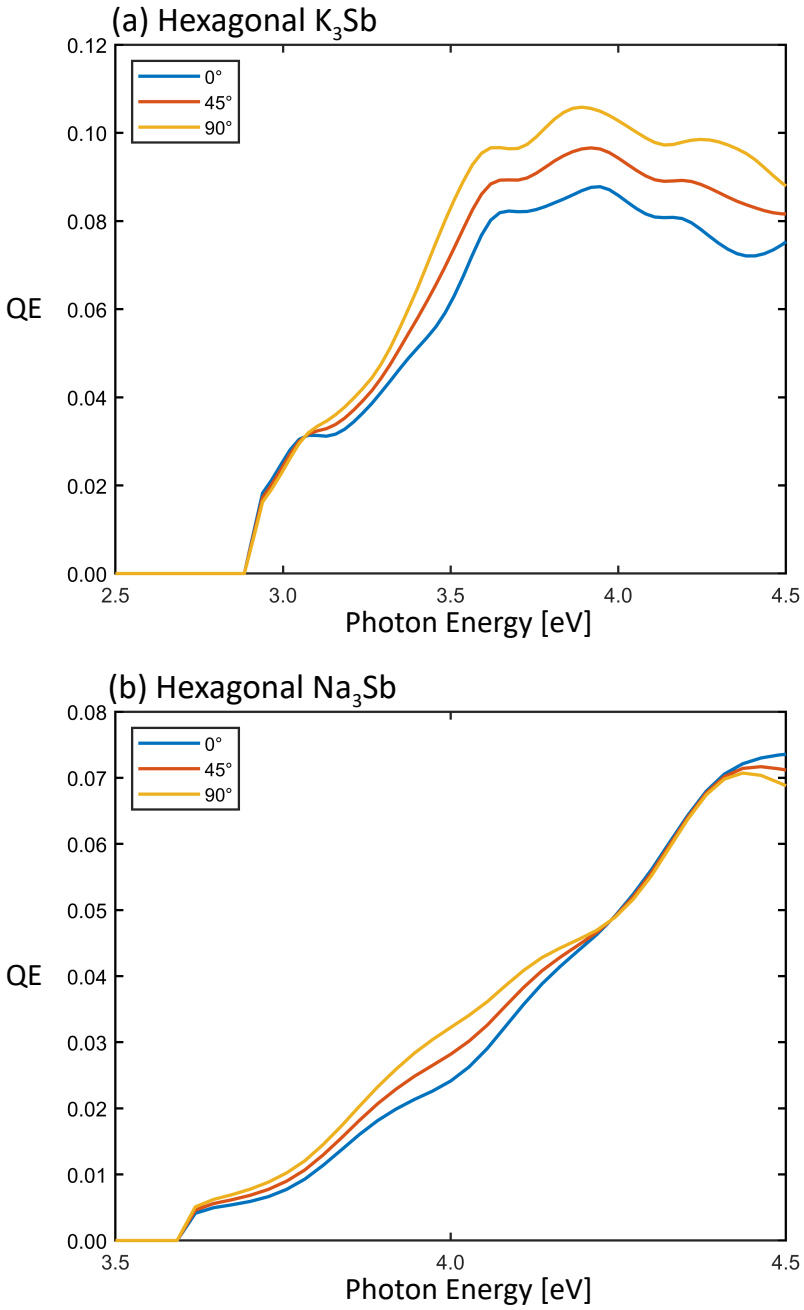

Figure 29: Individual components of the spectral response targeted by varying the polarization of the incoming light, for 9 nm thick films of hexagonal K_3Sb (a) and Na_3Sb (b).

In Fig. 29 (a), we see that there is indeed a significant difference between the two distinct components of hexagonal K_3Sb. The QE at a polarization of 90° is consistently higher than at a polarization of 0°, with a maximum difference of around 2 % in the region between 3.6 and 4.4 eV. This corresponds to the optical spectrum which was shown in Fig. 14(c). Also there we found that the oscillator strength of the parallel component,

which is targeted with a polarization of 90°, is consistently higher than that of the perpendicular component for energies above 3.2 eV. The perpendicular component leads to more absorption at lower energies close to the optical absorption onset, but this is not visible in Fig. 29 because the low energy peaks do not lead to emission. The exact reason for the higher absorption of the parallel component is difficult to pinpoint due to the large number of individual transitions that are contributing. In Fig. 14(c), it is visible that this difference exists also in the IQPA spectrum and is therefore not a product of excitonic effects but rather the fundamental electronic structure. From the PDOS of the material [2](SM) it is known that the top of the valence region as well as the conduction region are dominated by p- and d-states of K as well as p-states of Sb. Contrary to s-states, these orbitals do not posses a spherical symmetry. Therefore, it is unsurprising that transitions between them are strongly influenced by the polarization of the incoming light.

For hexagonal Na_3Sb, on the other hand, we observe only minor differences in the slope between the different polarization at around 4.0 eV. This originates from the fact that the different optical components plotted in Fig. 14(d) are very close together between 4.2 and 5.0 eV. Relating this observation again to the PDOS of the crystal [2], we can assess that s-orbitals are more prevalent in the density of states compared to hexagonal K_3Sb, leading to a lower difference between optical components. The major difference between components at lower energies in Fig. 14(d) is instead a result of excitonic effects.

In order to expand on the analysis of the different optical components for hexagonal crystals, we will take a look at further examples. For this, we turn to the Na-K-Sb compounds with chemical formula $(NaK)_3Sb$. Among these, cubic Na_2KSb was already shown on a qualitative level in Fig. 24(a). In this case, we are mainly interested in the possible hexagonal crystals Na_2KSb and NaK_2Sb, whose basic electronic and optical properties have been analyzed in earlier works [5, 133]. In the same procedure as for K_3Sb and Na_3Sb, we use the polarization of the incoming light to switch between the two distinct optical components. The resulting spectral response is shown in Fig. 30 together with the results for the related cubic crystals. In the plotted results we assume a workfunction of 2.0 eV for all materials, which is the experimental value that was used for cubic Na_2KSb in the earlier analysis.

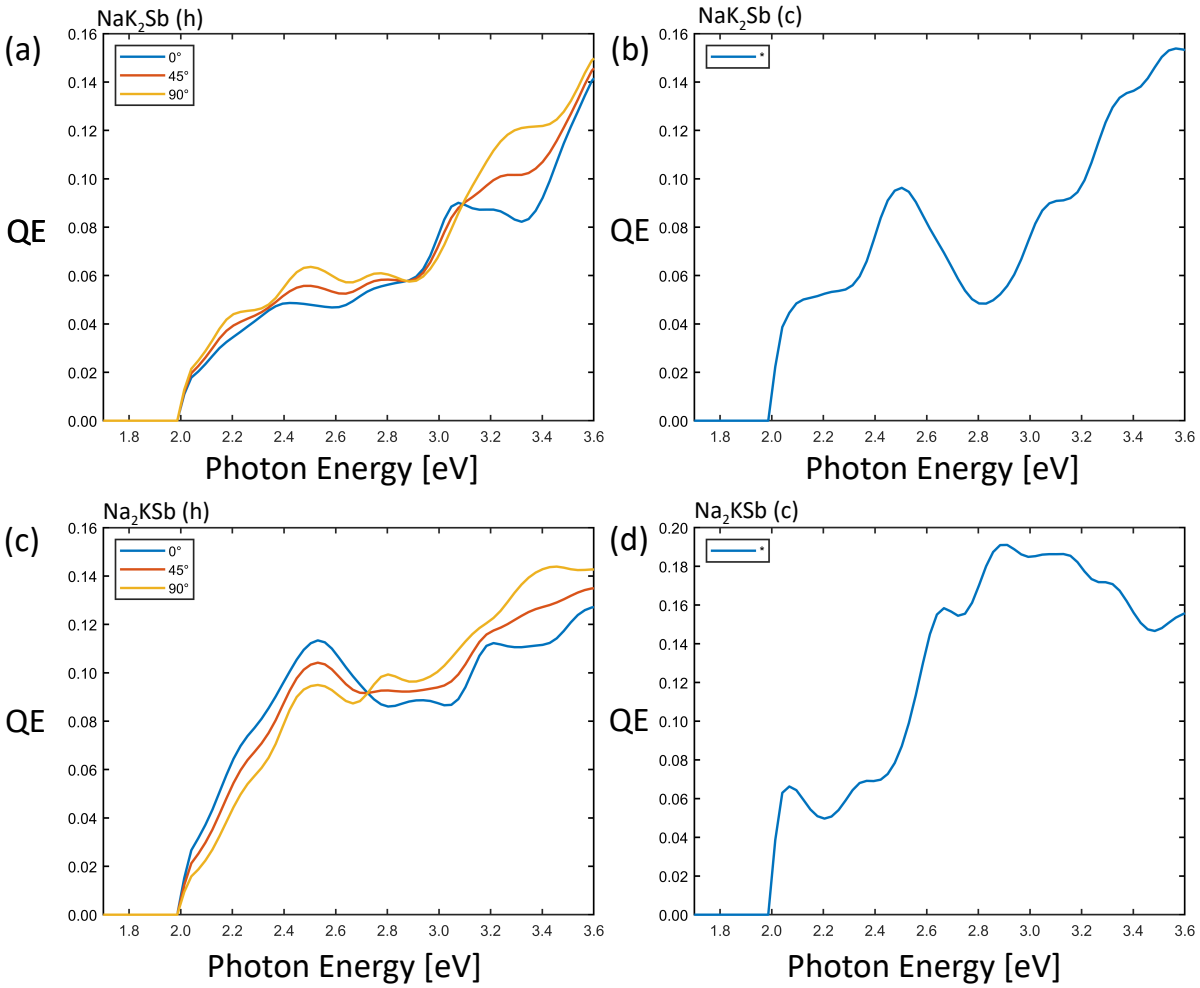

Figure 30: Individual components of the spectral response targeted by varying the polarization of the incoming light, for 9 nm thick films of hexagonal NaK_2Sb (a) and Na_2KSb (c). The calculated spectral response of 9 nm thick films of cubic NaK_2Sb (b) and Na_2KSb (d) is shown as reference.

The spectra for the hexagonal crystals show interesting changes depending on the polarization. For hexagonal NaK_2Sb in Fig. 30(a), we again find the case that one component (at 90° polarization) yields a higher QE over most of the plotted energy region. However, the difference is not very large here, it remains well below 2 % for most photon energies. The spectral response of hexagonal Na_2KSb, on the other hand, shows a different behavior, as seen in panel (c) of the figure. Here, using light with a 0° polarization leads to a QE that is higher at energies close to the onset compared to light with a 90° polarization. However, around 2.7 eV the curves switch their order. Above this energy, the 90° polarization provides a higher QE. The difference between the two optical components reaches again around 2 %.

Considering briefly the spectra of the cubic crystals, starting with cubic NaK_2Sb plotted in Fig. 30(b), we find clear distinct features. After the initial increase at the onset, the QE plateaus between 2.1 and 2.3 eV. Afterwards, there is a significant peak at around 2.5 eV followed by a major decrease. The QE reaches a local minimum at slightly above 2.8 eV and increases again for higher energies. The result in Fig. 30(d) is strongly related to the qualitative spectral response of the same compound shown in Fig. 24(a). Similar to the case of Cs_3Sb, it is visible here that the calculation of the macroscopic QE through `LayerOptics` leads to a higher QE at larger photon energies compared to the spectrum based solely on the macroscopic dielectric function.

Among the four phases shown in Fig. 30, cubic Na_2KSb is the only one for which clean experimental samples without significant contributions from other phases are currently available, as shown with one example during the model validation. It is also the compound with the highest predicted peak QE, reaching almost 20 %. However, the high QE of cubic Na_2KSb appears only for photon energies above 2.5 eV, below these values the yield remains at less than 7 %. For practical applications, it can be beneficial to operate closely to the photoemission threshold in order to keep the excess energy and MTE of the emitted electrons low. In this case, hexagonal Na_2KSb may be superior to the cubic phase, as it offers a higher QE in the region between 2.3 and 2.5 eV. If such a hexagonal and single-crystalline phase of Na_2KSb can be grown, it should be irradiated with polarized light as this can boost the QE by more than 1 % compared to unpolarized light, according to our prediction.

The two NaK_2Sb phases are constrained to a comparably low QE, especially hexagonal NaK_2Sb remains at a maximum QE of 6 % for photon energies below 3 eV. Therefore, it is generally advisable to focus on a 2:1 Na:K ratio when growing $(NaK)_3Sb$ photocathodes.

6 Conclusions and Outlook

In this work, we set out to create an implementation of the three-step model of photoemission based on the results of many-body perturbation theory. This is of major importance in connecting theoretical results on the microscopic level with the macroscopic quantities measured in the experiment.

While previous models based on density functional theory already exist, our approach goes beyond the single-particle picture of previous works. Our methodology, as reviewed in Chap. 2, is based on the GW approximation as well as the Bethe-Salpeter equation and allows us to directly include quasiparticle and excitonic effects. This approach allows us to integrate electron-electron as well as electron-hole correlations in a many-body picture into the calculation of the quantum efficiency.

In preparation for the creation of our model, computational data was collected for a multitude of alkali antimonides. As starting point, we reported the results of a high-throughput study based on DFT for K-Sb and Na-Sb crystals. Starting from an initial structure pool drawn from established databases, we first calculated the energetic properties of these compounds. With this we could generate a convex hull of stable crystals and establish, as a first step, which crystal structures are stable at different K-Sb and Na-Sb stoichiometries. For stable crystals, the electronic structure was calculated in order to understand their fundamental properties. The high-throughput workflow used in this chapter is a powerful tool to screen a large number of complex materials without having to calculate any compound individually. This is especially important when comparing with experimental samples that are not perfect single crystals, as a large amount of different polycrystalline structures can form, including possible intermediate or metastable phases. Our study offers an extensive overview on the properties of the possible phases, going beyond the basic properties previously available in databases.

Complementing the high-throughput screening, we launched a deeper investigation into the properties of eight binary K-Sb and Na-Sb crystals with 3:1 and 1:1 alkali:antimony ratio and diverse lattice symmetries. For this part, we employed many-body perturbation theory in order to calculate QP-gaps and optical spectra. We found low band gaps close to 1 eV and a near-infrared absorption onset for all materials. By analyzing the excitons making up the main peaks in the spectrum, we could obtain further information about their character and distribution in k-space. This study provided us with valuable insights into the fundamental optical properties of the considered materials at a high level of theory, again going far beyond the information previously available in the literature

especially for the crystals with a 1:1 stoichiometry.

After laying the groundwork by calculating sufficient results for the considered alkali antimonides, we then proceeded to the photoemission model itself. The initial photoexcitation is directly covered qualitatively by the results of the BSE. To determine the probability of emission through the surface, a computational scheme was implemented to extract the energy distribution of the photoexcited electrons. Overcoming the surface is then approximated as overcoming a potential step. Scattering events during transport are not treated explicitly in our model in order to focus on the effects that have a larger quantitative impact.

To validate our model, we compared our results against experimental data for multiple binary and ternary alkali antimonides and found an overall excellent agreement. The predicted spectral response generally resolves more individual features than found in the experiment, which is very good and allows us to better understand the origin of the measured data.

Through the Maxwell equations, we managed to connect the dielectric function with the Fresnel coefficients of a finite layer. For the numerical post-processing an updated version of the tool `LayerOptics` was used, leading ultimately to a quantitative prediction of the quantum efficiency. As seen for the example of Cs_3Sb, the predicted values are indeed very close to experimental measurements. This shows that the framework of many-body perturbation theory together with classical Fresnel optics is indeed suited to describe the photoemission process. In particular, it includes many-body features like the electronic self-energy (electron-electron interactions) as well as excitonic effects (electron-hole interactions) that are intrinsic to the photoemission process and could not be captured by previous approaches based solely on density functional theory. Among the more advanced features we can predict with our model, we have seen how we can target the distinct individual components of non-cubic crystals.

Overall, we have fulfilled our goal of creating a many-body extension of the three-step model for semiconductors. The suggested scheme allows us to bridge the gap between the microscopic description of electronic and optical properties from theory and the macroscopic spectral response from experimental samples. With this, the presented work represents a significant milestone in the theoretical description of semiconducting photocathode materials. On the one hand, our model allows us to understand the physical effects that give rise to the measured experimental peaks in a many-body framework, offering a more accurate description than previous models with their single-particle approach. On the

other hand, the possibility of quantitative predictions opens the road for a future *ab initio* screening of possible photocathode materials in order to determine which compounds would be candidates for further studies. In this regard, one major benefit of our model is the fact that it can offer accurate quantitative predictions without the need for empirical inputs such as experimental band gaps.

Looking at the experimental side, the better understanding of the spectral characteristics of photoemission in alkali antimonide materials allows us to work towards improving the design and optimization of the next generation of electron sources. The caveat is, of course, that the connection between theory and experiment is only straightforward for perfect single crystals. Thus, also refinements of the experimental growth of (quasi-)epitaxial samples are needed.

When considering a future follow-up work, there are multiple possible avenues.

On the one hand, the model itself can still be expanded. In particular, the effects of scattering need to be further quantified. We have seen with the calculated spectral response of Cs_3Sb for films of different thickness that we tend to slightly overestimate the quantum efficiency, especially its increase with growing thickness. Here, including losses due to scattering would certainly improve the agreement with experimental measurements. If we wish to simulate larger samples beyond the ultra-thin limit, transport also becomes more relevant. This point could be addressed through incorporating results from Monte-Carlo simulations in a future installment of the model. Another necessary aspect is the calculation of phonon properties, which is also possible from first principles [134, 135, 136].

Another relevant and non-trivial point is the emission through the surface. The description used here with a potential barrier is clearly a major simplification. While it provides reasonable results, the potential of real surfaces is much more complicated. In particular, experimental samples usually also show a certain surface roughness combined with possible defects or pollutants. While the explicit modeling of surfaces is not an issue, the combination of all possible effects is not straightforward at all. However, this point could be addressed with a high-throughput study of possible surface configurations, similar to an existing work on the surfaces facets of cesium telluride [137].

On the other hand, there are also additional possibilities to use the model we designed. In addition to the photocathode crystals themselves, we can proceed to explicitly model heterostructures, combining cathode, substrate and possible residual layers. This allows us to get even closer to the experiment, where some of the most promising samples utilize

a combination of different layers.

Summing up, there are still many effects left to explore, but the creation and verification of the model presented in this work is a major advancement in this field of research. It opens the road for a further close collaboration between theory and experiment in order to design the next-generation of advanced electron sources.

Acknowledgments

I would like to thank Caterina Cocchi for supervising this thesis and for supporting me in my academic career over many years.

Throughout the course of this work, I have had many positive interactions and stimulating discussions with my colleagues in our group as well as with our collaborators. I much appreciate the positive atmosphere that we have always maintained.

Finally, I am grateful to my family for always supporting me in my endeavors.

This work was funded by the DFG, Project No. 490940284.

The majority of the presented calculations were performed at the clusters CARL and ROSA of the High-Performance Computing Center at the University of Oldenburg, with funding provided by the Lower Saxony Ministry for Science and Culture and by the DFG (Project Nr. INST 184/157-1 and INST 184/225-1 FUGG). Additional calculations were performed at the ARA cluster of the University of Jena.

References

[1] R. Schier, C. Wang, J. Dube, J. Kühn, A. Galdi, T. Kamps, and C. Cocchi. Quantitative photoemission predictions of semiconducting photocathodes from many-body ab initio theory. *arXiv preprint arXiv:2602.12997*, 2026.

[2] R. Schier and C. Cocchi. Electronic and optical excitations of K-Sb and Na-Sb crystals. *Phys. Rev. Mat.*, 9(5):053804, 2025.

[3] R. Schier, D. Guo, H.-D. Saßnick, and C. Cocchi. Stability and electronic properties of K-Sb and Na-Sb binary crystals from high-throughput ab initio calculations. *Adv. Theory Simul.*, 7(12):2400680, 2024.

[4] R. Schier, H.-D. Saßnick, and C. Cocchi. Stability and electronic properties of CsK_2Sb surface facets. *Phys. Rev. Materials*, 6(12):125001, 2022.

[5] C. Xu, R. Schier, and C. Cocchi. Electronic and optical properties of computationally predicted Na–K–Sb crystals. *Electron. Struct.*, 7(1):015001, 2025.

[6] C. Xu, R. Schier, and C. Cocchi. Ab initio x-ray near-edge spectroscopy of sodium-based multi-alkali antimonides. *Phys. Chem. Chem. Phys.*, 27(36):19071–19080, 2025.

[7] M. Von Ardenne. Das Elektronen-Rastermikroskop: Theoretische Grundlagen. *Zeitschrift für Physik*, 109(9):553–572, 1938.

[8] P. Emma, R. Akre, J. Arthur, R. Bionta, C. Bostedt, J. Bozek, A. Brachmann, P. Bucksbaum, R. Coffee, F.-J. Decker, et al. First lasing and operation of an ångstrom-wavelength free-electron laser. *Nature Photonics*, 4(9):641–647, 2010.

[9] A. H. Zewail. 4d ultrafast electron diffraction, crystallography, and microscopy. *Annu. Rev. Phys. Chem.*, 57(1):65–103, 2006.

[10] G. H. Campbell, J. T. McKeown, and M. K. Santala. Time resolved electron microscopy for in situ experiments. *Applied Physics Reviews*, 1(4), 2014.

[11] D. Filippetto, P. Musumeci, R. K. Li, B. J. Siwick, M. R. Otto, M. Centurion, and J. P. F. Nunes. Ultrafast electron diffraction: Visualizing dynamic states of matter. *Rev. Mod. Phys.*, 94(4):045004, 2022.

[12] P. Musumeci, J. G. Navarro, J. B. Rosenzweig, L. Cultrera, I. Bazarov, J. Maxson, S. Karkare, and H. Padmore. Advances in bright electron sources. *Nucl. Instrum. Methods Phys. Res. A*, 907:209–220, 2018.

[13] J. Schaber, R. Xiang, and N. Gaponik. Review of photocathodes for electron beam sources in particle accelerators. *J. Mater. Chem. C*, 11(9):3162–3179, 2023.

[14] H. Hertz. Über einen Einfluss des ultravioletten Lichtes auf die electrische Entladung. *Annalen der Physik*, 267(8):983–1000, 1887.

[15] A. Einstein. Über einen die Erzeugung und Verwandlung des Lichtes betreffenden heuristischen Gesichtspunkt. *Annalen der Physik*, 322(6):132–148, 1905.

[16] D. H. Dowell, I. Bazarov, B. Dunham, K. Harkay, C. Hernandez-Garcia, R. Legg, H. Padmore, T. Rao, J. Smedley, and W. Wan. Cathode R&D for future light sources. *Nucl. Instrum. Methods Phys. Res. A*, 622(3):685–697, 2010.

[17] T. Rao and D. H. Dowell. An engineering guide to photoinjectors. *arXiv preprint arXiv:1403.7539*, 2014.

[18] C. Ghosh and B. P. Varma. Preparation and study of properties of a few alkali antimonide photocathodes. *J. Appl. Phys.*, 49(8):4549–4553, 1978.

[19] R. Xiang, A. Arnold, P. Lu, P. Murcek, J. Teichert, H. Vennekate, et al. Study of magnesium photocathodes for superconducting RF photoinjectors. *IPAC 2018*, 10, 2018.

[20] T. Srinivasan-Rao, J. Fischer, and T. Tsang. Photoemission studies on metals using picosecond ultraviolet laser pulses. *J. Appl. Phys.*, 69(5):3291–3296, 1991.

[21] H. J. Qian, J. B. Murphy, Y. Shen, C. X. Tang, and X. J. Wang. Surface photoemission in a high-brightness electron beam radio frequency gun. *Appl. Phys. Lett.*, 97(25), 2010.

[22] B. Feuerbacher and B. Fitton. Experimental investigation of photoemission from satellite surface materials. *J. Appl. Phys.*, 43(4):1563–1572, 1972.

[23] M. A. H. Schmeißer, S. Mistry, H. Kirschner, S. Schubert, A. Jankowiak, T. Kamps, and J. Kühn. Towards the operation of Cs-K-Sb photocathodes in superconducting rf photoinjectors. *Phys. Rev. ST Accel. Beams*, 21(11):113401, 2018.

[24] T. Yue, P. Sui, Y. Zhao, J. Ni, S. Meng, and Z. Dai. Theoretical prediction of mechanics, transport, and thermoelectric properties of full heusler compounds Na_2KSb and X_2CsSb (X= K, Rb). *Phys. Rev. B*, 105(18):184304, 2022.

[25] J. Feng, J. Nasiatka, W. Wan, S. Karkare, J. Smedley, and H. A. Padmore. Thermal limit to the intrinsic emittance from metal photocathodes. *Appl. Phys. Lett.*, 107(13), 2015.

[26] S. H. Kong, J. Kinross-Wright, D. C. Nguyen, and R. L. Sheffield. Cesium telluride photocathodes. *J. Appl. Phys.*, 77(11):6031–6038, 1995.

[27] L. Cultrera, C. Gulliford, A. Bartnik, H. Lee, and I. Bazarov. Ultra low emittance electron beams from multi-alkali antimonide photocathode operated with infrared light. *Appl. Phys. Lett.*, 108(13):134105, 2016.

[28] S. K. Mohanty, M. Krasilnikov, A. Oppelt, F. Stephan, D. Sertore, L. Monaco, C. Pagani, and W. Hillert. Development and characterization of multi-alkali antimonide photocathodes for high-brightness rf photoinjectors. *Micromachines*, 14(6):1182, 2023.

[29] S. Schubert, M. Ruiz-Osés, I. Ben-Zvi, T. Kamps, X. Liang, E. Muller, K. Müller, H. Padmore, T. Rao, X. Tong, et al. Bi-alkali antimonide photocathodes for high brightness accelerators. *APL Mater.*, 1(3), 2013.

[30] C. T. Parzyck, A. Galdi, J. K. Nangoi, W. J. I. DeBenedetti, J. Balajka, B. D. Faeth, H. Paik, C. Hu, T. A. Arias, M. A. Hines, D. G. Schlom, K. M. Shen, and J. M. Maxson. Single-crystal alkali antimonide photocathodes: High efficiency in the ultrathin limit. *Phys. Rev. Lett.*, 128:114801, 2022.

[31] W. E. Spicer. Photoemissive, photoconductive, and optical absorption studies of alkali-antimony compounds. *Phys. Rev.*, 112(1):114, 1958.

[32] J. Dube, J. Kühn, C. Wang, S. Mistry, G. Klemz, A. Galdi, and T. Kamps. Triple evaporation growth and photoemission characterization of bialkali antimonide photocathodes. *J. Appl. Phys.*, 138(4):045704, 2025.

[33] Z. Yusof, A. Denchfield, M. Warren, J. Cardenas, N. Samuelson, L. Spentzouris, J. Power, and J. Zasadzinski. Photocathode quantum efficiency of ultrathin Cs2Te layers on Nb substrates. *Phys. Rev. Accelerators and Beams*, 20(12):123401, 2017.

[34] M. Warren, A. Denchfield, W. Gai, N. Samuelson, J. Shao, L. Spentzouris, E. Wisniewski, Z. Yusof, J. Zasadzinski, et al. Development of hybrid superconducting photocathodes on niobium using high qe coatings. In *Proceedings of the 18th Int. Conf. on RF Superconductivity, SRF2017*, volume 5, 2017.

[35] P. Saha, O. Chubenko, G. S. Gevorkyan, A. Kachwala, C. J. Knill, C. Sarabia-Cardenas, E. Montgomery, S. Poddar, J. T. Paul, R. G. Hennig, et al. Physically and chemically smooth cesium-antimonide photocathodes on single crystal strontium titanate substrates. *Appl. Phys. Lett.*, 120(19):194102, 2022.

[36] J. Feng, S. Karkare, J. Nasiatka, S. Schubert, J. Smedley, and H. Padmore. Near atomically smooth alkali antimonide photocathode thin films. *J. Appl. Phys.*, 121(4):044904, 2017.

[37] C. Wang, J. Dube, A. Galdi, T. Kamps, and J. Kühn. Triple evaporation growth of Sodium-Potassium-Antimonide thin films as photoemission source for electron accelerators. *J. Phys. D*, 2026.

[38] C. Cocchi, S. Mistry, M. Schmeißer, R. Amador, J. Kühn, and T. Kamps. Electronic structure and core electron fingerprints of caesium-based multi-alkali antimonides for ultra-bright electron sources. *Sci. Rep.*, 9(1):18276, 2019.

[39] H. Kirschner, A. Jankowiak, T. Kamps, J. Kühn, M. A. H. Schmeißer, et al. Measuring the spectral response of Cs-K-Sb photocathodes for bERLinPro. In *8th Int. Particle Accelerator Conf.(IPAC'17), Copenhagen, Denmark*, 2017.

[40] H. Panuganti, E. Chevallay, V. Fedosseev, and M. Himmerlich. Synthesis, surface chemical analysis, lifetime studies and degradation mechanisms of Cs-K-Sb photocathodes. *Nucl. Instrum. Methods Phys. Res. A*, 986:164724, 2021.

[41] N. Marzari, A. Ferretti, and C. Wolverton. Electronic-structure methods for materials design. *Nature Mater.*, 20(6):736–749, 2021.

[42] S. G. Louie, Y.-H. Chan, F. H. da Jornada, Z.u Li, and D. Y. Qiu. Discovering and understanding materials through computation. *Nature Mater.*, 20(6):728–735, 2021.

[43] C. N. Berglund and W. E. Spicer. Photoemission studies of copper and silver: Theory. *Phys. Rev.*, 136(4A):A1030, 1964.

[44] B. Camino, T. C. Q. Noakes, M. Surman, E. A. Seddon, and N. M. Harrison. Photoemission simulation for photocathode design: Theory and application to copper and silver surfaces. *Comp. Mater. Sci.*, 122:331–340, 2016.

[45] E. R. Antoniuk, Y. Yue, Y. Zhou, P. Schindler, W. A. Schroeder, B. Dunham, P. Pianetta, T. Vecchione, and E. J. Reed. Generalizable density functional theory based photoemission model for the accelerated development of photocathodes and other photoemissive devices. *Phys. Rev. B*, 101(23):235447, 2020.

[46] P. Saha, O. Chubenko, J. K. Nangoi, T. Arias, E. Montgomery, S. Poddar, H. A. Padmore, and S. Karkare. Theory of photoemission from cathodes with disordered surfaces. *J. Appl. Phys.*, 133(5), 2023.

[47] E. Schrödinger. Quantisierung als Eigenwertproblem. *Annalen der Physik*, 385(13):437–490, 1926.

[48] E. Schrödinger. An undulatory theory of the mechanics of atoms and molecules. *Phys. Rev.*, 28(6):1049, 1926.

[49] T. Busch, B.-G. Englert, K. Rzażewski, and M. Wilkens. Two cold atoms in a harmonic trap. *Foundations of Physics*, 28(4):549–559, 1998.

[50] M. Born and R. Oppenheimer. Zur Quantentheorie der Molekeln. *Annalen der Physik*, 389(20):457–484, 1927.

[51] D. R. Hartree. The wave mechanics of an atom with a non-coulomb central field. part ii. some results and discussion. In *Mathematical Proceedings of the Cambridge Philosophical Society*, volume 24, pages 111–132. Cambridge University Press, 1928.

[52] D. R. Hartree and W. Hartree. Self-consistent field, with exchange, for beryllium. *Proceedings of the Royal Society of London. Series A-Mathematical and Physical Sciences*, 150(869):9–33, 1935.

[53] J. C. Slater. A simplification of the Hartree-Fock method. *Phys. Rev.*, 81(3), 1951.

[54] P. Hohenberg and W. Kohn. Inhomogeneous electron gas. *Phys. Rev.*, 136:B864–B871, 1964.

[55] W. Kohn and L. J. Sham. Self-consistent equations including exchange and correlation effects. *Phys. Rev.*, 140:A1133–A1138, 1965.

[56] J. P. Perdew and K. Schmidt. Jacob's ladder of density functional approximations for the exchange-correlation energy. In *AIP conference proceedings*, volume 577, pages 1–20. American Institute of Physics, 2001.

[57] P. A. M. Dirac. Note on exchange phenomena in the Thomas atom. In *Mathematical proceedings of the Cambridge philosophical society*, volume 26, pages 376–385. Cambridge University Press, 1930.

[58] J. P. Perdew and Y. Wang. Accurate and simple analytic representation of the electron-gas correlation energy. *Phys. Rev. B*, 45(23):13244, 1992.

[59] M. Gell-Mann and K. A. Brueckner. Correlation energy of an electron gas at high density. *Phys. Rev.*, 106(2):364, 1957.

[60] D. M. Ceperley and B. J. Alder. Ground state of the electron gas by a stochastic method. *Phys. Rev. Lett.*, 45(7):566, 1980.

[61] D. C. Langreth and M. J. Mehl. Beyond the local-density approximation in calculations of ground-state electronic properties. *Phys. Rev. B*, 28(4):1809, 1983.

[62] J. P. Perdew. Density-functional approximation for the correlation energy of the inhomogeneous electron gas. *Phys. Rev. B*, 33(12):8822, 1986.

[63] D. C. Langreth and J. P. Perdew. Theory of nonuniform electronic systems. i. analysis of the gradient approximation and a generalization that works. *Phys. Rev. B*, 21(12):5469, 1980.

[64] J. P. Perdew, J. A. Chevary, S. H. Vosko, K. A. Jackson, M. R. Pederson, D. J. Singh, and C. Fiolhais. Atoms, molecules, solids, and surfaces: Applications of the generalized gradient approximation for exchange and correlation. *Phys. Rev. B*, 46(11):6671, 1992.

[65] J. P. Perdew, K. Burke, and M. Ernzerhof. Generalized gradient approximation made simple. *Phys. Rev. Lett.*, 77(18):3865, 1996.

[66] J. P. Perdew, M. Ernzerhof, and K. Burke. Rationale for mixing exact exchange with density functional approximations. *J. Chem. Phys.*, 105(22):9982–9985, 1996.

[67] C. Adamo and V. Barone. Toward reliable density functional methods without adjustable parameters: The PBE0 model. *J. Chem. Phys.*, 110(13):6158–6170, 1999.

[68] A. D. Becke. Density-functional thermochemistry. iii. the role of exact exchange. *J. Chem. Phys.*, 98(7):5648–5652, 1993.

[69] P. J. Stephens, F. J. Devlin, C. F. Chabalowski, and M. J. Frisch. Ab initio calculation of vibrational absorption and circular dichroism spectra using density functional force fields. *J. Phys. Chem.*, 98(45):11623–11627, 1994.

[70] T. Yanai, D. P. Tew, and N. C. Handy. A new hybrid exchange–correlation functional using the Coulomb-attenuating method (CAM-B3LYP). *Chem. Phys. Lett.*, 393(1-3):51–57, 2004.

[71] F. Jensen. Atomic orbital basis sets. *Wiley Interdisciplinary Reviews: Computational Molecular Science*, 3(3):273–295, 2013.

[72] J. C. Slater. Atomic shielding constants. *Phys. Rev.*, 36(1):57, 1930.

[73] S. Goedecker, M. Teter, and J. Hutter. Separable dual-space Gaussian pseudopotentials. *Phys. Rev. B*, 54(3):1703, 1996.

[74] C. Hartwigsen, S. Gœdecker, and J. Hutter. Relativistic separable dual-space Gaussian pseudopotentials from H to Rn. *Phys. Rev. B*, 58(7):3641, 1998.

[75] M. Krack. Pseudopotentials for H to Kr optimized for gradient-corrected exchange-correlation functionals. *Theo. Chem. Accounts*, 114(1):145–152, 2005.

[76] F. Bloch. Über die Quantenmechanik der Elektronen in Kristallgittern. *Zeitschrift für Physik*, 52(7):555–600, 1929.

[77] G. Gilat. Analysis of methods for calculating spectral properties in solids. *Journal of Computational Physics*, 10(3):432–465, 1972.

[78] D. J. Chadi and M. L. Cohen. Electronic structure of $Hg_{1-x}Cd_xTe$ alloys and charge-density calculations using representative k points. *Phys. Rev. B*, 7(2):692, 1973.

[79] H. J. Monkhorst and J. D. Pack. Special points for Brillouin-zone integrations. *Phys. Rev. B*, 13(12):5188, 1976.

[80] L. Hedin. New method for calculating the one-particle green's function with application to the electron-gas problem. *Phys. Rev.*, 139:A796–A823, 1965.

[81] N. Marom, F. Caruso, X. Ren, O. T. Hofmann, T. Körzdörfer, J. R. Chelikowsky, A. Rubio, M. Scheffler, and P. Rinke. Benchmark of GW methods for azabenzenes. *Phys. Rev. B*, 86(24):245127, 2012.

[82] F. Caruso, M. Dauth, M. J. Van Setten, and P. Rinke. Benchmark of GW approaches for the GW 100 test set. *J. Chem. Theory. Comput.*, 12(10):5076–5087, 2016.

[83] M. S. Hybertsen and S. G. Louie. Electron correlation in semiconductors and insulators: Band gaps and quasiparticle energies. *Phys. Rev. B*, 34(8):5390, 1986.

[84] E. E. Salpeter and H. A. Bethe. A relativistic equation for bound-state problems. *Phys. Rev.*, 84:1232–1242, 1951.

[85] G. Strinati. Application of the green's functions method to the study of the optical properties of semiconductors. *La Rivista del Nuovo Cimento*, 11(12):1–86, 1988.

[86] T. Sander, E. Maggio, and G. Kresse. Beyond the tamm-dancoff approximation for extended systems using exact diagonalization. *Phys. Rev. B*, 92(4):045209, 2015.

[87] C. Vorwerk, B. Aurich, C. Cocchi, and C. Draxl. Bethe-Salpeter equation for absorption and scattering spectroscopy: implementation in the exciting code. *Electron. Struct.*, 1(3):037001, 2019.

[88] T. D. Kühne, M. Iannuzzi, M. Del Ben, V. V. Rybkin, P. Seewald, F. Stein, T. Laino, R. Z. Khaliullin, O. Schütt, F. Schiffmann, et al. CP2K: An electronic structure and molecular dynamics software package-quickstep: Efficient and accurate electronic structure calculations. *J. Chem. Phys.*, 152(19), 2020.

[89] M. Krack. Pseudopotentials for H to Kr optimized for gradient-corrected exchange-correlation functionals. *Theo. Chem. Accounts*, 114(1):145–152, 2005.

[90] J. VandeVondele and J. Hutter. Gaussian basis sets for accurate calculations on molecular systems in gas and condensed phases. *J. Chem. Phys.*, 127(11), 2007.

[91] J. W. Furness, A. D. Kaplan, J. Ning, J. P. Perdew, and J. Sun. Accurate and numerically efficient r2SCAN meta-generalized gradient approximation. *J. Phys. Chem. Lett.*, 11(19):8208–8215, 2020.

[92] H.-D. Saßnick and C. Cocchi. Electronic structure of cesium-based photocathode materials from density functional theory: Performance of PBE, SCAN, and HSE06 functionals. *Electron. Struct.*, 3(2):027001, 2021.

[93] A. Gulans, S. Kontur, C. Meisenbichler, D. Nabok, P. Pavone, S. Rigamonti, S. Sagmeister, U. Werner, and C. Draxl. exciting: a full-potential all-electron package implementing density-functional theory and many-body perturbation theory. *J. Phys. Condens. Matter.*, 26(36):363202, 2014.

[94] J. P. Perdew, A. Ruzsinszky, G. I. Csonka, O. A. Vydrov, G. E. Scuseria, L. A. Constantin, X. Zhou, and K. Burke. Restoring the density-gradient expansion for exchange in solids and surfaces. *Phys. Rev. Lett.*, 100:136406, 2008.

[95] E. O. Kane. Theory of photoelectric emission from semiconductors. *Phys. Rev.*, 127(1):131, 1962.

[96] K. L. Jensen, P. G. O'Shea, D. W. Feldman, and N. A. Moody. Theoretical model of the intrinsic emittance of a photocathode. *Appl. Phys. Lett.*, 89(22), 2006.

[97] K. L. Jensen, B. L. Jensen, E. J. Montgomery, D. W. Feldman, P. G. O'Shea, and N. Moody. Theory of photoemission from cesium antimonide using an alpha-semiconductor model. *J. Appl. Phys.*, 104(4), 2008.

[98] D. H. Dowell, F. K. King, R. E. Kirby, J. F. Schmerge, and J. M. Smedley. In situ cleaning of metal cathodes using a hydrogen ion beam. *Phys. Rev. ST Accel. Beams*, 9(6):063502, 2006.

[99] D. Dowell and J. Schmerge. Quantum efficiency and thermal emittance of metal photocathodes. *Phys. Rev. ST Accel. Beams*, 12(7):074201, 2009.

[100] S. Karkare, W. Wan, J. Feng, T. C. Chiang, and H. A. Padmore. One-step model of photoemission from single-crystal surfaces. *Phys. Rev. B*, 95(7):075439, 2017.

[101] C. Cocchi and H.-D. Saßnick. Ab initio quantum-mechanical predictions of semiconducting photocathode materials. *Micromachines*, 12(9):1002, 2021.

[102] H.-D. Saßnick, J. Edzards, T. Reents, and C. Cocchi. aim2dat: A python infrastructure for automated ab initio material modeling and data analysis. *arXiv preprint arXiv:2604.26551*, 2026.

[103] S. P. Huber, S. Zoupanos, M. Uhrin, L. Talirz, L. Kahle, R. Häuselmann, D. Gresch, T. Müller, A. V. Yakutovich, C. W. Andersen, et al. AiiDA 1.0, a scalable computational infrastructure for automated reproducible workflows and data provenance. *Sci. Data*, 7(1):300, 2020.

[104] M. Uhrin, S. P. Huber, J. Yu, N. Marzari, and G. Pizzi. Workflows in AiiDA: Engineering a high-throughput, event-based engine for robust and modular computational workflows. *Comp. Mater. Sci.*, 187:110086, 2021.

[105] A. Jain, S. P. Ong, G. Hautier, W. Chen, W. D. Richards, S. Dacek, S. Cholia, D. Gunter, D. Skinner, G. Ceder, and K. A. Persson. Commentary: The Materials Project: A materials genome approach to accelerating materials innovation. *APL Mater.*, 1(1):011002, 2013.

[106] M. K. Horton, P. Huck, R. X. Yang, J. M. Munro, S. Dwaraknath, A. M. Ganose, R. S. Kingsbury, M. Wen, J. X. Shen, T. S. Mathis, et al. Accelerated data-driven materials science with the Materials Project. *Nature Mater.*, 24(10):1522–1532, 2025.

[107] J. E. Saal, S. Kirklin, M. Aykol, B. Meredig, and C. Wolverton. Materials design and discovery with high-throughput density functional theory: the open quantum materials database (OQMD). *JOM*, 65(11):1501–1509, 2013.

[108] S. Kirklin, J. E. Saal, B. Meredig, A. Thompson, J. W. Doak, M. Aykol, S. Rühl, and C. Wolverton. The Open Quantum Materials Database (OQMD): assessing the accuracy of DFT formation energies. *NPJ Comput. Mater.*, 1(1):1–15, 2015.

[109] A. R. Oganov and M. Valle. How to quantify energy landscapes of solids. *J. Chem. Phys.*, 130(10), 2009.

[110] M. Valle and A. R. Oganov. Crystal fingerprint space–a novel paradigm for studying crystal-structure sets. *Foundations of Crystallography*, 66(5):507–517, 2010.

[111] Y. Hinuma, G. Pizzi, Y. Kumagai, F. Oba, and I. Tanaka. Band structure diagram paths based on crystallography. *Comp. Mater. Sci.*, 128:140–184, 2017.

[112] A. Togo, K. Shinohara, and I. Tanaka. Spglib: a software library for crystal symmetry search. *Science and Technology of Advanced Materials: Methods*, 4(1):2384822, 2024.

[113] H.-D. Saßnick and C. Cocchi. Crystal structure prediction of Cs-Te with supervised machine learning. *Adv. Theory Simul.*, 8(5):2401344, 2025.

[114] C. T. Parzyck, C. A. Pennington, W. J. I. DeBenedetti, J. Balajka, E. M. Echeverria, H. Paik, L. Moreschini, B. D. Faeth, C. Hu, J. K. Nangoi, et al. Atomically smooth films of CsSb: A chemically robust visible light photocathode. *APL Materials*, 11(10), 2023.

[115] P. Gupta, L. Cultrera, and I. Bazarov. Monte Carlo simulations of electron photoemission from cesium antimonide. *J. Appl. Phys.*, 121(21), 2017.

[116] S. Karkare, D. Dimitrov, W. Schaff, L. Cultrera, A. Bartnik, X. Liu, E. Sawyer, T. Esposito, and I. Bazarov. Monte Carlo charge transport and photoemission from negative electron affinity GaAs photocathodes. *J. Appl. Phys.*, 113(10), 2013.

[117] O. Chubenko, S. Karkare, D. Dimitrov, J. Bae, L. Cultrera, I. Bazarov, and A. Afanasev. Monte Carlo modeling of spin-polarized photoemission from p-doped bulk gaas. *J. Appl. Phys.*, 130(6), 2021.

[118] W. E. Spicer. Photoemission and related properties of the alkali-antimonides. *J. Appl. Phys.*, 31(12):2077–2084, 1960.

[119] C. Cocchi, S. Mistry, M. Schmeißer, J. Kühn, and T. Kamps. First-principles many-body study of the electronic and optical properties of CsK_2Sb, a semiconducting material for ultra-bright electron sources. *J. Phys. Condens. Matter.*, 31(1):014002, 2019.

[120] A. Galdi, J. Balajka, W. J. I. DeBenedetti, L. Cultrera, I. V. Bazarov, M. A. Hines, and J. M. Maxson. Reduction of surface roughness emittance of Cs3Sb photocathodes grown via codeposition on single crystal substrates. *Appl. Phys. Lett.*, 118(24), 2021.

[121] J. C. Maxwell. Viii. a dynamical theory of the electromagnetic field. *Philosophical transactions of the Royal Society of London*, (155):459–512, 1865.

[122] C. Vorwerk, C. Cocchi, and C. Draxl. Layeroptics: Microscopic modeling of optical coefficients in layered materials. *Comput. Phys. Commun.*, 201:119–125, 2016.

[123] C. Cocchi, H. Zschiesche, D. Nabok, A. Mogilatenko, M. Albrecht, Z. Galazka, H. Kirmse, C. Draxl, and C. Koch. Atomic signatures of local environment from core-level spectroscopy in β-Ga_2O_3. *Phys. Rev. B*, 94(7):075147, 2016.

[124] C. Cocchi, T. Breuer, G. Witte, and C. Draxl. Polarized absorbance and davydov splitting in bulk and thin-film pentacene polymorphs. *Phys. Chem. Chem. Phys.*, 20(47):29724–29736, 2018.

[125] M. A. H. Schmeißer. *Photocathodes for high brightness, high average current photoelectron injectors*. Humboldt Universität zu Berlin, Germany, 2019.

[126] F. Wooten, J. P. Hernandez, and W. E. Spicer. Photoemission and electron scattering in Cs_3Bi and Cs_3Sb. *J. Appl. Phys.*, 44(3):1112–1117, 1973.

[127] H. Yamaguchi, F. Liu, J. DeFazio, M. Gaowei, L. Guo, A. Alexander, S. I. Yoon, C. Hyun, M. Critchley, J. Sinsheimer, et al. Quantum efficiency enhancement of bialkali photocathodes by an atomically thin layer on substrates. *physica status solidi (a)*, 216(23):1900501, 2019.

[128] W. G. Stam, M. Gaowei, E. M. Echeverria, Kenneth Evans-Lutterodt, Jean Jordan-Sweet, T. Juffmann, S. Karkare, J. Maxson, S. J. van der Molen, C. Pennington, P. Saha, J. Smedley, and R. M. Tromp. Growth of ultra-flat ultra-thin alkali antimonide photocathode films. *APL Mater.*, 12(6):061114, 2024.

[129] A. Galdi, W. J. I. DeBenedetti, J. Balajka, L. Cultrera, I. V. Bazarov, J. M. Maxson, and M. A. Hines. The effects of oxygen-induced phase segregation on the interfacial electronic structure and quantum efficiency of Cs_3Sb photocathodes. *J. Chem. Phys.*, 153(14), 2020.

[130] I. Frank and I. Tamm. Coherent visible radiation from fast electrons passing through matter. *CR Acad. Sci. USSR*, 14:109–114, 1937.

[131] N. Akchurin, F. Bedeschi, A. Cardini, M. Cascella, G. Ciapetti, D. De Pedis, P. Dimpfl, R. Ferrari, S. Franchino, M. Fraternali, et al. Polarization as a tool for dual-readout calorimetry. *Nucl. Instrum. Methods Phys. Res. A*, 638(1):47–54, 2011.

[132] K. Matsuoka. Expression for the angular dependence of the quantum efficiency of a thin multi-alkali photocathode and its optical properties. *Prog. Theor. Exp. Phys.*, 2018(12):123H01, 2018.

[133] R. Amador, H.-D. Saßnick, and C. Cocchi. Electronic structure and optical properties of Na_2KSb and NaK_2Sb from first-principles many-body theory. *J. Phys. Condens. Matter.*, 33(36):365502, 2021.

[134] K. Esfarjani and H. T. Stokes. Method to extract anharmonic force constants from first principles calculations. *Phys. Rev. B*, 77(14):144112, 2008.

[135] I. Errea, M. Calandra, and F. Mauri. Anharmonic free energies and phonon dispersions from the stochastic self-consistent harmonic approximation: Application to platinum and palladium hydrides. *Phys. Rev. B*, 89(6):064302, 2014.

[136] J. Santana-Andreo, H.-D. Saßnick, and C. Cocchi. Thermodynamic stability and vibrational properties of multi-alkali antimonides. *J. Phys. Mater.*, 2024.

[137] H.-D. Saßnick and C. Cocchi. Automated analysis of surface facets: the example of cesium telluride. *NPJ Comput. Mater.*, 10(1):38, 2024.

[138] K. Momma and F. Izumi. *VESTA3* for three-dimensional visualization of crystal, volumetric and morphology data. *J. Appl. Cryst.*, 44(6):1272–1276, 2011.

Appendix

A - Computational Parameters

For plotting crystal structures, the visualization software `VESTA` [138] was used.

Band structure and PDOS plots in Chap. 3 were created through the workflow in `aim`^{2}`dat`, which uses `matplotlib` and `plotly` for visualization. All other plots were created with `MATLAB`.

The k-meshes for the DFT and MBPT calculations are reported in Table 5.

Table 5: Meshes for the DFT and MBPT calculations.

Stoichiometry	Symmetry	DFT	G_0W_0	BSE
K_3Sb / Na_3Sb	cubic	$10 \times 10 \times 10$	$6 \times 6 \times 6$	$8 \times 8 \times 8$
K_3Sb / Na_3Sb	hexagonal	$8 \times 8 \times 4$	$4 \times 4 \times 2$	$8 \times 8 \times 4$
KSb / NaSb	orthorhombic	$8 \times 8 \times 4$	$4 \times 4 \times 2$	$6 \times 6 \times 3$
KSb / NaSb	monoclinic	$8 \times 8 \times 4$	$4 \times 4 \times 2$	$6 \times 6 \times 3$
Cs_3Sb	cubic	$10 \times 10 \times 10$	$4 \times 4 \times 4$	$8 \times 8 \times 8$
CsK_2Sb	cubic	$10 \times 10 \times 10$	$4 \times 4 \times 4$	$8 \times 8 \times 8$
NaK_2Sb / Na_2KSb	cubic	$10 \times 10 \times 10$	$4 \times 4 \times 4$	$8 \times 8 \times 8$
NaK_2Sb / Na_2KSb	hexagonal	$10 \times 10 \times 10$	$4 \times 4 \times 2$	$8 \times 8 \times 4$

B - Computational Calculation of the Energy Distribution

The energy distribution of the excited electron is calculated through a series of post-processing scripts created for the output files of `exciting neon`. First, the energy eigenvalues on the mesh of the BSE calculation are extracted from the `EIGVAL_SCR.OUT` file. This yields a vector of size $n_{\text{all}} \times n_k$, with the total number of bands included in the calculation n_{all} and the total number of k-points n_k. Since only the unoccupied states participating in the BSE are required, all occupied states are discarded and a final vector E_{unocc} of the energy eigenvalues is formed.

The following transformations are applied to E_{unocc}:

1. The energies are shifted to set the VBM to zero: $E_{\text{unocc}} = E_{\text{unocc}} - E_{\text{VBM}}$.
2. Energies are converted from Hartree to eV (1 Ha = 27.211386 eV).
3. A scissor shift is applied to account for the difference between the QP and DFT gaps: $E_{\text{unocc}} = E_{\text{unocc}} + E_{\text{scissor}}$, with $E_{\text{scissor}} = E_{\text{QP-gap}} - E_{\text{DFT-gap}}$.

Next, excitonic weights are read from the files `WEIGHTS_BSE-singlet-TDA-BAR_SCRfull_QMT001_LAMBDAxxxxxx.OUT`. These files provide the contribution of each transition to a specific excitonic state with index λ. Again, the occupied band indices are discared and we construct a weight vector w_{unocc}, which is of the same size as the energy vector E_{unocc} and index-matched to it. For every index i, the pair $\{E_{\text{unocc}}(i), w_{\text{unocc}}(i)\}$ defines the energy and the corresponding excitonic weight of a specific unoccupied state, associated with a known (but not relevant) k-point and band.

The energy distribution of an exciton is obtained by summing up all the excitonic weights at the same energy. In this implementation, we defined a discrete energy grid with a resolution of 1 meV, ranging from 0.000 eV to 7.000 eV. Each energy $E_{\text{unocc}}(i)$ is associated with an energy step $E_{\text{step}}(i)$ by conventional rounding of its value. We then process all weights $w_{\text{unocc}}(i)$, summing the weights at the associated energy steps that were identified. The total sum of the weights then correspond to the energy distribution $D_\lambda(E)$ of the electron associated with the exciton λ:

$$D_\lambda(E) = \sum_i w_{\text{unocc}}(i) \cdot \Delta(E - E_{\text{unocc}}(i)), \tag{44}$$

where Δ represents the discretization onto the energy grid.

C - List of Figures

The contents of Fig. 5-10 have been published in [3], those from Fig. 11-17 in [2] and those from Fig. 18-25 in [1] with minor modifications.